Department für Diagnostische Labormedizinder
Universität Tübingen
Institut für Pathologie und Neuropathologie
Abteilung Allgemeine und Molekulare Pathologie und
Pathologische Anatomie

The role of Anaplastic Lymphoma Kinase (ALK) and CEBPβ-regulated miRNAs in ALK+ Anaplastic Large Cell Lymphoma

Thesis submitted as requirement to fulfill the degree ”Doctor of Philosophy” in *Experimental Medicine* (PhD)

at the
Faculty of Medicine
Eberhard Karls Universität
Tübingen

Presented by:

Montes Mojarro, Ivonne Aidee

Dekan:	Professor Dr. B. Pichler
1. Berichterstatter	Professor Dr. F. Fend
2. Berichterstatter:	Professor A. Weber

Tag der Disputation: 18.09.2023

Parts of the results presented in this dissertation have already been published elsewhere.

Montes-Mojarro I-A, Steinhilber J, Griessinger CM, Rau A, Gersmann A-K, Kohlhofer U, Fallier-Becker P, Liang H-C, Hofmann U, Haag M, Klapper W, Schaeffeler E, Pichler BJ, Schwab M, Fend F, Bonzheim I, Quintanilla-Martinez. CD147 a direct target of miR-146a supports energy metabolism and promotes tumor growth in ALK+ ALCL. *Leukemia*. Aug 2022;36(8):2050-2063. doi:10.1038/s41375-022-01617-x.

Montes-Mojarro I-A, Steinhilber J, Bonzheim I, Quintanilla-Martinez L, Fend F. The Pathological Spectrum of Systemic Anaplastic Large Cell Lymphoma (ALCL). *Cancers (Basel)*. Apr 4, 2018;10(4) doi:10.3390/cancers10040107

Table of contents.

List of figures.

List of tables.

List of supplementary tables.

List of abbreviations.

AA:	Amino acids
ALCL:	Anaplastic Large Cell Lymphoma
AKG:	α-ketoglutarate
ALK:	Anaplastic Lymphoma Kinase
Ab:	Antibody
bp:	Base pair(s)
BSA:	Bovine serum albumin
CDS:	Coding sequence
CD:	Cluster of differentiation
CD93:	Cluster of Differentiation 93
CD147:	Cluster of Differentiation 147 or *BSG*: Basigin
C/EBPβ:	CCAAT/enhancer binding protein beta
CRISPR:	Clustered Regularly Interspaced Short Palindromic Repeats
CT:	Threshold cycle
DLRA:	Dual luciferase reporter assay
dNTPs:	Deoxynucleotide Triphosphates
ΔΨm:	Mitochondrial potential
eGFP:	Enhanced green fluorescent protein
EDTA:	Ethylenediaminetetraacetic acid
ETC:	Electron transport chain
FACS:	Fluorescence Activated Cell Sorting
FBS:	Fetal bovine serum
FCS:	Fetal calf serum
FDR:	False Discovery Rate
FDG:	F-fluorodeoxyglucose
FFPE:	Formalin-Fixed Paraffin-Embedded
GAPDH:	Glyceraldehyde-3-Phosphate Dehydrogenase
GOI:	Gene of interest
GSEA:	Gene set enrichment analysis
KD:	Knockdown
KO:	Knockout

h:	Hour
H&E:	Hematoxylin and eosin
IHC:	Immunohistochemistry
IL:	Interleukin
MCT1:	Monocarboxylat-Transporter
MDR:	Mito Tracker deep red
MG:	Mito Tracker green
miRNAs:	Micro-RNAs
min:	Minutes
nM:	Nanomolar
nt:	Nucleotides
NPM:	Nucleophosmine
PBS:	Phosphate-Buffered Saline
PCR:	Polymerase chain reaction
PET:	Positron emission tomography
pF-S:	Empty pFUGW plasmid
pF-SS1:	FUGW plasmid with a scrambled insert
pF-CD147:	FUGW plasmid carrying a CD147 shRNA
RT-PCR:	Real-time PCR
SD:	Standard Deviation
sh-RNA:	Short hairpin RNA
SLC2A3:	Solute carrier, glucose transporter member 3 or GLUT3
STAT:	Signal transducer and activator of transcription
TCA:	Tricarboxylic acid cycle
TCR:	T cell receptor
TBS-T:	Tris-buffered saline with Tween2
TEM:	Transmission Electron Microscopy
UTR:	Untranslated region
WB:	Western Blot
WHO:	World Health Organization

1. Introduction.

1.1 Anaplastic Large Cell Lymphoma.

1.1.1 Definition and main clinical features.

Anaplastic large cell lymphoma (ALCL) is a distinct group of peripheral T-cell non-Hodgkin lymphomas, common in children and young adults, usually diagnosed in an advanced stage disease and associated with systemic symptoms. Morphologically, it is defined by large anaplastic lymphoid cells with uniform strong expression of CD30 and a propensity to grow cohesively and to invade lymph node sinuses [1-3].

The presence or absence of the recurrent translocation gene t(2;5) (p23;q35) that fuses the anaplastic lymphoma kinase (*ALK*) gene and the nucleophosmin gene (*NPM*), existing in 80% of the cases, denotes the main genetic event and molecular determinant of the clinical behavior of this lymphoma [4]. Therefore, the World Health Organization (WHO) classification of tumors of hematopoietic and lymphoid tumors recognizes two major aggressive subtypes of ALCL based on its distinctive clinical and molecular characteristics: systemic ALK-positive ALCL (ALK+ ALCL) and systemic ALK-negative ALCL (ALK− ALCL) [1].

Systemic ALK+ ALCL accounts for 10-20% of pediatric and adolescent NHL and displays an aggressive clinical course associated with systemic symptoms and rapidly progressive adenopathy [1,2]. Its diagnosis is usually in an advanced stage of disease (III-IV stage), once the patient already presents nodal (90%) and extranodal involvement (40-68%), including skin (26%), soft tissues (15%), bone marrow (14%), lung (12%), liver (8%) and central nervous system (extremely rare <1%) [5-8]. In comparison, ALK− ALCL more commonly affects adults in the sixth decade of life, with a slight male predominance, showing a relatively lower nodal (49%) and extranodal involvement (20%), and poorer clinical behavior [5-9]. The WHO classification recognizes two additional entities within the group of ALCL, including primary cutaneous ALCL and breast implant-associated ALCL. However, these entities are less aggressive lymphomas with typical clinical behavior and localization distinct from ALK+ ALCL and ALK- ALCL[1]. Therefore, these entities have been excluded in this thesis.

1.1.2 Morphological characteristics and Immunophenotype.

ALCL exhibit a broad histologic spectrum with diverse patterns. However, all of them are distinguished by the presence of large anaplastic cells, also called “hallmark cells” These cells are large-sized with a prominent Golgi apparatus, abundant eosinophilic cytoplasm, and horseshoe or kidney-shaped eccentric nuclei (Figure 1C) [10,11]. The dissemination of the neoplastic cells is very characteristic and unusual, simulating a melanoma or a metastatic carcinoma, in which the neoplastic cells present sinusoidal dissemination in the paracortical region and the subcapsular sinuses of the lymph nodes (Figure 1A) [12].

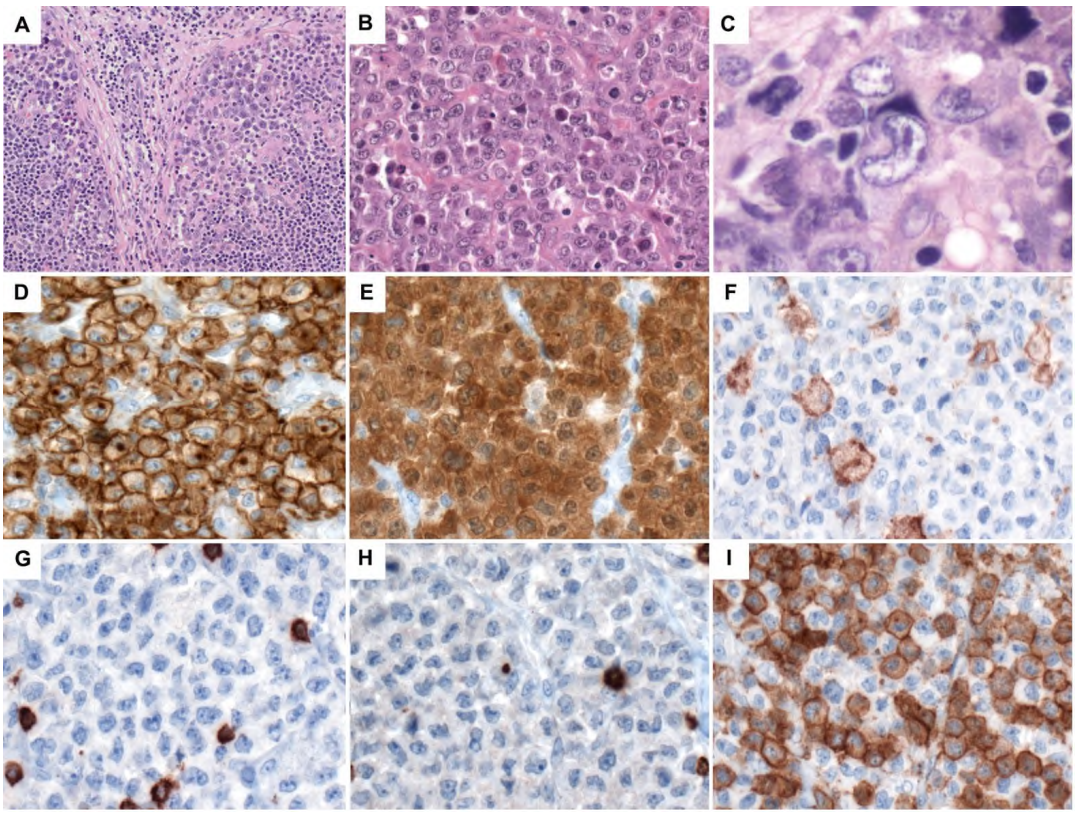

Figure 1. Main morphological and immunohistochemical features of ALK+ ALCL.

The neoplastic cells infiltrate in a cohesive pattern the lymph node sinuses, imitating a metastatic melanoma (A, H&E stain, 100x). The tumor cells are monomorphic, large-sized, and display abundant cytoplasm and kidney shape nuclei (B, H&E stain, 400x); characteristic "hallmark cells" are easily identified. These cells show horseshoe-shaped nuclei and two nucleoli; prominent Golgi is identified by a clear area (C, H&E stain, 630x). By immunohistochemistry, the tumor cells show uniform and strong staining for CD30 (D) and ALK (E). However, CD4 (F), CD3 (G), and CD7 (H) are negative in the tumor cells, but positive in the lymphocytes and macrophages, respectively. The majority of the neoplastic cells are positive for CD5 (I). Immunohistochemistry: 400x (D, E, F, G, H, I) [12]. Abbreviation, H&E Hematoxylin and eosin.

Affected lymph nodes are partially effaced and demonstrate different morphological variants. The neoplastic cells show a broad spectrum ranging from small-medium to large-sized cells; however, hallmark cells constitute the main morphological feature in all cases (Figure 1 B) [10,11]. According to its different morphological features, five main different patterns are recognized by the WHO Classification of Tumours of Haematopoietic and Lymphoid Tissues : the common pattern (60-70%), the small cell pattern (5-10%), the lymphohistiocytic pattern (10%), the Hodgkin-like pattern (3%) and the composite pattern (15%) [1]. In immunohistochemical analyses, the neoplastic cells typically exhibit a strong and uniform expression of CD30 on the cell membrane and in a dot-like or Golgi pattern (Figure 1D). CD30 is a member of the superfamily of tumor necrosis factor receptors (TNFR) [3,13]. In most of the cases, the cells also express epithelial membrane antigen (EMA) and one or more T cell markers; however, the loss of T cell markers indicating a null cell phenotype is not unusual (Figure 1 F, G, H, I) [14] and 75% of cases present negative CD3 staining. However, other T cell antigens, such as CD2, CD4, and CD5, are positive in 40% to 70% of the cases, while CD8 is frequently negative. Cytotoxic molecules such as TIA-1, granzyme B, and perforin are usually positive, which supports the cytotoxic origin of the ALCL cells [9]. TCR betaF1 antibody is only expressed in 4% of the cases, and other TCR-associated molecules such as ZAP70, LAT, and SLP76 are also lacking. The loss of these T cell molecules and antigens is rare in T-cell lymphomas. In ALCL, however, the loss has been related to an epigenetic mechanism mediated by the IL-2 receptor (CD25), a marker strongly expressed in ALCL cells [15]. The T cell origin of ALCL is supported by clonal rearrangements in the TCR genes in 90% of the cases.

ALK monoclonal antibody to detect ALK translocation was developed in 1997 by Pulford *et al*. Until now, it represents the gold standard to detect ALK protein expression and to distinguish the two main ALCL subtypes [16]. Other genetic analyses detect ALK rearrangements, similarly, including sequencing, karyotyping, and fluorescence in situ hybridization (FISH). Interestingly, conferring the nature of ALK fusion protein, the subcellular localization of ALK expression may be different and it might be valuable predicting the fusion partner gene by immunohistochemistry. The classical *NPM1-ALK* translocation exhibits diffuse cytoplasmatic, nuclear and nucleolar staining due to the intracytoplasmic terminal portion of NPM1 and ALK proteins and the co-localization of heterodimers of wild-type *NPM1* and *NPM1-ALK* (Figure 1E). Nevertheless, ALK is

usually located in the cytoplasm when fusions are related to other translocation partners, including *TPM3, ATIC, TFG, CLTC, TPM4,* and *MYH 9* [17-29]*.*

Cases with staining limited to the cellular membrane are rare and usually associated with *MSN-ALK* translocation [17-19], whereas *TPM3-ALK* translocation shows a characteristic diffuse cytoplasmatic staining with peripheral intensification [30]*.* Proteins directly or indirectly targeted by ALK translocation are SHP-1 phosphatase, BCL6, C/EBPβ, CD147, CD44v6, and PD-L1. These molecules play an important role in oncogenesis by promoting cell proliferation, metabolism, metastasis, and immune system deregulation [30-36]. Furthermore, 50% of ALK+ ALCL tumors evaluated by tissue microarrays are positive for SHP-1, an inhibitor of the NPM-ALK signaling pathway, which is essential for tumorigenesis and emerging as a therapeutic target in this lymphoma [31].

1.1.3 Genetic and molecular features.

1.1.3.1 ALK translocation as main oncogenic event.

ALK+ ALCL is well-defined by overexpression and constitutive activation of a chimeric fusion protein involving *ALK*, a well-known oncogene that is believed to regulate the TCR signaling pathway. [37,38]. Up to 80% of the cases show the chromosomal translocation t(2;5), which fuses the *ALK* gene at 2p23 to the nucleophosmin (*NPM*) gene at 5q35. However, further variant translocations of ALK with other partner genes located on chromosomes 1, 2, 3, 17, 19, 22, and X, are relatively common, occurring in 20% of the cases, and all of them result in the upregulation of ALK [4]. The ALK portion of the fusion chimeric proteins containing the catalytic domain of ALK undergoes autophosphorylation, leading to intense and persistent activation [39,40]. Constitutively active ALK fusion proteins drive oncogenesis through a variety of signal transduction pathways, including, phospholipase C γ (PLCγ), phosphatidylinositol 3-kinase (PI3K), serine-threonine kinase-1 (AKT-1), signal transducer and activator of transcription 3 (STAT3), and signal transducer and activator of transcription 5 (STAT5), mechanistic target of Rapamycin (mTOR), p130Crk-associated substrate (p130Cas) and mitogen-induced extracellular kinase (MEK)/extracellular signal-regulated kinase (ERK) [41-45].

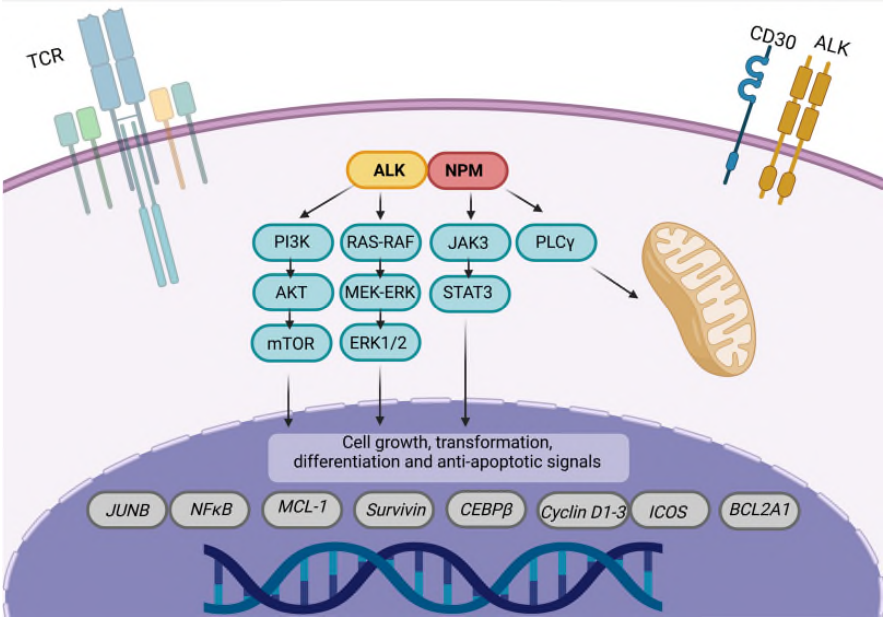

Figure 2. NPM-ALK fusion protein activates different signal transduction pathways.

Aberrant NPM-ALK kinase activates cell signaling pathways similar to those physiologically activated by TCR and IL-2. Through these pathways, many transcriptional targets involved in the proliferation and survival of ALK+ ALCL neoplastic cells are directly activated. Interestingly, NPM-ALK also targets key metabolic pathways promoting anaerobic glycolysis in mitochondria. This figure is adapted from Wernet *et al.* [45] and was created using BioRendercom.

Abbreviations: ALK, anaplastic kinase lymphoma; NPM, nucleophosmin; PI3K, Phosphoinositid-3-Kinasen, AKT serine/threonine kinase; mTOR, mechanistic Target of Rapamycin; MEK-ERK, extracellular signal-regulated kinase (ERK) RAS-RAF- MEK–ERK–MAPK signaling pathway; JAK3, Janus Kinase 3; STAT3, Signal transducer and activator of transcription 3, PLC, Phospholipase C.

Activation of STAT3 is a key oncogenic step in ALK+ ALCL and highly required for the maintenance of the neoplastic ALK+ ALCL phenotype and for the induction of lymphoproliferative signals, promoting the proliferation and survival of tumor cells. [46,47].

Gene expression profiling in ALK+ and ALK- ALCL cell lines and tumor samples have allowed to detect transcriptional targets directly activated by signaling pathways that favor tumor growth and survival of the neoplastic cells , including is the transcription factor CCAAT/enhancer binding protein beta (*C/EBPβ*), one central downstream target of ALK (Figure 2) [41-45].

1.1.3.2 C/EBPβ overexpression.

C/EBPβ is a member of the C/EBP family of transcription factors, which consists of 6 members: *C/EBPα, C/EBPβ, C/EBPγ, C/EBPδ, C/EBPε,* and *C/EBPξ*. All family mem-

bers contain an essential DNA binding and dimerization domain and a leucine zipper motif. This group of basic-leucine zipper (bZIP) transcription factors participates in essential functions such as metabolism, innate and adaptive immunity, inflammation, hematopoiesis, adipogenesis, osteoclastogenesis, cell cycle, cellular proliferation, and cell differentiation [48]. *C/EBPβ* is mainly expressed in macrophages, myelomonocytic cells, liver, adipose tissue, intestine, lung, spleen, nervous system, and kidney [49]. *C/EBPβ* is encoded by an intronless gene, transcribed into a single mRNA, and translated into three protein isoforms: liver-enriched activator protein (LAP*), LAP, and Liver-enriched inhibitory protein (LIP). *C/EBPβ* LAP and LAP* isoforms contain the N-terminal trans-activating and the central regulatory regions, lacking the short LIP isoform.

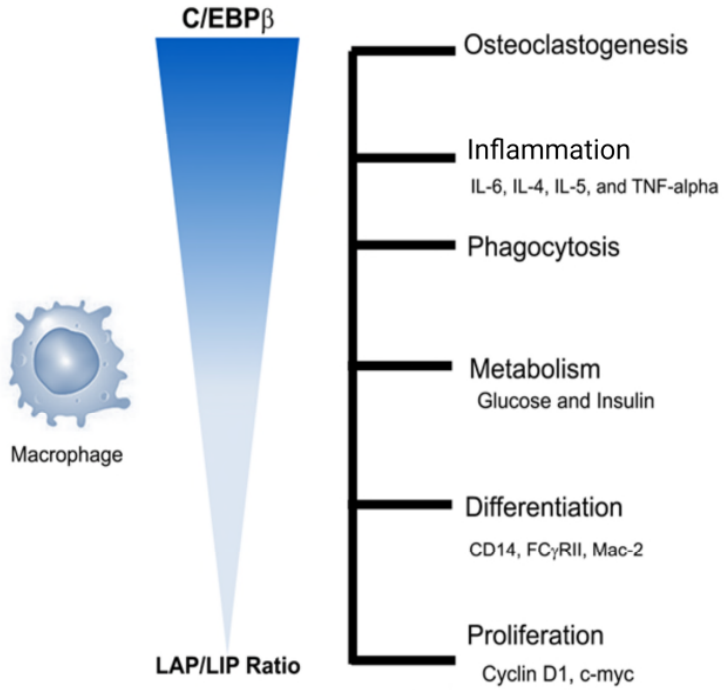

Figure 3. *C/EBPβ* functions and reported target genes.

C/EBPβ functions, including osteoclastogenesis, inflammation, metabolism, differentiation, and proliferation, correlate directly with the LAP/LIP ratio. C/EBPβ target genes are depicted. Adapted from Huber *et al* [49].

The *C/EBPβ* LAP/LIP ratio controls its function and features (Figure 3). The central functions of *C/EBPβ* are associated with liver regeneration, bone homeostasis, me-

tabolism, and monocyte differentiation and regulating the immune and inflammatory response genes such as IL-6, IL-4, IL-5, and TNF-alpha genes [50-52].

C/EBPβ is implicated in cancer and tumorigenesis of solid tumors. In physiological states, this transcription factor is regulated by several autoinhibitory components suppressing the DNA and transactivating domains. However, an oncogenic stimulus such as the MAP kinase pathway can trigger *C/EBPβ* and promote cellular proliferation. In mature lymphocytes, *C/EBPβ* is not constitutively expressed, but it is involved in B cell lymphomagenesis and has a primary role as a regulator of T cell response. Recent evidence has documented the overexpression of C/EBPβ in ALCL, which exhibits ALK kinase-dependent activity, indicating a critical role in proliferation and survival through transcriptional activation of its target genes (Figure 4) [33,42].

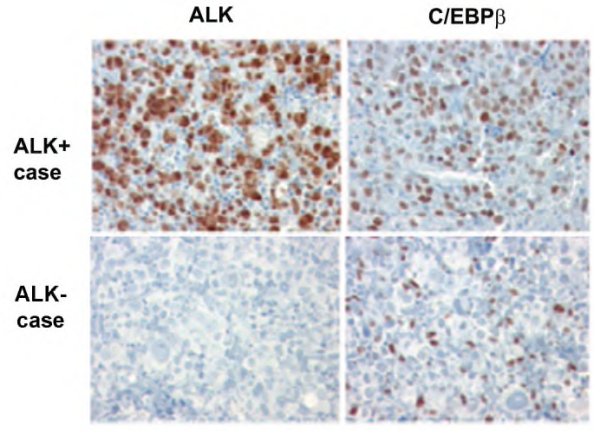

Figure 4. ALK and C/EBPβ immunostaining in ALCL cases.

ALK+ ALCL cases show strong and nuclear staining for C/EBPβ compared to the ALK-ALCL cases, which demonstrate no expression. However, some reactive histiocytes are strongly positive. Immunohistochemistry, original magnification, 400x [33].

C/EBP transcription factors have been related to tumorigenesis in the last decade by regulating the gene expression via posttranscriptional miRNA induction [53]. In acute myeloid leukemia, *C/EBPα* inhibition results in the absence of miR-223, which possess tumor suppressor function. This miRNA triggers normal granulopoiesis in normal myeloid cells [54]; it represses cell proliferation and enhances cell apoptosis [55]. Interestingly, miR-223 is upregulated by *C/EBPβ* in colorectal cancer, contributing to tumor growth [56]. In the respiratory epithelium, cigarette smoke induces *C/EBPβ* overexpres-

sion, which results in miR-31 upregulation promoting pulmonary oncogenesis. Moreover, C/EBP transcription factors similarly contribute to cellular macrophage phenotype by miRNA up- and downregulation [57].

1.1.3.3 miRNAs.

1.1.3.3.1 miRNAs in Cancer.

MiRNAs are short (21-25 nucleotides) non-coding RNAs involved in post-transcriptional regulation of gene expression by affecting the stability and translation of messenger RNA (mRNA). These small molecules were discovered in *Caenorhabditis elegans* in 1993 as the product of the *lin4* gene, which participates in translational repression [58,59]. MiRNAs are transcribed by RNA polymerase II from DNA sequences into primary miRNAs (pri-miRNAs) with hairpin structures and processed into mature miRNAs by two RNase III proteins, Drosha and Dicer. Drosha-DCGR8 enzyme complex cleaves pri-miRNAs into precursor-miRNAs and is then transported to the cytoplasm by exportin-5 and then processed by Dicer to mature miRNAs. Subsequently, mature miRNAs enter the RNA-induced silencing complex (RISC), where they inhibit translation following base pairing to the 3′ untranslated region (UTR) of their mRNA target [30,60]. The region at the 5′ ends of miRNAs that spans from nucleotide positions 2 to 7, called "miRNA seed", is crucial for target recognition. Up to 60% of human protein-coding genes comprise at least one conserved miRNA-binding site, but non-conserved sites are also common, leading to the hypothesis that most of the genes may be under the control of miRNAs [30]. The level of complementarity between the miRNA guide and mRNA target in the RISC determines which silencing mechanism will be employed: cleavage of target mRNA with subsequent degradation or translation inhibition (Figure 5) [61]. However, miRNAs are also able to activate gene expression [30,62]. In the last two decades, more than 2500 miRNAs have been identified in humans (www.mirbase.org) involved in diverse physiological processes, such as embryonic development, cell proliferation, cellular differentiation, and apoptosis, among others [63,64]. Given the abnormal miRNA expression in cancer, there is strong evidence that deregulated miRNAs might contribute to human disease and happen to drive oncogenesis, acting either as tumor suppressor or oncogenes. Therefore, they are also called oncomirs [62,65,66]. MiRNAs can target up to hundreds of genes; however, their

role in tumorigenesis is probably attributed to their regulation of very few specific targets [67]. Therefore, identifying miRNAs and their specific targets is an interesting approach to blocking cancer development and metastases, revealing new therapeutic opportunities [30]. Moreover, the different miRNA signatures in cancer, supported by miRNA expression profiles and depth sequencing, exposed that miRNA profiles are not only suitable as therapeutic targets but also as an accurate method for classification, diagnosis, and prognosis of different neoplasms [62].

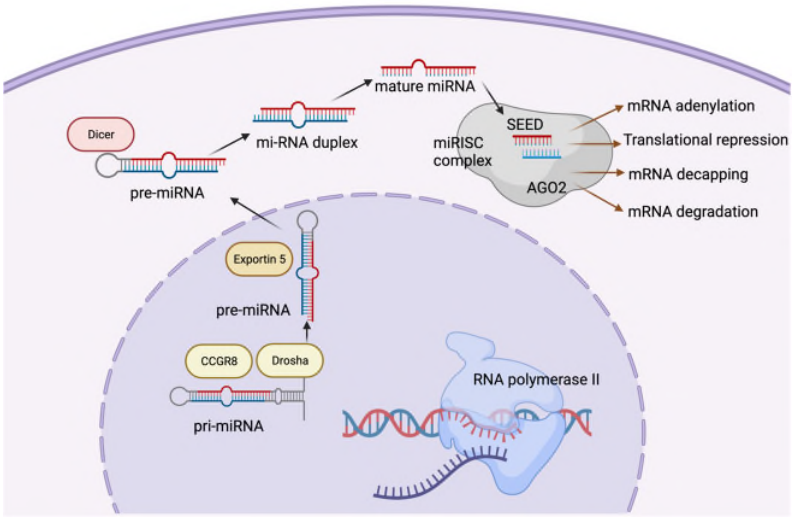

Figure 5. The canonical pathway of the miRNA Biogenesis.

RNA polymerase II transcribes the miRNA, originally known as pri-miRNA, which is >1 kb long. The microprocessor complex, composed of the enzyme Drosha and the RNA binding protein DGCR8, processes these sequences into ~70 nt pre-miRNAs. Then, the Exportin-5 exports the pre-miRNA hairpins to the cytoplasm, where they are cleaved by Dicer to lose the hairpin. Next, one of the miRNA guide duplexes is processed to a mature mi-RNA, which binds to the miRISC complex by the Argonaute protein 2 (AGO-2). The mature mi-RNA guide seeks its complementary mRNA, localized mainly within the 3′-UTRs, also known as the "SEED" sequence, around 2-7 nucleotides long). Moreover, once the miRNA is bound to its mRNA target induces translational repression or mRNA decay via mRNA deadenylation, mRNA decapping, and mRNA degradation. Abbreviations: DGCR8, DiGeorge syndrome critical region gene 8/microprocessor subunit; miRISC, miRNA-induced silencing complex; UTR, untranslated region. The figure was adapted from [68,69] and created using BioRendercom.

The deregulated expression of specific miRNA is well known in solid cancers, leukemias, and lymphomas [64,70-72]. However, the first clinical data about dysregulation of microRNAs was related to the tumorigenesis of chronic lymphocytic leukemia (CLL), where it was described the function of miR-15a and miR-16-1 as tumor suppressors by directly targeting *BCL2*, resulting in apoptosis repression [73,74]. In addition, miRNAs

participate in cell differentiation of leukemic pre-B lymphocytes through miR155-dependent downregulation of *SHIP1* and *CEBPβ*, blocking B-cell differentiation but promoting uncontrolled cell proliferation [75].

MiRNA profiling is also investigated in T-cell lymphomas, facilitating the discernment among the most common peripheral T-cell lymphomas subtypes, including peripheral T-cell lymphoma not otherwise specified (PTCL-NOS), angioimmunoblastic T-cell lymphoma (AITL), ALCL and activated CD4+ and CD8+ T lymphocytes [76]. Moreover, further studies have acknowledged a characteristic miRNA signature of ALK+ ALCL, distinguishing it from ALK− ALK and activated mature T cells [77-79] (Tables 1 and 2).

The top miRNA candidates significantly deregulated in ALK+ ALCL included 11 upregulated miRNAs and one cluster: miR-72-92 cluster, miR-106, miR-135b, miR-182, miR-183, miR-203, miR-340, miR-512-3p, miR-886-5p, miR-886-3p, miR-708, miR-135b ; and 7 downregulated: miR-196b, miR-155, miR-146a, miR-424, miR-503, miR-424*, miR-542-3p [77-79]. Steinhilber *et al.* identified a signature of 56 miRNAs distinguishing ALK+ ALCL, ALK− ALCL, and T cells in *in vitro* experiments. The top candidates significant differentially expressed between T-cells, ALK+ and ALK− ALCL included five upregulated miRNAs: miR-340, miR-203, miR-135b, miR-182, and miR-183; and seven downregulated: miR-196b, miR-155, miR-146a, miR-424, miR-503, miR-424*, and miR-542-3p [79].

Although published studies have rendered different results, the stronger downregulation in ALK+ ALCL of miR-181a, miR-26a, and miR-146a, in comparison to the ALK− ALCL cell lines and normal T cells, triggered the hypothesis that these miRNAs seem to play a role as tumor suppressor genes in ALK+ ALCL and might contribute to ALK mediated oncogenesis and tumor biology (Figure 6) [79].

To date, only some target genes of deregulated miRNAs have been investigated in ALK+ ALCL. In a recent study, some miR-155 target genes, such as *ZNF652, BACH1, RBAK, E2F2,* and *TP53INP1,* were identified [80]. Matsuyama et al. also revealed some target genes of the upregulated miR-135b, including *FOXO1, STAT6*, and *GATA3* [81]. Moreover, MCL-1 was recognized as a target gene of the downregulated miR-29a [82].

Table 1. Distinct mi-RNA signatures to distinguished ALK+ ALCL from normal activated T-cells

Sample	Technique	Upregulated	Downregulated	Reference
ALCL primary tumors: **8 ALK+ ALCL** **T-cells from healthy donors**	LNA-modified miRCURYLNA miRNA Array-ready-to-spot probe set no.208010-A (Exiqon)	miR-886-3p, miR-20b, miR-106a, miR-17, miR-20a,	miR-451, miR-145, **miR-146a,** miR-142-3p, miR-29c, miR-29a, miR-29b, miR-30a, miR-342-3p, **miR-26a,** miR-142-5p, miR-101, miR-150, miR-155	[78]
ALK+ ALCL cell lines (Karpas 299, SU-DHL-1 and SR786) and pool of T-cells		miR-886-3p, miR-886-5p, miR-432*, miR-363*, miR-18a, miR-183, miR-302c*, miR-20b, miR-525-5p, miR-20a, miR-106a, miR-17-1	**miR-146a,** miR-142-3p, miR-640, miR-518e*/519a*/519b-5p, miR-423-3p, miR-423-5p, miR-125a-5p, miR-30c, miR-206, miR-215, miR-452, miR-29b, miR-146b-5p, miR-374b, miR-29a, miR-142-5p, miR-29c, let-7i, miR-30a, miR-374a, miR-101, miR-140-5p, let-7g, miR-22, **miR-26a**, miR-125b, miR-342-3p, miR-369-3p, miR-150	
ALCL primary tumors: **33 ALK+ ALCL** **T-cells from healthy donors**	TaqMan Array Human MicroRNA Card A v.2.0 (ABI)	miR-10b, miR-512-3p, miR-517a, miR-517c, miR134, miR-495, miR-379, miR-539, miR-518e, miR-411, miR-519a, miR376a, miR-511, miR-199a-5p, miR-519d, miR-376a, miR-485-3p, miR-323-3p, miR-137, miR-337-5p, miR-124, miR-204, miR-503, miR-107, miR-518f	miR-375, miR-184, miR98, miR-205, miR501-5p, miR-200a, miR342-5p, miR-486-5p, miR-486-3p.	[77]
ALK+ cell lines (SU-DHL-1, KiJK, Karpas 299 and SR-786) and ALK− ALCL cell line (Mac-1)	Next generation sequencing (Ilumina)	**Significantly deregulated ALK− vs T cells** miR-183, miR-182, miR-196a miR-21*, miR-363, miR-20b.	**Significantly deregulated ALK+ vs T cells** miR-150, miR-150*, miR-451, miR-141, **miR-**146a, **miR-26a,** miR-151-5p, miR-361-3p, miR-342-5p, miR-101, miR-29c	[79]

Table 2. Distinct mi-RNA signatures to distinguish ALK+ ALCL from ALK− ALCL.

Sample	Technique	Upregulated	Downregulated	Reference
ALCL primary tumors: 6 ALK+ ALCL 5 ALK− ALCL	Human miRNA Microarray version 3 (Agilent Technologies, Santa Clara, CA)	**Higher expression in ALK− ALCL** miR-486-5p, miR-500-3p, miR-629	**Lower expression in ALK− ALCL** miR-155, miR-29a, miR-29b, miR-720	83
ALCL primary tumors: 6 ALK+ ALCL 6 ALK− ALCL	Taq man Array Human MicroCard A v.2.0 (Thermo Fisher Scientific Carlsbad, CA, USA)	**Higher expression in ALK+ ALCL** miR-203, miR-376c, miR340, miR-224, miR-138, miR-505, miR-148a, miR-372, miR-598, let-7f, miR-454, miR374a, miR-374b, miR590-5p, miR-132, miR-199, miR-455, miR-145, miR-149	**Lower expression in ALK+ ALCL** miR-155, miR-570, miR-216a, miR-412, miR-381, miR-625, miR-377, miR-208b, miR-512-5p, miR-299, miR-615-5p, miR-147b, miR-515-3p, miR-520b, miR-511, miR-208, MiR-210, miR499-3p, miR-485-5p, miR-876-3p, miR-887, miR-369-3p, miR-423-5p, miR1-29-5p, miR-197, miR-328, miR-342-5p, miR-376b, miR380, miR450b, MIR491-3p, miR-499-5p, miR501-3p, miR-510, miR-518a, miR-518d, miR520d, miR524, miR-525, miR-544, miR-548a, miR556, miR561, miR-624, miR-654, miR-871, miR-872, miR-874, miR-876, miR-890, miR-891b, miR-892a, miR-147, miR-220b, miR-384, miR492, miR-509, miR-223, miR-453, miR-541, miR-296, miR-92a, miR325, miR-298, miR-92a, miR-325, miR-298, miR-483, miR-576, miR597, miR185, miR548c, miR-320, miR-324 miR-582, miR-636, miR-494, miR-548, miR-24, miR-618, miR-181c, **miR-181a,** miR-202, miR-548d, miR-136, miR-34a, miR-548b, miR-22, miR-125, miR-520a, miR-885, miR-516b, miR-518f, miR-548b, miR105, miR326, miR674, miR-507, miR-220c, miR-507, miR-220c, miR-526b, miR-520e, miR-523, miR-29a, miR-487, miR-508, miR-518c, miR-545, miR-885, miR-519e, miR-652, miR-517b	76
ALCL primary tumors: 8 ALK+ ALCL 5 ALK− ALCL	LNA-modified miRCURYLNA miRNA Array ready-to-spot probe set no.208010-A (Exiqon)	**Higher expression in ALK+ ALCL** miR135b, miR512-3p, miR-708, miR-886-5p	**Lower expression in ALK+ ALCL** **miR-146a,** miR-155	78
ALCL primary tumors: 8 ALK+ ALCL 5 ALK− ALCL	Next generation sequencing (Illumina)	Higher expression in ALK+ ALCL Vs ALK-ALCL and T cells miR-182, **miR-181a*,** miR-21, miR-363, miR-20b	**Lower expression in ALK+ ALCL Vs ALK-ALCL and T cells:** miR-155, **miR-146a,** miR-193b, **miR-26a,** miR-34a, miR-196a, miR-342-3p, **miR-181a.**	79.

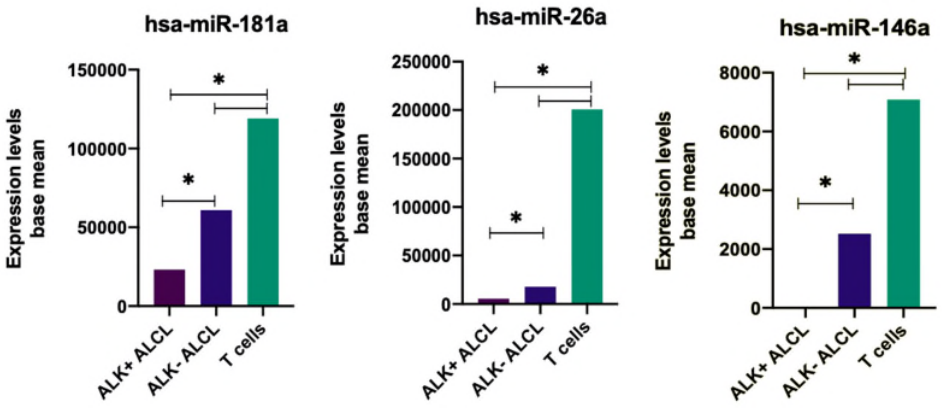

Figure 6. Deregulated miRNAs in ALCL.

Transcriptome analysis reveals a significant differential expression of miR-146a, miR-181a and miR-26a in T cells in comparison to ALK+ and ALK− ALCL Expression levels depicted as base means of triplicates of read counts. *p-value=<0.05. Data adapted from [79].

1.1.3.1.1 miR-181a.

The miR-181 family has been identified to be significantly regulated by the transcription factor C/EBPβ in ALCL [79]. The miR-181 family consists of four members: miR-181a, miR-181a*, miR-181b, and miR-181c. The reduced expression of miR-181 family has been related to carcinogenesis and adaptive immune response deregulation. MiR-181a is transcribed in chromosome 1 (1p) and is one of the most abundant miRNAs in lymphocytes, participating in the NF-κB, T cell differentiation [84], and as an inhibitor of the TCR signaling pathway [85-87]. miR-181a plays a dual role in different cancers, acting as an oncogene and tumor suppressor. In diffuse large B-cell lymphoma (DLBCL), this miRNA acts as a tumor suppressor, demonstrating that its low expression in activated B-cell (ABC-like) DLBCL, in comparison with germinal center B-cell (GCB-like) DLBCL, fails to target the NF-κB signaling, promoting oncogenesis and conferring chemoresistance antagonizing the apoptotic action of the therapy [88].

In other malignancies such as hepatic cancer, multiples myelomas, myelodysplastic syndrome, and acute myeloid leukemia (AML), the upregulation of miR-181a has been documented and related to an oncogenic role [84,89-92].

Since impaired TCR expression is a common feature of ALCL, miR-181a has emerged as a candidate target to study, given its potential involvement in TCR signaling. Indeed, its study may help us to understand the dysregulation of intracellular signaling pathways that control T cell activation and survival in ALCL [14].

1.1.3.1.2 miR-26.

A variety of other miRNAs with less known functions, such as miR-26a, may also play a role in lymphomagenesis in ALK+ ALCL [79]. The immature miR-26a-1 and -2 are codified in chromosomes 3 and 12. The mature sequence of these immature miRNAs contains an identical sequence. Like other miRNAs, miR-26a functions as a tumor suppressor in nasopharyngeal, breast, and hepatic carcinoma, whereas in glioma and T-cell acute lymphoblastic lymphoma acts as an oncogene [93].

Some miR-26a functions are related to cell proliferation and apoptosis through the regulation of phosphatase and tensin homolog (*PTEN*) and *BCL-2* in tumoral cells [94,95]. Particularly, in lung carcinoma, where miR-26a enhances metastases by targeting the PTEN/AKT/NFκB pathway [96]. In cardiovascular diseases, miR-26a also participated in signaling pathway related to angiogenesis and endothelial cell growth [97]. However, in osteogenesis, it seems to play a more complex role since the transcription factor *C/EBPα* is described as a target gene of miR-26a, and this miRNA is also regulated by the *C/EBP* transcription factor creating a feedback loop [98]. Another miR-26a target is CD38; the inhibition of CD38 by miR-26a results in repressed proliferation and apoptosis in xenografts models of myeloma multiple, highlighting miR-26a as a promising therapy in this neoplasia [99]. Finally, the roles of miR-26a in T cell activation, angiogenesis, and oncogenesis in tumoral cells and T regulatory cells highlight it as a potential target in the lymphomagenesis in ALK+ ALCL [100,101].

1.1.3.1.3 miR-146a.

The gene of miR-146a is located on chromosome 5 and transcribed into two mature miRNAs: miR-146a-5p and miR-146a-3p [102]. MiR-146a 5p is the best characterized, and since its discovery, its function has been related to the innate immune response to microbial infections as the principal regulator of multiple pro-inflammatory processes [102]. Moreover, multiple putative transcription factor binding sites have been identified in the miR-146a promotor region in the last decades, including the *C/EBPβ* transcription factor (Figure 7).

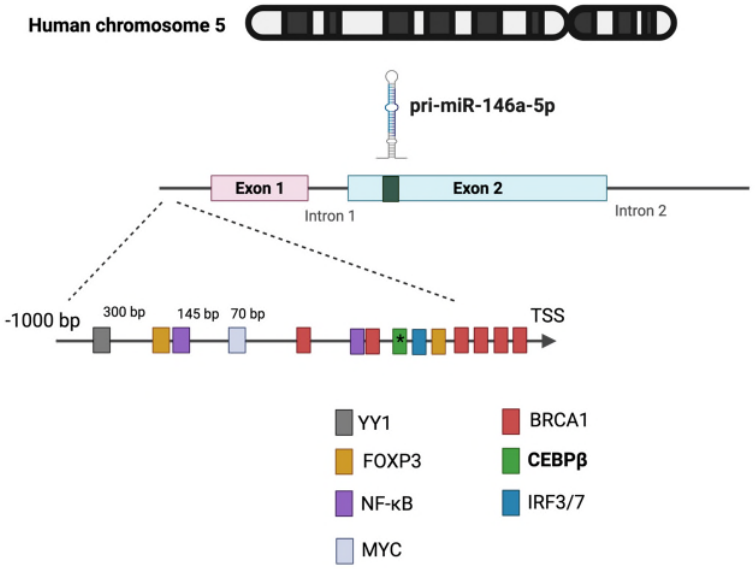

Figure 7. MiR-146a gene and its promotor region.

Transcription factors regulating miR-146a are illustrated; their putative binding sites are confirmed 1000 bp upstream of the transcriptional start site (TSS) in different cell lines [103]. The figure was created using BioRender.com.

Further studies also identified its role in the Th1 (T-helper) phenotype in the adaptive immune response and tumorigenesis [104-106]. Interestingly, the absence or lack of miR-146a results in the overexpression of TNF-alfa and IL-6, stimulating inflammation, disturbing normal hematopoiesis, and promoting the development of myeloid malignancies [107,108].

In cancer, miR-146a provides a dual function, working as a tumor suppressor in certain cancers but as an oncogenic miRNA in others [103]. Its main targets result in the regulation of key signaling pathways involved in cell proliferation and inflammation, including NOTCH, NF-kB, TGFB, EGFR, arachidonic acid, PI3K, and VEFG [103]. In acute lymphoid leukemia (ALL), AML, and T-cell lymphoma, miR-146a seems to play a role as an oncomir, whereas in B-cell lymphomas and myeloid malignancies acts as a tumor suppressor.

On the other hand, miR-146a demonstrates low levels in tissues acting as a tumor suppressor, resulting in poor outcome in cases with NK cell and T cell malignant lymphoproliferation. Restoring its function *in vitro* results in NF-κB signaling inhibition through TNF receptor-associated factor 6 (*TRAF6*), avoiding cell proliferation and activating apoptosis [109]. Some of the central target genes of miR-146a studied in different cancers comprise the previously mentioned *TRAF6*, interleukin 1 receptor-associated kinase 1 (*IRAK1*), epidermal growth factor receptor (*EGFR*), NOTCH receptor, arachidonate 5-lipoxygenase activating protein (*ALOX5AP*), caspase recruitment domain family member 10 (*CARD10*), ras homolog family member A (*RHOA*), *CD147* or Basigin (*BSG*), among others [103].

Intriguingly, miR-146a is significantly downregulated in ALK+ ALCL compared to ALK− ALCL [79]. Moreover, miR-146a is also significantly downregulated in comparison to normal T cells, suggesting the leading role as a tumor suppressor miRNA in the pathogenesis of ALCL [79].

In order to investigate the role of miR-146a in ALK+ ALCL, the identification of its target genes was performed using transcriptome analysis by comparing ALK+ ALCL cells with miR-146a overexpression with ALK+ ALCL cells with inherently low expression of miR-146a. The analysis resulted in the identification of four targets genes, including *ZNF275* (zinc finger protein 275), *SRPRB* (signal recognition particle receptor, B subunit), *PNPO* (pyridoxamine 5'-phosphate oxidase), and *CD147*. *In silico* and *in vitro analyses* were further performed to recognize the direct target genes of miR-146a by luciferase reporter assay, demonstrating SRPRB as a direct target gene of miR-146a in HEK293T cells, but failing to demonstrate the direct association of miR-146a and CD147 [110,111]. However, in other cancers, such as hepatocellular carcinoma (HCC), the transmembrane gly-

coprotein CD147 was previously reported as an crucial oncogenic protein and a direct target of miR-146a [112].

1.1.3.1.3.1 CD147, a potential miR-146a target gene.

CD147, also known as extracellular matrix metalloproteinase inducer (EMMPRIN), hepatoma-associated antigen (Hab18G), or Basigin (BSG), is a member of the immunoglobulin family. Its gene is located on chromosome 19 at p13.3, comprising ten exons [113,114].

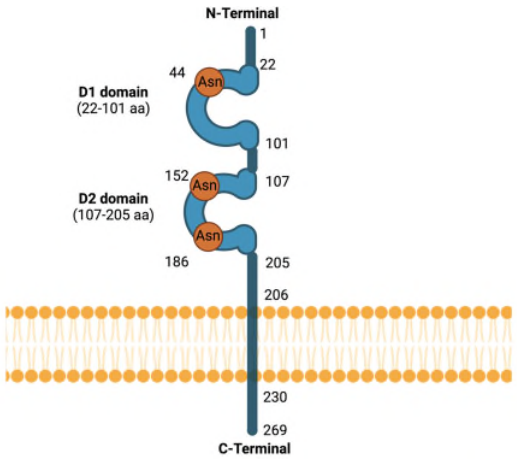

Figure 8. CD147 protein structure

CD147 has a signal domain, an extracellular domain, a transmembrane domain, and a cytoplasmic domain [115]. The figure was adapted by [115] and created using BioRender.com.

Four variants of CD147 have been described (BSG 1,2,3 and 4). BSG 2 is the most abundant and best-characterized isoform, which is also referred to as CD147. Its mRNA transcripts encode a protein of 269 amino acids (aa), containing an extracellular portion with 2 Ig-like domains at the N-terminus, a transmembrane domain of 24 aa, and a cytoplasmatic domain of 39 aa [116].

CD147 is widely distributed in many stromal cells, such as fibroblasts and epithelial cells, and is highly enriched in the surface of a variety of malignant tumor cells [117]. In addition, CD147 is involved in the invasion and metastasis of tumors by

promoting cell adhesion, migration, and degradation of the extracellular matrix (ECM) [115].

On the one hand, CD147 stimulates the secretion of metalloproteinases (MMP)1, 3, and 9 in melanoma, which leads to the degradation of ECM in melanoma and breast carcinoma [118,119]. On the other hand, it also induces invasion by overexpressing the urokinase-plasminogen activator system [120], activating the EGFR-RAS-ERK pathway via CD147-hyaluronan-CD44 interaction [121] and triggering the NF-kB pathway [122].

CD147 likewise induces angiogenesis by enhancing vascular endothelial growth factor (*VEFG*) and *MMP* expression levels [123]. Upregulation of *VEFG* and its receptor VEGFR-2 is mediated by the HIF-2 alpha transcription factor, a CD147 target. Interestingly, CD147 participates in the cells' metabolism by reprogramming glycolytic energy metabolism.

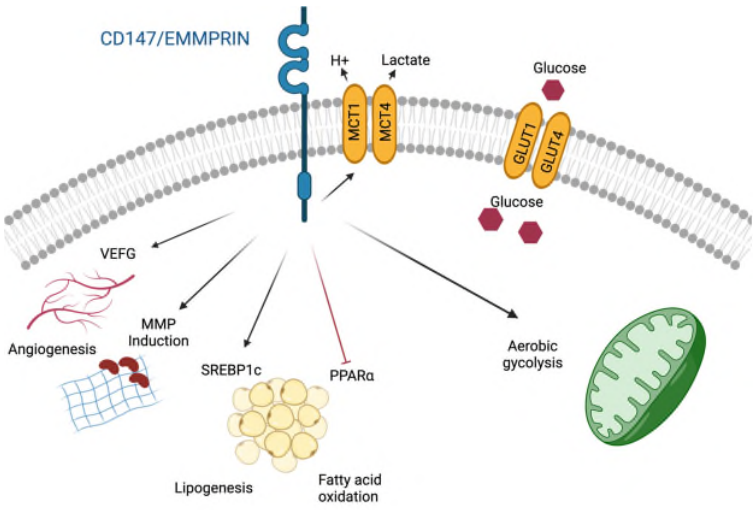

Figure 9. The pleiotropic functions of CD147.

CD147 activation drives different biological pathways, including matrix degradation, aerobic glycolysis promoting energy metabolism, activation of MCTs triggering lactate efflux, lipogenesis, and fatty acid oxidation [124]. The figure was created using BioRender.com.

Abbreviations: MCTs, monocarboxylate transporters; MMP, metalloproteinase; GLUT4, SREBP1c, sterol regulatory element-binding protein; glucose transporter-4; PPAR-α, Peroxisome proliferator-activated receptor alpha.

CD147 forms a complex with the monocarboxil transporter-1 (MCT-1) and MCT4 on the membrane to allow lactate efflux produced by anaerobic glycolysis [125]. The function of CD147 in glycolysis reprogramming has been studied, and gain and loss of function analysis [126]. Baba *et al.* established that CD147 silencing leads to a striking decrease in energy metabolism, promoting cell proliferation [127,128]. CD147 stimulates metabolic reprogramming by inhibition of p53 and activation of the PIK3/AKT/MDM2 signaling pathway [128].

In order to proliferate rapidly, tumor cells not only require high energy consumption and lactic acid efflux, but they also need a high demand for phospholipid synthesis. Interestingly, CD147 expression is linked to lipogenesis, stimulating the transcription factor *SREBP1c* as well as other downstream genes, which encode lipogenic enzymes [124]. Furthermore, CD147 similarly contributes to chemoresistance by activation of PIK3 and MAPK signaling pathways [125]. In our working group, Schmidt *et al.* exposed the differential expression of CD147 in ALK+ versus ALK− ALCL *in vitro* and *in vivo*, becoming CD147 a suitable protein to study in ALCL (Figure 10) [34].

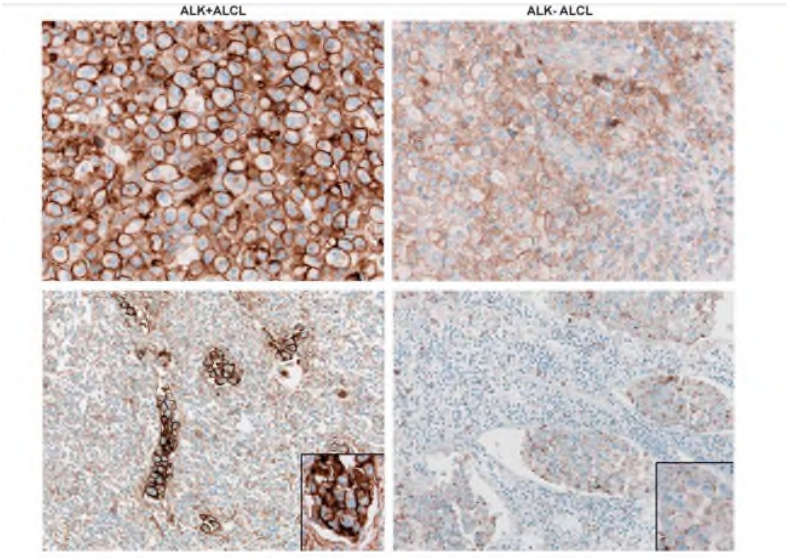

Figure 10. CD147 is differentially expressed in ALK+ and ALK- ALCL using immunohistochemistry.

CD147 Immunohistochemistry in primary patients' samples of ALK+ and ALK− ALCL. ALK+ ALCL cases show stark expression in comparison to ALK ALCL, independently of the infiltration pattern (diffuse (upper) or sinusoidal (lower panel). Immunohistochemistry x400 upper panel, x200, lower panel, and insert x400. Data reproduced from [34].

1.1.4 Prognosis.

In previous studies, ALK+ ALCL was shown to have a better prognosis than ALK- ALCL and other peripheral T-cell lymphomas (PTCL). However, in studies stratifying ALCL by age and stage of diagnosis, a similar prognosis for these entities was observed for these entities [129]. ALK+ ALCL shows a 70-90% overall survival rate compared to the 40-60% rate exhibited in ALK− ALCL. Main genetic alterations are observed in ALCL and directly correlate with patient outcomes. ALCL cases with ALK translocation show a 70% of 5-year overall survival rates, whereas ALCL cases lacking ALK translocations but showing DUSP22 or TP63 rearrangements exhibit 90 and 17% five-year overall survival rate, respectively [130]. Nevertheless, ALK− ALCL patients lacking DUSP22 and TP63 translocations demonstrate a 42% overall survival rate and a worse prognosis than ALK+ ALCL [131,132]. The International Prognostic Index (IPI) is a helpful predictor of outcome in aggressive lymphomas, which is useful in ALCL patients [133]. This tool considers diverse variables, including age, ECOG performance status, LDH level, Ann Arbor stage, and extranodal involvement. This score defines four risk groups: IPI: score 0–1, low risk; score 2, low-intermediate risk; score 3, high-intermediate risk; and score 4–5, high risk. The high-risk group shows a 33% five-year overall survival rate versus the 23%, 68%, and 90% observed in the high-intermediate, low-intermediate, and low-risk groups, correspondingly [9]. In recent years, additional prognostic markers have been identified, including CD56 expression, elevated CD30 levels in serum, and elevated beta2 microglobulin (> 3mg/L).

1.1.5 Therapy.

Cyclophosphamide, doxorubicin, vincristine and prednisone (CHOP) is the standard treatment for all aggressive lymphomas, including ALCL [9]. However, cases with IPI scores >3 or younger patients (<60 years old) benefit from the addition of etoposide (CHOEP) to the standard CHOP therapy [134,135]. Other alternative regimens include hyperfractionated cyclophosphamide, vincristine, doxorubicin, dexamethasone, methotrexate, and cytarabine (hyperCVAD) also exist, but until now, they have not displayed a better outcome [136]. More recently, brentuximab vedotin (Adcetris) in combination with cyclophosphamide, doxorubicin, and pred-

nisone (B-CHP) has revealed greater results in comparison to standard CHOP chemotherapy [137]. ALCL relapse is relatively common and present in around 40% to 65% cases [9]. Once patients relapsed, they struggled with the limitations of chemotherapy because it had toxic side effects, and patients had failed to respond to conventional chemotherapy. High-dose therapy and autologous stem cell transplantation (SCT) can improve long-term remission in 30 to 40% of patients; however, this therapy is only optional for patients with chemotherapy-sensitive diseases [138]. Unfortunately, there is no standard treatment for patients with disease relapse, SCT failure or patients who do not respond to primary chemotherapy. Brentuximab vedotin (Adcetris), an antibody-drug conjugate targeting CD30, may represent the best treatment option for patients with relapsed or systemic ALCL after the failure of at least one prior multiagent chemotherapy regimen, showing a high and complete response in 57% of the patients with a median of 13 months of progression-free survival (PFS) [133,139,140].

In recent years, new research has focused on the number of novel drugs and targets for treating ALCL. For example, Crizotinib, an ALK and c-met inhibitor has shown an efficient antitumor activity [141]. Nevertheless, the probability of resistance to the inhibitor due to mutant forms of the ALK protein is high, leading to new disease relapse problems. Therefore, developing other drugs that will act synergistically with ALK inhibitors is needed to prevent disease recurrence.

1.2 Aim of the project.

- This work aimed to characterize the role of the *C/EBPβ*- or ALK-dependent miRNA (miR-181a, miR-26a, and miR-146a) in ALCL by identifying their target genes and further analyzing their relevant candidates.

The NPM-ALK fusion protein results in the constitutive expression of ALK kinase, the major oncogenic mechanism in ALCL. Through its transforming ability, it is previously known, that NPM-ALK activates signaling pathways related to cell proliferation, differentiation, and survival, including RAS/MAPK, PLCγ, PI3K, and JAK/STAT [142-147]. In addition, a large number of genes that are regulated by ALK have been described, including *C/EBPβ*, a gene that is involved in a variety of cellular processes, including differentiation, proliferation, inflammatory response, and metabolism. [48]. In ALCL, *C/EBPβ* has been confirmed to be overexpressed as a result of NPM-ALK kinase activity and plays an important role in ALK-mediated oncogenesis [33,42,79]. Moreover, ALK and C/EBPβ have been proven to regulate gene expression through induction of miRNA [56,57,78,105,148,149]. Several studies have identified different miRNA signatures characteristic for ALK+ ALCL, highlighting miR-155, miR-181a, miR-210, miR-29a/b, miR-342-5p/3p, miR-369-3p miR-374a/b, miR-423-5p, miR-625, miR-205, miR-146a, and miR-26a as significantly downregulated miRNAs in ALK+ ALCL [150] in comparison to ALK− ALCL; however, from those only miR-181a was *C/EBPβ* dependent. By next generation sequencing (NGS), Steinhilber *et al*. recognized miR-181a, miR-26a, and miR-146a as potential deregulated miRNA targets in ALK+ ALCL, demonstrating a 5- to 244-fold higher expression in normal T cells, as well as 2- to 87-fold higher in ALK− ALCL, in comparison to ALK+ ALCL cell lines [79]. In normal T cells, these miRNAs' lower expression has been associated with adaptive immune response deregulation, angiogenesis, and tumor progression, revealing a potential role in ALK+ ALCL tumorigenesis [151-153].

In this thesis, we aimed to investigate the functions of miR-181a and miR-26a. To fulfill this goal, we have identified their target genes by transcriptome analysis using NGS to distinguish the significantly downregulated genes after miRNA

(miR-181a, miR-26a) overexpression in ALK+ ALCL cell lines through transient transfection. Moreover, gene ontology and pathway analyses of the significantly regulated genes were performed to identify the main pathways related to the miRNA functions. Their candidate target genes were validated at the RNA level by RT-qPCR and at protein levels by Western Blot (WB). In addition, the identification of target gene expression levels in normal lymph nodes and in ALK+ and ALK− ALCL primary patient samples were analyzed by immunohistochemistry and RT-qPCR.

Furthermore, screening of miR-146a target genes by transcriptome analysis was already investigated in our working group by Steinhilber et al., detecting *CD147* as one of the top candidates for regulating tumor growth, metabolism, cell invasion, and angiogenesis in ALK+ ALCL. Since miR-146a appears as a tumor suppressor by targeting *CD147*, the current study aimed to further investigate the role of CD147 in ALCL and its relationship with ALK and miR-146a. To this end, we studied the binding sites "*in silico"* of miR146a in *CD147* with bioinformatics tools and confirmed it *in vitro* by luciferase reporter assay. CD147 was silenced using two different approaches, CRISPR/ Cas9 knockout (KO) and shRNA knockdown (KD) in ALK+ ALCL cell lines (SUDHL1, KiJK). *In vitro* and *in vivo* experiments were performed to assess tumor cell viability and growth retardation after CD147-KD. Metabolomic analysis and mitochondrial potential were also evaluated since CD147 appears to play an important function in energy metabolism in this lymphoma.

2. Material and methods.

2.1. List of the materials.

2.1.1.1 Antibodies.

Table 3. Primary antibodies.

Immunohistochemistry:				
Primary antibodies	Clone	Dilution	Staining	Company
ALK-1	M7195	1:400	Nucleus cy-	Dako
CD147	MEM-M6/1	1:1500	Membrane	Abcam
CD30	Ber-H2	1:30	Cytoplasm	Dako
CD31	JC70A	1:1500	Membrane	Dako
CD93	HPA009300	1:800	Membrane	Sigma-Aldrich
GLUT3	15311	1:800	Cytoplasm	Abcam
MCT1	H1	1:250	Cytoplasm	Santa Cruz
MMP7	Poly Rabbit	1:5000	Cytoplasm	Abcam
p53	DO-7	1:400	Nucleus	Novocastra
P-STAT3	Y705	1:500	Cytoplasm	Cell Signaling
VEGFR2	55B11	1:50	Cytoplasm	Cell Signaling
Western Blot:				
Primary antibodies	**Clone**	**Dilution**	**Specie**	**Company**
ALK	45C5B8	1:1000	Mouse	Termo Fisher Scien-
a-Tubulin	DM1A	1:50000	Mouse	Sigma-Aldrich
CD147 (BSG)	HIM6	1:100	Mouse	BD Biosciences
CD30	Ber-H2	1:300	Mouse	Dako
CD93	HPA009300	1:500	Mouse	Sigma-Aldrich
GLUT3	15311	1:400	Mouse	Abcam
MCT1 (H1)	SC365501	1:100	Mouse	Santa Cruz
P-STAT1 (Tyr701)	9167S	1:1000	Rabbit	Cell Signaling
P-STAT3 (Tyr705)	9138	1:750	Mouse	Cell Signaling
P-STAT5	716900	1:1000	Rabbit	Thermo Fisher Scien-
Secondary Antibodies				
ECL anti-rabbit IgG HRP-linked	NA931	1:1000	Sheep	Amersham
ECL anti-mouse IgG HRP-	NA934	1:3000	Donkey	Amersham
IRDye® 800CW anti-Mouse IgG	926-32212	1:10000	Donkey	LiCOR
IRDye® 800CW anti-Rabbit IgG	926-32212	1:15000	Donkey	LiCOR

2.1.1.2 Buffers.

Table 4. Buffers.

Western Blot Buffers		
Laemmli 2x Concentrate	50 ml	Sigma-Aldrich
4% SDS	20 ml	Sigma-Aldrich
20% 2-Beta-Mercaptoethanol	10 ml	Sigma-Aldrich
10% Glycerol	5 ml	Sigma-Aldrich
0.1 M Tris (pH=6.8)	5 ml (1 M Tris)	AppliChem
0.01% Bromophenol blue	0.005 g	Sigma-Aldrich
Ponceau S		
1.5 M Ponceau S	0.5 g	Sigma-Aldrich
1% Acetic acid	1 ml	Merck
Distilled water	100 ml	
Protein Lysis Buffer	700 µl	
0.85 V T-Per	600 µl	Thermo Fisher Scientific
0.14 V Complete Mini (7x)	100 µl	Roche Diagnostics
0.1 V Phosphatase Inhibitor Cocktail	7 µl	Thermo Fisher Scientific
5% Skim milk/TBS-T	50 ml	
Milk powder	2.5 g	
TBS-T buffer	50 ml	
3% Bovine Serum Albumin/TBS-T	50 ml	
Bovine Serum Albumin	1.5 g	Sigma-Aldrich
TBS-T buffer	50 ml	
TBS/TBS-T buffer (10x) (pH 7.6	1000 nl	
0.2 M Trizma Base	24.2 g	Sigma-Aldrich
1.4 M NaCl pH 7.6	80.2 g	Merck
1% Tween 20	10 ml	Sigma-Aldrich
Transfer buffer (10x) (pH 8.3)	1000 ml	
0.25 M Tris	31.2 g	Sigma-Aldrich
2 M Glycine	144 g	Sigma-Aldrich
XT-MES running Puffer (20x)		Bio-Rad
TBS-T Buffer (10x) (pH 7.6)		
10x Buffer II + 25 mM $MgCl_2$		

2.1.1.3 Cells.

Table 5. Cells.

Cell line	Company	Identifier
Adherent cells		
Cervix carcinoma		
HeLa	DSMZ-German Collection of Microorganisms and Cell Cultures GmbH	DSMZ; ACC-57
Embryonal Kidney		
HEK293	DSMZ-German Collection of Microorganisms and Cell Cultures GmbH	DSMZ; ACC 293
Suspension cells		
ALK− ALCL		
Mac-1	Provided by Eva Geißinger (University of Würzburg, Germany	
Mac2 and Fe-PD	Olaf Merkel (Medical University Vienna, Wien, Austria)	
ALK+ ALCL		
SR-786	Provided by Mark Raffeld (National Cancer Institute, NIH, Bethesda, MD, USA),	
SUDHL-1	DSMZ-German Collection of Microorganisms and Cell Cultures GmbH	DSMZ; ACC 356
Karpas 299		DSMZ; ACC-31
KiJK		DSMZ; ACC-695
SUP-M2	DSMZ-German Collection of Microorganisms and Cell Cultures GmbH	DSMZ; ACC-509
Diffuse Large B-cell lymphoma		
SUDHL-4	DSMZ-German Collection of Microorganisms and Cell Cultures GmbH	DSMZ; ACC 495
Mantle cell lymphoma cells		
Jeko-1 and Rec-1	Donated by Dr. Dolors Colomer (University of Barcelona, Spain)	
Multiple myeloma		
KMS-12	DSMZ-German Collection of Microorganisms and Cell Cultures GmbH	DSMZ; ACC 551
Promyelocytic leukemia cell line		
HL-60	DSMZ-German Collection of Microorganisms and Cell Cultures GmbH	DSMZ; ACC 3
T-cell acute lymphoblastic lymphoma		
Jurkat	DSMZ-German Collection of Microorganisms and Cell Cultures GmbH	DSMZ; ACC 282

2.1.1.4 Chemicals and Equipment.

Table 6. Chemicals and equipment.

Chemicals	Company
2-Mercaptoethanol	Sigma-Aldrich
Chloroform	VWR
Chloroform / isoamyl alcohol	Roth
EDTA	AppliChem
Ethanol	Merck
Isopropanol	AppliChem
Lithium Chloride	AppliChem
Phenol: chloroform: isoamyl alcohol (25:24:1)	Roth
Tween 20	Sigma-Aldrich
Equipment	**Company**
Automated Immunostainer	Ventana Medical Systems
Axiostar Plus Microscope	Zeiss
Balance	Sartorius
Biofuge fresco	Thermo Fisher Scientific
Centrifuge/Vortex Combi-Spin FVL2400	Peqlab
Counting chamber Neubauer improved	Hecht Assistent
FACS CAlibur	Becton Dickinson
Fluorescence microscope Axiovert 135	Carl Zeiss
Gel chamber Criterion	Bio-rad
Gel documentation system CN-300-WL/LC	Peqlab
Gene Touch Thermal Cycler Chassis	Biozym
Gene Amp PCR System 9700	Applied Biosystems
Genome Lab GeXP Genetic Analysis System	Beckman Coulter
Heating block	Liebisch
IMARK Microplate Reader	Bio-Rad
Incubator B6030	Thermo Fisher Scientific
Invertoscope	Carl Zeiss
Light Cycler 480 System	Roche Diagnostics
Magnetic stirrer MR2000	Heidol
Megafuge 1.0	Thermo Fisher Scientific
Microfuge 16 microcentrifuge	Beckman Coulter
Microtome	Microm International GmbH
Microwave 800	Severin
Mini vacuum and compressor	
Minicentrifuge	Neolab Heildelberg

Mixer Uzusio VTX 3000	LMS
Multifuge 1L-R Centrifuge	Thermo Fisher Scientific
Nanodrop 2000 Spectrophotometer	Thermo Fisher Scientific
PCR Work-station with UV/Air circulator	
Pipette	Gilson, Eppendorf
Qubit 3.0 Fluorometer	Thermo Fisher Scientific
Shaking incubator	Infors HT Ecotron
Shaking incubator thriller	Peqlab
Thermo Cycler	Applied Biosystems
TriStar LB941	Berthold Technologies
Vortexer	Biozym
Water bath	GLF

2.1.1.5 Consumables.

Consumables were purchased from Eppendorf, Merck Millipore, neoLab, Biozym, GE Healthcare, Falcon, SARSTEDT, OMNILAB, Roth, Roche Diagnostics, Greiner Bio-One, BD Biosciences, Becton Dickinson, Bio-Rad, and Thermo Fisher Scientific.

2.1.1.6 Enzymes.

Table 7. Enzymes.

Enzyme	Company
AmpliTaq Gold DNA Polymerase	Thermo Fisher Scientific
BsmBI (Esp3I) fast Digest	Thermo Fisher Scientific
Proteinase K	Promega
rDNase I	Thermo Fisher Scientific
RNase OUT	Thermo Fisher Scientific
Sac I fast Digest	Thermo Fisher Scientific
SbfI fast Digest	Thermo Fisher Scientific
Super Script II Reverse Transcriptase	Thermo Fisher Scientific
Uracil-DNA Glycosylase	Roche Diagnostics

2.1.1.7 Kits.

Table 8. Kits.

Kit	Company
BCA Protein assay reagent	Thermo Fisher Scientific
DNA-free kit ™	Thermo Fisher Scientific
Genome Lab DTCS Quick Start Kit	Beckman Coulter
innuPREP DOUBLEpure Kit	Analytik Jena
miRNeasy MiniKit	Qiagen
miScript II RT Kit	Qiagen
miScript SYBR green PCR KIt	Qiagen
Pierce BCA Protein Assay Kit	Thermo Fisher Scientific
PureYield Plasmid Midi Kit	Promega
PureYield Plasmid Miniprep System	Promega
QIAprep Spin Miniprep Kit	Promega
QIAquick Gel Extraction Kit	Qiagen
QIAshredder	Qiagen
QuantiTect SYBR Green PCR Kit	Qiagen
Quick ligation Kit	New England BioLabs
Rapid DNA Dephos & Ligation Kit	Roche Diagnostics
RNeasy MiniKit	Qiagen
Steril-Filter Millex HV (0.45 µm)	Merck/Millipore
Universal Probe Library Set Human	Roche Diagnostics
Vivaspin 20	VWR
Sequencing Kits	
High Prep Cleaning Beads	Thermo Fisher Scientific
Ion AmpliSeq Library Kit 2.0-96 LV:	Thermo Fisher Scientific
Qubit® dsDNA HS Assay Kit:	Thermo Fisher Scientific

2.1.1.8 Media and additives.

Table 9. Media and additives.

Media and additives for bacterial cultures	
Ampicillin- Na salt	Sigma-Aldrich
LB-Agar	Affymetrix
LB-Broth Base Medium	Thermo Fisher Scientific
LE-Agarose	Biozym
SOC Medium	Thermo Fisher Scientific
Media and additives for cell culture	
Bortezomib	
Crizotinib (PF-02341066)	Med Chem Express
DMEM (1x) + GlutaMax - I	Thermo Fisher Scientific
DMSO solution	Sigma-Aldrich
FCS Fetal Bovine Serum Gold	Biochrom KG
FCS Fetal Bovine Serum Gold (5%)	Gibco BRL
Oligomycin A	Sigma-Aldrich
Opti-Mem	Thermo Fisher Scientific
Penicillin/Streptomycin	Thermo Fisher Scientific
RPMI 1640 + Gluta MAX	Gibco BRL
Trypsin-EDTA	PAA

2.1.1.7 Plasmids and Bacteria.

Table 10. Plasmids and bacteria.

Plasmid/ Bacteria	**Company**
DH5α Competent Cells	Thermo Fisher Scientific
FUGW	
lentiCRISPRv2	Addgene
One Shot TM Stbl3 Tm chemically Competent E. coli	Invitrogen
One Shot™ TOP10 Chemically Competent E. coli	Thermo Fisher Scientific
p-CMV Δ R8.9	
pmirGLO Dual-Luciferase	Promega
pSuper	Promega
VSV-G	Promega
psPAX2	Addgene (12260)
pMD2G	Addgene (12259)

2.1.1.8 Patient material.

Formalin fixed, paraffin embedded (FFPE) human tissues from primary ALK+ and ALK- ALCLs and reactive lymph nodes were taken from the archives of the Institute of Pathology, University of Tübingen and University of Kiel, Germany. All the cases were completely immunophenotyped during diagnostic work-up and classified following the recommendations of the WHO classification for tumors of hematopoietic and lymphoid tissues [154]. The University of Tübingen granted ethical approval for the study (620/2011BO2).

2.1.1.9 Primers.

Table 11. Primers.

cDNA synthesis			
10x miScript Primer as-	Qiagen		
10x miScript Universal	Qiagen		
Hsa_miR-146a_1	Qiagen		
Hsa_miR-181a_1	Qiagen		
Hsa_miR-26a_1	Qiagen		
Oligo (dT) primer	Promega		
Random hexamer pri-	Thermo Fisher Scientific		
RT q PCR. Confirmation of the target genes. UPL Primer with their according probe			
ID	**Sequence (F 5 to 3´ or R 3 to 5´)**	**Probe**	**Reference**
ADAM19_F	GCCTATGCCCCCTGAGAG	78	*GAPDH*
ADAM19_R	TCTGTCTGCAGCAGTAGTACATCA		
ADAMTSL4_F	CGATGGAGAACTGGACTGG	84	*GAPDH*
ADAMTSL4_R	TGTAGGTGTCTGAAGAGAGTGTCC		
BCL9L_F	CCTCCCTCGCAGTTCGTAT	34	*GAPDH*
BCL9L_R	GTAGGCGAGGATGGAGTCG		
CACNA2D4_F	GCTTCTAGGCACCTCCCTGT	6	*GAPDH*
CACNA2D4_R	GTCAGCCCATAGCTTCACTGT		
CD147_F	GGGAGAGTACTCCTGCGTCTT	42	*ACTB*
CD147_R	ACTTCACAGCCTTCACTCTGG		
CD93_F	AGGCAAGACCAACCACATCT	13	*GAPDH* and *ACTB*
CD93_R	CAATGACGATGACGCTTAGG		
CHAC-1_F	GAAGTTTACGACGCCCAGAG	37	*GAPDH* and *ACTB*
CHAC-1_R	CACAGACTCAGTCCCAAGTCG		
CLU_F	CAACCACCGAAATCCGACT	16	*GAPDH* and *ACTB*

CLU_R	TGACTTTTCTCTGATGCACCTC		
COL16A1_F	CATGGGGCAAATACAGGTG	4	*GAPDH*
COL16A1_R	GGCTGGCAGGCTACTACTGT		
ITGA5_F	GGGGGCTTCAACTTAGACG	3	*GAPDH*
ITGA5_R	CTCCCACCAGCACACTGAC		
LINGO-1_F	GGTGTGGCTGAGACTCTGG	79	*ACTB*
LINGO-1_R	GCTCTCTCCACTGACTGTGCT		
MAPK13_F	TGGTGTATCAGATGCTCAAAGG	76	*GAPDH*
MAPK13_R	AGAATCTTCAGTTCACAGTCCTCA		
MCT1_F	GGGATTGGTGACCATTGTG	56	*GAPDH*
MCT1_R	CATGTCATTGAGCCGACCT		
OAF_F	CAGATCTGGGCTCGGCTAC	62	*GAPDH*
OAF_R	GGAGGCACAGAGAGGTCAAG		
PLEKHG5_F	CCCAGCCATGAAGAAGAAGT	74	*ACTB*
PLEKHG5_R	CAATGCCCTTCCTTTCAAAT		
PTPRC_F	GTATTTGTGACAGGGCAAAGC	73	*GAPDH*
PTPRC_R	GGTTTGGTGACTTGGATTGG		
SCD_F	CCTACCTGCAAGTTCTACACCTG	37	*GAPDH*
SCD_R	GACGATGAGCTCCTGCTGTT		
SLC2A3_F	GCCCTGAAAGTCCCAGATTT	35	*GAPDH*
SLC2A3_R	TTCATCTCCTGGATGTCTTGG		
SPON2_F	GCCTCGGGCTTAAATAGGAG	51	*ACTB*
SPON2_R	AGGAGGAGAGCGCAGAGG		
ST18_F	CCTCAGGACTTTGTGTTCATGT	41	*ACTB*
ST18_R	CACTGAGCTCCTGGATTAGTGA		
TAP1_F	CTCAGGGCTATGACACAGAGG	36	*ACTB*
TAP1_R	ACACGGTTTCCGGATCAAT		

Primers were designed using the Universal Primer Library Technology platform*. See section 2.2.2

***CD147* Cloning**	
Primers to amplify CD147 3UTR region (Insert)	
CD147 3UTR_F	AATGGAGCTCAGGTGGCCCGAGGA
CD147 3UTR_R	TCTACCTGCAGGGAGTCGAACACAGACCCGTGG
pmirGLO sequencing primers	
pmirGLO_F	TGACCGGCAAGTTGGACGCC
pmirGLO_R	GGCCGCCCCAAGGGGTTATG
***CD147* shRNA 5′ to 3′**	
A	AGCTTTTCCAAAAAGTCGTCAGAACACATCAACTCTCTTGAAGTTGATGTGTTCTGA
B	TGACAAAGGCAAGAACGTCTCTCTTGAAGACGTTCTTGCCTTTGTCA

C	AGCTTTTCCAAAAAGGTTCTTCGTGAGTTCCTCTCTCTTGAAGAGGAACTCACGAAG
D	AGCTTTTCCAAAAAGCTACACATTGAGAACCTGAATCTCTTGAATTCAGGTTCTCAA
E	GCTTTTCCAAAAAGGCTGTGAAGTCGTCAGAACATCTCTTGAATGTTCTGACGACTT
Primers for *CD147*/Sanger sequencing	
CD147CRISPRseqM13F	TGTAAAACGACGGCCAGTGGTTCCAGGCTCCTCTCTCT
CD147CRISPRseqpUC/M13	CAGGAAACAGCTATGACCTCCTTGGCTTCTCACCTTG
Primers for *CD147*-/NGS sequencing	
*CD147*_CRISPR_BC91_A_F	CCATCTCATCCCTGCGTGTCTCCGACTCAGCGGAAGGATGCG
*CD147*_CRISPR_BC91_A_	CCATCTCATCCCTGCGTGTCTCCGACTCAGCGGAAGGATGCG
*CD147*_CRISPR_trP1_F	CCTCTCTATGGGCAGTCGGTGATGGTTCCAGGCTCCTCTCTCT
*CD147*_CRISPR_trP1_R	CCTCTCTATGGGCAGTCGGTGATCTCCTTGGCTTCTCACCTTG

All primers design was performed using Primer 3 free available online software (v. 0.4.0)*. See section 2.2.2.6.3.3

sgRNa sequences for CRISPR/Cas 9 KO	
*CD147_F_*	CACCGGGGCAGCACCAGAATGACAA
*CD147_R_*	AAACTTGTCATTCTGGTGCTGCCCC
CD93_F	CACCGACACAAGGGTCCTTCCACTG
CD93_R	AAACCAGTGGAAGGACCCTTGTGT
GLUT_F	CACCGATGGTAAAACCCAGTAGCAG
GLUT_R	AAACCTGCTACTGGGTTTTACCAT

All primers design was performed using GUIDES design tool (Sanjana Lab, New York Genome Center) *. See section 2.2.6.1

* Oligonucleotides were subsequently synthetized by Sigma-Aldrich using the following specifications: desalt purification and 0.025 µmol concentrations. The dilution with distilled water was performed to reach the final stock 100 µM. concentration.

2.1.1.10 Reagents.

Table 12. Reagents.

Reagent	Company
2x QuantiTECT Sybr Green PCR Master Mix	Qiagen
480 Probes Master	Roche Diagnostics
5x First-Strand Buffer	Thermo Fisher Scientific
6x Loading Buffer	Thermo Fisher Scientific
BSA	Sigma-Aldrich
Buffer 10x Fast Digest	Thermo Fisher Scientific
Complete Mini	Roche Diagnostics
DNAse I Buffer	Thermo Fisher Scientific
Dnase/Rnase Free Water	Gibco

dNTPs	Fermentas
DTT	Thermo Fisher Scientific
Gel Red Nucleic Acid Stain	Biotium
Gene ruler 1 kb plus	Thermo Fisher Scientific
Gene ruler 100 bp	Thermo Fisher Scientific
Glycogen	Roche Diagnostics
HiPerfect Transfection Reagent	Qiagen
LE-Agarose	Lonza
Lipofectamine 2000	Thermo Fisher Scientific
Lipofectamine™ LTX Reagent with PLUS™ Reagent	Invitrogen
miRIDIAN microRNA Mimic Housekeeping Positive Thermo	Dharmacon
miRIDIAN microRNA Mimic miRNA 146a-5p	Dharmacon
miRIDIAN microRNA Mimic miRNA 181a-5p	Dharmacon
miRIDIAN microRNA Mimic miRNA 26a-5p	Dharmacon
miRIDIAN microRNA Mimic negatve control-1	Dharmacon
Mito Tracker Deep Red (MDR)	Thermo Fisher Scientific
Mito Tracker Green (MG)	Thermo Fisher Scientific
PBS	Thermo Fisher Scientific
Polybren	Sigma-Aldrich
Ponceau S	Sigma-Aldrich
Precision Protein StrepTracin-HRP conj.	Bio Rad
Propidiumiodid	Sigma-Aldrich
Protein marker Precision Plus Protein Standard	Bio-Rad
Pyruvat	Thermo Fisher Scientific
QIAzol Lysis Reagent	Qiagen
Randome hexamers	Roche Diagnostics
TaqMan Universal PCR Master Mix	Applied Biosystems
TBE Buffer (Tris, Oric acid, EDTA)	Sigma-Aldrich / Merck KGaA /Appli-
T-Per	Thermo Fisher Scientific
Trypan Blue	Sigma-Aldrich
Apoptosis analysis	
Annexin-V-Fluos Staining Kit	Roche Diagnostics
Citronensäure- Monohydrat	VWR
D-Saccharose	Fluka Chemie
Nonidet P-40	VWR
Propidium-Iodid (25mg)	Sigma-Aldrich
RNAse A	VWR

2.1.1.11 Software.

Table 13. Softwares.

Programme	Link- Company-Reference
Ensembl	https://www.ensembl.org European Molecular Biology Laboratory's European Bioinformatics Institute [155]
Cloning online sesource	https://www.embl.de European Molecular Biology Laboratory (EMBL)
Microsoft Office	Microsoft
EndNote X9	Clarivate Analytics
Universal Primer Library Technology platform	https://lifescience.roche.com/en_de/articles/Universal-ProbeLibrary-System-Assay-Design.html Roche
GUIDES design tool	http://guides.sanjanalab.org/ Sanjana Lab, New York Genome Center
Primer3web (Version 4.1.0)	https://bioinfo.ut.ee/primer3-0.4.0 Whitehead Institute for Biomedical Research
Integrative Genomics Viewer (Version 2.3)	https://igv.org/ Broad Institute [156]
GraphPad Prism (Version 8.0)	San Diego, CA, USA
Benchling (Molecular Biology)	https://www.benchling.com/molecular-biology/ San Francisco, CA, USA
MiRAnda	http://www.microrna.org/ Computational Biology Center, Memorial Sloan-Kettering Cancer Center, New York, NY, USA [157,158]
TargetScan 6.0	http://www.targetscan.org/vert_72 Whitehead Institute for Biomedical Research, Cambridge, MA, USA [159]
Rna22	https://cm.jefferson.edu/rna22 Computational Medicine Center, Sidney Kimmel Medical College, Thomas Jefferson University, PA, USA [160]
miRWalk	http://zmf.umm.uni-heidelberg.de/apps/zmf/mirwalk2/ Ruprecht-Karls-Universität Heidelberg, Medizinische Fakultät Mannheim, Germany[161]
miRmap	https://mirmap.ezlab.org University of Geneva Medical School, Geneva, Switzerland, Swiss Institute of Bioinformatics, Geneva, Switzerland and Imperial College London, South Kensington Campus, London, UK [162]
NCBI	https://www.ncbi.nlm.nih.gov National Center for Biotechnology Information, U.S. National Library of Medicine, Bethesda, USA
WinMDI 2.9 Software	Windows Multiple Document Interface software (WinMDI) is freeware designed by J. Trotter.
Reactome	https://reactome.org/ [163]
Panther	http://pantherdb.org/ [164]

2.1.1.12 Companies

Table 14. Companies

Companies	Location
Abcam	Cambridge, UK
Addgene	Watertown, Massachusetts, USA
Affymetrix	Santa Clara, California, USA
Amersham	Amersham, UK
Analytik Jena	Göttingen · Deutschland
Applied Biosystems	Schwerte, Nordrhein-Westfalen, Germany
BD Biosciences	Heidelberg, Germany
Beckman Coulter	Munich, Germany
Biochrom KG	Berlin, Germany
Bio-Rad	Feldkirchen, Germany
Biotium	Fremont, California, USA
Biozym	Niedersachsen, Germany
Cell Signaling	Danvers, Massachusetts, USA
Dako	Jena, Germany
Dharmacon	Buckinghamshire, United Kingdom
Fermentas	Leon-Rot, Germany
Fluka Chemie	Buchs, Switzerland
Gibco BRL	Karlsruhe, Germany
Hecht Assistent	Sondheim vor der Rhön, Deutschland
Invitrogen	Carlsbad, CA, USA
LiCOR	Lincoln, NE, USA.
Leica	Wetzlar, Germany
Lonza	Cologne, Germany
Med Chem Express	Beutelsbach, Bayern, Germany
Merck KGaA	Darmstadt, Germany
Novocastra	Wetzlar, Germany
Peqlab	Erlangen, Deutschland
Promega	Manheim, Germany
Qiagen	Hilden, Germany
Roche Diagnostics	Penzberg, Germany
Santa Cruz	Heidelberg, Germany
Sartorius	Göttingen, Deutschland
Sigma-Aldrich	Taufkirchen, Bayern, Germany
Thermo Fisher Scientific	Waltham, Massachusetts, USA
Ventana Medical Systems	Oro Valley, Arizona, USA
VWR	Radnor, Pennsylvania, USA
Zeiss	Jena, Deutschland

2.2. Methods.

2.2.1 Identification of miR-181a and miR-26a target genes in ALK+ ALCL cell lines.

2.2.1.1 Cell culture.

Suspension cell lines (Section 2.1.1.3, table 5) were supplemented with 10% fetal calf serum, 2 mM glutamine, 100 µg/ml penicillin, and 100 µg/ml streptomycin (Thermo Fisher Scientific), (See section 2.1.1.8, table 9). These cells must be passaged every two days to maintain a density of 0.3-1.0 x 10^6 cells/ml.

Adherent cells were supplemented with DMEM (High Glucose, GlutaMAX, Thermofisher Scientific) containing 10% FBS (PAA) and 1% penicillin-streptomycin (Thermo Fisher Scientific), (Table 9). These cells were passaged every two days in a 1:10 ratio to achieve a density of 0.3-1.0 x 10^6 cells/ml. For this purpose, the cells were washed with PBS (Thermo Fisher Scientific) and detached from the bottom of the cell culture flask (Greiner Bio-One) with trypsin-EDTA (PAA) (approximately 5 ml per 175 cm^2). The trypsin-EDTA reaction was stopped by adding fresh DMEM medium.

2.2.1.2 MiRNA Transfection.

To overexpress miR-146a, miR-181a, and miR-26a in ALK+ ALCL cell lines. miRNA mimic transfection was performed by triplicates. SUDHL-1 and Karpas 299 cells were seeded prior to transfection in 24-well plate (1 × 10^8 per well). Media were replaced with antibiotics-free media. Synthetic miRNA mimics: hsa-miR-146a-5p, hsa-miR-181a-5p, and hsa-miR-26a-5p, miRIDIAN (GE Healthcare Dharmacon), (Section 2.1.1.9, table 11) were transfected into cells following the Hiperfect transfection reagent protocol (Qiagen), (Section 2.1.1.10, table 12). In parallel, the microRNA mimic housekeeping positive control #2 (*GAPDH,* glyceraldehyde-3-phosphate dehydrogenase, Dharmacon) and microRNA Mimic Negative Control #1 were transfected to evaluate transfection efficiency and assess undesirable side effects through the transfection procedure. 6 h later, cells were supplemented with antibiotics-containing media and cultured for an additional 68 h. After 72 h, cells were collected for the mRNA and miRNA isolation.

2.2.1.3 MiRNA and mRNA Isolation.

MiRNAs were isolated to validate the overexpression of the miRNAs in the SUDHL-1 and Karpas 299 cells after miRNA transfection. First, total RNA was isolated using the RNeasy Mini Kit (Qiagen), including DNase treatment (Qiagen), according to the manufacturer's instructions (See section 2.1.1.7, table 8). The RNA concentration was subsequently measured using the Nanodrop 2000. mRNA was isolated from the ALK+ ALCL cell lines with and without miRNA overexpression to identify the target candidates by transcriptome analysis using next generations sequencing (NGS) or for the validation of the potential miRNA target genes by RT-qPCR. For further assurance, in primary cases, total RNA was extracted from FFPE tissues in primary cases using phenol/chloroform extraction, followed by DNase treatment (DNA-free™ Kit, Applied Biosystems), as described previously [165].

2.2.1.4 miRNA cDNA synthesis.

To quantify the mature miRNA and validate the miRNA overexpression in the ALK+ ALCL cells after transfection, cDNA was synthesized. The synthesis was performed from 100 nanograms of miRNA using the miScript II RT Kit (Qiagen), (Table 8), enabling a reverse transcription reaction using miScript HiSpec Buffer. Mature miRNAs were polyadenylated by poly(A) polymerase and transcribed to cDNA by reverse transcriptase; details are described in table 15.

Table 15. Reverse transcription of miRNA into cDNA using the miSript II RT Kit

Reagent	**Concentration**	**Volume (µl)**
miScript HSpec Buffer	5x	4
miScript Nucleics Mix	10x	2
Template miRNA	50 ng	2
ddH2O		11
Total Volume		20
Program Thermocycler		
Time	Temperature	
37°C	1h	
95°C	5 min	
4° C	∞	

2.2.1.5 miRNA relative quantification by RT-qPCR.

MiRNAs quantification was performed using miScript SYBR Green PCR Kit (Qiagen). SYBR Green is a fluorescence-emitting dye that binds to double-stranded DNA. During RT-qPCR, DNA is quantified in its log-linear phase of amplification by measurement of the amount of fluorescence that increases above the background. Relative quantification was performed comparing to normal expression in the cDNA from the ALK-positive ALCL cell line SUDHL-1. The following miScript Primer assays (Qiagen) were used: Hs_miR106b_1, Hs_miR-146a, Hs_miR-181-a_1_and Hs_miR-26a_2 (Qiagen), (Table 11). RT-qPCRs were carried out according to table 16 by duplicate, the Ct values were normalized to miR-106b, and expressions from the miRNA were calculated using the $2^{-\Delta\Delta ct}$ method.

Table 16. miRNA relative quantification by RT-qPCR.

Reagent	**Concentration**	**Volume (µl)**
miScript Universal Primer	10x	2
miScript Primmer assay	10x	2
Template cDNA	5 ng	2
QuantiTec Sybr Green PCR Master Mix	2x	10
ddH2O		4
Total Volume		20
Program Light Cycler 480 System		
Time	Temperature	Number of cycles
95°C	15 min	
95°C	15 seconds	
55° C	30 seconds	55 cycles
70° C	30 seconds	
55° C	Melting curve	

2.2.1.7 cDNA Synthesis.

MRNA from transfected cells was transcribed into cDNA. The cDNA synthesis was carried out with Superscript II reverse transcriptase (Qiagen), a mix of Oligo (dT) primer (Promega) and random hexamer (Thermo Fisher Scientific), according to the manufacturer's instructions (Table 17). The samples were diluted at 1:5 to obtain a concentration of 2.5 ng/µl.

Table 17. Annealing of primers to RNA

Reagent	**Concentration**	**Volume (µl)**
Random Primer	1 ng/µl	1
Oligo dT	500 ng/µl	1
Template mRNA	50 ng/µl	5
Program Thermocycler		
Temperature	Time	
70°C	2 min	
20°C	10 min	
cDNA synthesis using Superscript II Reverse Transcriptase		
Reagent	**Concentration**	**Volume (µl)**
First Strand Buffer	5x	4
DTT	0.1 M	2
dNTPs	10 mM	1
Superscriot II Reverse Transcriptase	200 U/µl	1
RNAse out	40 U/µl	1
ddH2O		4
Total Volume		20
Program Thermocycler		
Temperature	**Time**	
42°C	1 h	
95°C	5 min	

2.2.1.8 mRNA relative quantification by RT-qPCR to assess the efficiency of the transfection.

Relative mRNA expression to calculate transfection efficiency was analyzed using TaqMan assay. Quantification of *GAPDH,* the gene targeted by miRNA-mimic positive control, was performed in ALK+ ALCL cells with and without miRNA overexpression after cDNA synthesis.

Real-time quantitative RT-PCR analysis (RT-qPCR) was carried out by duplicates with the LightCycler 480 Probes Master using the LightCycler 480 System for detection (Roche Diagnostics). TaqMan assays detect the nuclease activity of the Taq polymerase by using oligonucleotides that have a donor fluorochrome (reporter, FAM) at one end and an acceptor fluorochrome (quencher, e.g., TAMARA) at the opposite end. Upon amplification of the target sequence, the

TaqMan probe is degraded by the 5`-3` exonuclease activity of Taq polymerase, separating the reporter and quencher, increasing the reporter fluorescence, which is detectable and will increase during the PCR cycles. This fluorescence is measured and allows conclusions about the amount of DNA produced. RT-qPCR was performed in duplicates, as shown in table 18. Normalization was performed with TBP (TATA-box binding protein). The data were analyzed using the 2-ΔΔCt method.

Table 18. RT-qPCR using Taq Man assay.

Reagent	**Concentration**	**Volume (µl)**
Assay (GAPDH or TBP)	10x	2
cDNA	2.5 ng/µl	4
Probes Master (Roche Diagnostics)	2x	10
Uracil-Glycolsylase	2 U/µl	0.2
ddH2O		3.8
Total Volume		20
Program Thermocycler		
Temperature	Time	
40°C	10 min	
95°C	10 min	
95°C	15 seconds	55 cycles
60° C	1 min	

2.2.1.10 Transcriptome analysis.

To identify the target genes of miR-146a, miR-181a, and miR-26a, a transcriptome analysis of SUDHL-1 cells, with and without miRNA overexpression, was performed. Transcriptome analysis using next-generation sequencing (NGS) was performed by CeGAT (Center for Genomics and Transcriptomics) in Tübingen, Germany. The RNA quality was tested with the Agilent 2100 bioanalyzer using the Agilent RNA 6000 Nano Kit, according to the manufacturer's instructions. Library Preparation: Small RNA sequencing libraries were constructed from 1 µg total RNA using the TruSeq Small RNA Library Prep Kit (Illumina, San Diego, CA), according to the manufacturer's instructions. Clusters were generated in a cBot instrument (Illumina) using "HiSeq® Rapid SR Cluster Kit v2" (Illumina), according to the manufacturer's instructions. Transcriptome sequencing was per-

formed using Illumina HiSeq2500 platform (1x50 Cycles). Data preprocessing: Illumina CASAVA (1.8.2) was used for demultiplexing the sequenced reads. The Adapter trimming was performed with Skewer (version 0.1.116). Trimmed raw reads were aligned to the human reference genome (hg19) using STAR (version 2.5.2b) [166]. Analyses of differential expression between groups were performed with DESeq2 [167] in R (R Core Team 2015). DESeq2 uses a negative binomial generalized linear model to test for differential expression based on gene counts. The quality of FASTQ files was analyzed with FastQC (version 0.11.5-CEGAT). Plots were created using ggplot2 (https://ggplot2.tidyverse.org) and dendextend package [168] in R (R Core Team 2015). The further processing of the data and the calculation of the expression strength were carried out with the Cufflinks Tool Suite (version 2.1.1). Cufflinks were also used to count mapped reads and to obtain the normalized gene expression of the gene in the sample. The normalized gene expression is expressed through the Fragments Kilobase of exon model per million mapped reads (FPKM) value. Data analysis was performed using the Jensen-Shannon-Divergence method to measure the similarity between two probability distributions. In this case, the gene expression profile was used as a basis for a hierarchical analysis clustering. Statistical analysis was performed to identify the significantly downregulated genes after miRNA overexpression (target genes). This analysis was the result of the comparison of the normalized gene expression (Fragments Kilobase of exon model per million mapped reads, FPKM value) between SUDHL-1 cells without miRNA overexpression and SUDHL-1 cells with miRNA overexpression.

2.2.1.11 Selection of the potential target genes.

Target genes were defined as those which were significantly downregulated after the miRNA overexpression of certain miRNAs in SUDHL-1 cells in comparison to untransfected or cells transfected with miR-negative control mimic. To distinguish the best candidate, target downregulated genes were sorted according to the normalized gene expression expressed through the FPKM value. From those genes, we selected as potential target genes only those genes with >500 FPKM value and with >0.4 differential expression given as a logarithm for the basis 2

(Log 2-Fold change) between the gene expression of the SUDHL-1 cells with and without miRNA overexpression, excluding genes with p-value adjusted by false discovery rate (FDR) >0.5. From those genes matching the selection criteria, we investigated which genes were predicted according to the following miRNA target gene prediction algorithms: MiRAnda, TargetScan, Target Scan S, Rna22, miR-Walk, and miRmap, a web tool that measures the strength of the prediction. We only selected the target genes predicted for at least one algorithm. Finally, we sorted the genes by p-adjusted value, reducing the number of false candidate genes subsequent from performing many tests. The functions of additional selected genes were investigated using the US National Library of Medicine National Institutes of Health (PubMed) database. Enrichment of manually ranking list was assessed using Gene Set Enrichment Analysis (GSEA, V4.1.0)[169,170] by the pre-ranked analysis option [169,170]. DESeq2 $\log_2$ fold change values between untransfected, and cells with mi-R146a overexpression were used to rank the genes. In addition, the REACTOME web data base was used for comparison [171,172].

2.2.2 MRNA relative quantification by RT-qPCR for target validation.

RT-qPCR of the target genes was performed in ALK+ (SUDHL-1, Karpas 299, KiJK, SR768, and SUPM2), ALK− (Fe-PD, Mac1, Mac2a) ALCL cell lines, mRNA from five patients with ALK+ ALCL and five patients with ALK- ALCL. The analysis was achieved using the UPL system.

Primers for genes selected as potential miRNA targets were designed according to the Universal Primer Library Technology platform (https://lifescience.roche.com/shop/en/global/overviews/brand/universal-probe-library.html); this comprises short hydrolysis probes substituted with blocked nucleic acids and enables the design of multiplex PCR to detect the gene target and reference gene expression. The probes were selected according to the manufacturer´s recommendations (Roche Diagnostics). *GAPDH* (glyceraldehyde-3-phosphate dehydrogenase), and *ACTB* (ß-actin) were used as housekeeping genes. RT-qPCR was performed in duplicates, as shown in table 19. Data were normalized with the corresponding housekeeping gene, reactions and permed by duplicates. mRNA expression was calculated with the $2^{-\Delta\Delta ct}$ method.

Table 19. RT-qPCR using UPL System.

Reagent	**Concentration**	**Volume (µl)**
Assay (*GAPDH* or *ACTB*)	10x	2
cDNA	2.5 ng/µl	4
Probes Master (ROCHE DIAGNOSTICS)	2x	10
Uracil-GLycolsylase	2 U/µl	0.2
ddH2O		3.8
Total Volume		20
Program Thermocycler		
Temperature	Time	
40°C	10 min	
95°C	10 min	
95°C	15 s	55 cycles
60° C	1 min	

2.2.3 Immunohistochemistry.

Tissue microarrays (TMAs) were assembled to test miR-26a and miR-181a targets using three patient samples from ALK+ and ALK− ALCL in duplicates. In addition, two samples from normal lymph nodes were added. 3-5 µm-thick sections were cut and stained with hematoxylin and eosin (H&E). Immunohistochemistry was performed on an automated immunostainer (Ventana Medical Systems, Inc.), according to the company's protocols. The TMAs were stained using the following antibodies (specifications listed in table 3): SLC2A3 (GLUT3) antibody (ab15311, Abcam) and CD93 antibody (HPA009300, Sigma-Aldrich). In addition, a larger cohort was used to test and validate the target gene of miR-146a. FFPE primary tumor samples of 81 ALK+ and 14 ALK-ALCLs patients were collected from the archives of the Institutes of Pathology from the University of Tübingen and the University of Kiel, Germany. Primary ALCL cases were completely immunophenotyped and classified in ALK+ and ALK- ALCL. CD147 immunohistochemistry (MEM-M6/1, Abcam) was performed and quantified using the histoscore as described below. The staining was scored according to the intensity and the cell percentage with membranous staining. The intensity was assessed as 0 negative, 1+ weak, 2+ moderate, and 3+ strong. Histoscore was then calculated by multiplying the intensity of the stains by the percentage of positively stained cells. Appropriate positive and negative controls were used to confirm the

adequacy of the staining. The use of human tissue samples was approved by the local ethics committee of the University of Tübingen (approval 620/2011BO2).

2.2.4 Direct regulation of miRNA and target gene analysis using Dual-Luciferase® Reporter Assay System.

To identify if there is a direct regulation between the miRNA and its validated target genes, a Dual-Luciferase Reporter Assay System Assay (DLR™, Promega) was performed. To evaluate the activity of miR-146a and confirm the direct regulation of its target genes, the miRNA binding site was first inserted downstream, or 3´, of the firefly luciferase gene (*luc2*) within the pmirGLO vector.

2.2.4.1 Cloning of the CD147 Insert into the pmirGLO vector.

2.2.4.1.1 Preparation of the insert from a PCR product.

The regions of the *CD147* 3´-UTRs, including the miR-146a binding site predicted by the miRanda tool, were amplified from DNA of human lymphocytes of a healthy donor as described in table 20 and cloned into the pmirGLO Dual-Luciferase miRNA target expression vector. Since the binding site of miR-146a in *CD147* was previously identified by Zhang *et al*., primers to amplify the insert were designed accordingly [112]. *SRPRB* is a direct target gene of miR-146a and was previously validated by Gersmann *et al*. in our group using DLR assay [111]. Therefore, the pmirGLO plasmid containing the *SRPRB* binding site was used as a positive control. The primers were manually designed with appropriate restriction sites (Sbf I and Sac I) to clone unidirectionally into the vector according to EMBL platform instructions (https://www.embl.de); primers are enlisted in table 11. The designed insert and digested vector were assembled using the free available blenching software (https://www.benchling.com/). After amplification, 3 µl of the product were electrophoretically separated in a 1% agarose gel at 140 V to validate the size of the product (475 bp). Purification of the insert was achieved using the PCR clean-up kit (Qiagen), and DNA concentration was measured by Nanodrop 2000.

Table 20. Cloning of the CD147 Insert.

Reagent	Concentration	Volume
H2O		17.1
PCR Buffer	10x	2.5
dNTP Mix*	10 mM	0.5
$MgCl_2$	25 mM	1.5
Forward primer	10 µM	0.6
Reverse primer	10 µM	0.6
AmpliTaq Gold DNA polymerase		0.20
DNA (50 ng/ µl)	2	2
Total volume	25	25

Themoycer Program	Temperature(°C)	Time	
Initial denaturation	95	10 min	
Denature	95	15 seconds	
Anneal	62	30 seconds	42 cycles
Extend	72	60 seconds	
Final extension	72	5 min	
Hold	4	Indefinitely	

2.2.4.1.2 DNA end modifications of the insert.

The restriction digestion of the insert after clean-up was carried out for 1.5 h at 37 °C. according to table 21. The purification of the insert was performed as previously described [165].

Table 21. DNA end modifications of the insert.

Reagent	Concentration	Volume
Sac I (Fast digest)	10 U/µl	1
Sbf I (Fast digest)	10 U/µl	1
Buffer Fast digest 10x	10x	2
Insert	71 ng/µl	16
Total volume		20
80 °C for 5 min to inactivate the enzymes		

2.2.4.1.3 Vector (pmirGLO) DNA end-modifications.

Digestion of pmirGLO Dual-Luciferase miRNA Target Expression Vector (Promega, Madison, Wi, USA) was carried out for 30 h at 37 °C, following 5 min at 80 °C to deactivate the enzyme activity, according to table 22. Subsequently, the restriction digestion product was electrophoretically separated in a 1.0% aga-

rose gel at 140 mV; the vector was isolated according to the phenol-chloroform method [111,165]. The linearized and purified vector concentration was measured on the Nanodrop 2000.

Table 22. Vector DNA end-modifications.

Reagent	**Concentration**	**Volume µl**
Sac I (Fast digest)	10 U/ µl	1
Sbf I (Fast digest)	10 U/ µl	1
Buffer Fast digest 10x	10x	2
Plasmid 2 µg (pmirGLO Promega)		10
Total volume		20

2.2.4.1.4 Dephosphorylation Roche Kit (Rapid DNA Dephos & Ligation Kit).

The vector was dephosphorylated using the Rapid DNA Dephos & Ligation Kit (Roche Diagnostics) using 1 µg Vector DNA, 2 µl rAPid Alkaline Phosphatase Buffer 10x, and 1 µl rAPid Alkaline Phosphatase. The samples were incubated in the thermocycler at 37 °C for 30 min and after at 75 °C for 2 min.

2.2.4.1.5 Vector quantification and ligation reaction.

The PCR products were inserted into the pmirGLO Dual-Luciferase miRNA target expression vector (Promega) by using the Rapid DNA Dephos & Ligation Kit (Merck KGaA) using two ratios (50:150 and 100:100), according to the manufacturer's instructions (Table 23).

Table 23. DNA concentration of vector by nanodrop after dephosphorylation.

	Concentration	**(50 ng vector**	**(100ng vector:**
pmirGLO	45.8 ng/µl	1.09 µl	2.18 µl
Insert	32.4 ng/ µl	4.62 µl	3.08 µl
Dilution Buffer	5x	2 µl	2 µl
H2O	To 10 µl	2.29	2.74
		Mix well	
T4 DNA Ligation Buffer	2x	10 µl	10 µl
T4 DNA Ligase	1 U/µl	1 µl	1 µl
	30 min Room Temperature (Ligase step 1) Thermocycler		

2.2.4.1.6 Transformation.

Transformation was carried out using 5 µl of the ligation product in 50 µl of competent Top 10 *E. Coli* on ice in 1.5 ml Eppendorf tubes. After 30 min of incubation, heat shock was performed by placing the samples at 42 °C for 30 seconds. 250 µl of pre-warmed S.O.C. medium was added, and the samples were incubated for 2 h at 37 °C in a thermoshaker at 225 rpm. Next, 100 µl of the product was spread on LB-Agar plates and incubated overnight at 37 °C.

2.2.4.1.7 Screening of the cloning by PCR-Colonies.

A PCR using sequencing primers was performed to assess the efficiency of insert cloning. The forward primer (pmirGLO_F: TGACCGGCAAGTTGGACGCC) was placed 132 bp upstream of the *SacI* interface, and the reverse primer pmirGLO_R (GGCCGCCCAAGGGGTTATG) was placed 95 bp downstream of the interface, yielding a product size of 227 bp for one vector relation. If the insert was installed correctly, the product size was extended by the size of the insert, in this case, 475 bp (Table 24).

Table 24. Screening of the cloning PCR colonies.

Reagent	**Volume (µl) (5x)**		
H2O	18.6	93	
10x PCR Buffer	2.5	12.5	
10 mM dNTP Mix*	0.5	2.5	
25 mM $MgCl_2$	2	10	
10 µM Forward primer	0.6	3	
10 µM Reverse primer	0.6	3	
AmpliTaq Gold DNA polymerase	0.20	1	
Colony			
Program	**Temperature(°C)**	**Time**	
Initial denaturation	95	10 min	
Denature	95	15 seconds	38 cycles
Anneal	62	30 seconds	
Extend	72	60 seconds	
Final extension	72	5 min	
Hold	4	Indefinitely	

The PCR samples were electrophoretically separated in a 1.5% agarose gel at 140 mV. Compared with the non-linearized vector as a control, the base pair lengths of the PCR products provided an early indication of whether cloning was

successful. One successful cloned vector was selected for future experiments. Midi-preps from a selected plasmid were performed according to manufacturer's protocol (Promega), and the quantification of the isolated plasmid was done using Nanodrop 2000. The selected vector was verified using Sanger sequencing.

2.2.4.2 Transfection of HEK293T and He-LA cells with miRNA-Mimics and luciferase reporter assay.

The Dual Luciferase® Reporter Assay System from Promega is based on the measurement of *firefly* luciferase (*luc2)* and *renilla* luciferase (*hRluc-neo*) activity. In this system, firefly luciferase is the primary reporter gene; reduced firefly luciferase expression indicates the binding of endogenous or introduced miRNAs to the cloned miRNA target sequence. After lysis of the cells, this can be detected with a luminometer. Analysis was performed after 20 h incubation at 37 °C and 5% CO^2 and lysis of the cells. For luciferase reporter assay, HEK-293 and HeLa cells were conserved in cell culture and microscopically controlled every day for seven days before transfection. $4x10^5$ HEK-293 and HeLa cells per well were seeded in 12 -well plates and incubated for 20 h at 37 °C and 5% CO^2 before transfection. Cells were transfected using 2 µg pmirGLO Dual-Luciferase miRNA Target Expression Vector, and 16 µl miRIDIAN miRNA mimics (has-miR-146a-5p) (Dharmacon) with 6 µl Lipofectamine 2000 (Invitrogen) diluted in 100 µl optimum (Thermos Fisher Scientific), as described in table 25. After transfection of the complexes, cells were incubated for 6 h at 37 °C and 5% CO^2, and then 120 µl RPMI containing 10% FCS was added. 40 h following transfection, cells were counted and split in triplicates $3x10^4$ cells/well in 180 µl DMEM with 10% FCS and 1% P/S in a 96-well.

Analysis was completed after 20 h incubation. The growth medium from cultured cells was removed, and cells were rinsed with 180 µl PBS. The cell lysis was achieved using 20 µl of 1x Passive Lysis Buffer and 15 min incubation on a rocker.

Table 25. pmirGLO transfection complexes and conditions

ID	Description	Concentra-tion	Vector (µl)	miR-146a mimic (µl)	Optimem (µl)
1	Neg control Optimem				100
2	Optimem + Lipofectamine				100
3	pmirGLO	307.5 ng/µl	6.5		100
4	miR-146a mimic			16	100
5	pmirGLO + miR-146a mimic		6.5	16	100
6	pmirGLO-CD147	312 ng/µl	6.4		100
7	pmirGLO- CD147 + miR-146a mimic		6.4	16	100
8	pmirGLO SRPRB	323.1 ng/µl	6.19		100
9	pmirGLO SRPRB + miR-146a mimic		6.19	16	100

The luciferase and *renilla* activity pipetting and the measurement was performed with the TriStar LB941 (Berthold Technologies) with the specified assay. In this program, 100 µl Luciferase Assay Reagent was first added to the cell lysates; this contains Beetle luciferin, the substrate of *firefly luciferase*. Subsequently, the luminescence was measured. In a subsequent step, 100 µl Stop and Glo Reagent was added, containing Coelenterazine, *renilla* luciferase substrate, and a firefly luciferase suppressing substance. The light emission was then measured again. For each sample, two luminescence measurements were obtained (*luciferase* and *renilla*) by triplicate. To normalize the measured values, background luminescence activity was removed, and the *firefly luciferase* measurement of each sample was divided by its corresponding *renilla* luciferase measurement.

2.2.5 Analysis of ALK dependence of CD147 and miR-146a.

Crizotinib (PF-02341066) was synthesized and purchased at Med Chem Express. Stock solutions were prepared in DMSO solution and diluted in PBS to reach 25, 50, and 100 nM concentrations. ALK+ALCL cell lines (Karpas 299 and SUDHL-1) with $2x10^5$ density were incubated in T25 flask at 37 °C in the presence of the increasing concentrations of Crizotinib by triplicates (0, 25, 50, and 100

nM) during 48 and 72 h. The medium was replaced every 24 h, and fresh medium with antibiotic (P/S) and corresponding Crizotinib concentration was given. After 48 and 72 h of treatment, cell pellets were retrieved, protein and total miRNA were isolated. ALK inhibition was confirmed and the expression levels of CD147 were assessed by WB (described in section 2.2.6.3.3). Subsequent miR-146a expression was estimated by RT-qPCR as described before in section 2.2.2.

2.2.6 CRISPR/Cas-9 Knockout (KO) and shRNA knockdown (KD) of the potential candidate genes to assess their function and relevance in ALK+ ALCL.

2.2.6.1 CRISPR/Cas-9 system.

Clustered Regularly Interspaced Short Palindromic Repeat (CRISPR) associated protein (Cas) is a method employed to KO target genes, contributing to understanding the gene's function. The system has two components: a guide RNA (gRNA) and a CRISPR vector containing the Cas9 protein. The gRNA is a short synthetic sequence containing the scaffold sequence for the Cas9 protein binding and a sequence of approximately 20 nucleotides, which is unique compared to the rest of the genome and delimits the gene to be targeted. Adjacent to the sgRNA, a Protospacer Adjacent Motif (PAM) acting as a Cas9 binding signal, is found. On the other hand, Cas9 is an RNA-guided endonuclease from *Streptococcus pyogenes* (SpCas9), which uses base pairing to recognize and cleave target DNAs with complementarity to the guide RNA. SpCas9 uses a Protospacer Adjacent Motif (PAM), which is adjacent to the sgRNA and serves as the Cas9 binding signal. Cas9 forms a nucleoprotein complex with the sgRNA, activating and changing its conformation, allowing it to bind to the DNA. The Cas9-gRNA complex then goes through a second conformational change resulting in the interaction of its catalytic domains, the modular RuvC-like domain, and the C-terminal HNH-like domain. Each domain cleaves one of the DNA strands, resulting in a blunt-ended double-strand break (DSB) 3 bp upstream of the PAM motif within the target DNA. The resulting DSB is then repaired by one of two general repair processes, including the non-homologous end joining (NHEJ) repair process and the homology-directed repair (HDR) pathway, which results in the intro-

duction of indels resulting in amino acid deletions, insertions, or frameshift mutations, producing non-sense-mediated decay (NMD) of the mRNA transcript or leads to non-functional proteins. Individual lentiviral CRISPR plasmids targeting a single genomic locus targeting *CD147, GLUT3*, and *CD93* were designed and constructed according to the lentiCRISPRv2 (Addgene), one vector system protocol [173,174]. This vector contains two expression cassettes, hSpCas9 and single guide RNA skeleton.

2.2.6.1.1 SgRNA design.

The sgRNAs oligonucleotides were designed using the GUIDES design tool (Sanjana Lab, New York Genome Center, table 11). The seed sequence was flanked on the 3' end by a 3 bp NGG PAM sequence. Standard de-salted oligos were diluted to 100 µM in sterile water.

2.2.6.1.2 SgRNA shRNA cloning into then lentiCRISPRv2 backbone.

2.2.6.1.2.1 Lentiviral vector digestion.

Digestion of LentiCRISPRv2 plasmid (5 µg, Addgene) was performed using *BsmBI (Esp3I)* fast digest enzyme for 30 min in the heating plate at 37 °C (Table 26).

Table 26. LentiCRISPRv2 plasmid digestion.

Component	Concentration	Volume (µl)
LentiCRISPRv2 plasmid	1 µg	5
Fast Digest *BsmBI*		3
FastAP Thermosensitive Alkaline Phosphatase	1 U/µl	3
Fast Digest Buffer	10x	6
DTT (freshly prepared)	100 mM	0.6
Nuclease-free water		43
Total		**60**

The product was electrophoretically separated in an 0.8% agarose gel diluted in 50 ml 1x TAE Buffer (Tris-acetate-EDTA) buffer containing 1:1000 of Ethidium Bromide and using 10 µl of the 100 bp DNA ladder (Thermofisher Scientific). The gel ran at 80 Volts for 90 min. Next, the larger band was selected for subsequent analysis, whereas the ~2 kb filler piece was discharged. The digested plasmid

was purified using QIAquick Gel Extraction Kit (Qiagen) and eluted in elution buffer supplemented by the kit. Finally, the digested plasmid was stored at -20 °C.

2.2.6.1.2.2 Oligo annealing.

Previously designed pairs of shRNA were phosphorylated and annealed according to the table 27.

Table 27. Oligonuleotides phosphorylation and annealing.

Component	Final concentration	Volume (µl)
Forward sgRNA (100 µM)	10 µM	1
Reverse sgRNA (100 µM	10 µM	1
T4 Ligation Buffer, 10x (NEB, cat. no.: B0202S)	1x	1
T4 PNK (NEB, cat. no.: M0201S)/ enzyme		0.5
Nuclease-free water		6.5
Total		10
Program Thermocycler	**Temperature**	**Time**
Denature	37 °C	30 min
Anneal	95 °C	5 min
Extend	Ramp down 25 °C, at 5 °C/min	~50 min

2.2.6.1.2.3 Cloning into digested LentiCRISPRv2 plasmid.

After phosphorylation and annealing, the oligonucleotides were diluted 1:200 with nuclease-free water and transferred to a 1.5 ml tube. Annealed oligos were stored at -20 °C. Subsequently, a ligation reaction was performed according to table 28 and incubated for 10 min at room temperature. The transformation was performed into 50 µl One shot Stbl3 bacteria (Invitrogen C7373-03) in LB-plate and LB broth supplemented with 100 µg/ml ampicillin. First, the cells were thawed on ice, then 5 µl of the DNA were added, and the sample was mixed very gently. The samples were incubated for 30 min on ice. Next, the cells underwent heat shock for 45 seconds at 42 °C without shaking and then incubated on ice for 2 min. After incubation, 250 µl of pre-warmed S.O.C. Medium (37 °C) was added to each sample, and samples were incubated in a shaking plate at 37 °C for 1 h at 225 rpm. All the transformation volume was spread on a pre-warmed selective

plate and incubated overnight at 37 °C. After 16 h incubation time, inoculation in liquid bacterial culture with selected colonies was performed using 3 ml liquid LB to a flask with ampicillin (100 µg/ml). Subsequent incubation of bacterial culture at 37 °C overnight followed. Centrifugation of the samples was performed, and the liquid was discharged. The plasmid DNA purification was performed using the QIAprep Spin Miniprep Kit (Qiagen) and a Microcentrifuge. Afterward, samples were measured with nanodrop. The plasmid was analyzed by Sanger sequencing using primer hU6-F (5'-GAGGGCCTATTTCCCATGATT-3').

Table 28. Ligation reaction.

Component	Concentration	Volume [µl]
BsmB1 digested plasmid	50 ng	0.8
Diluted annealed oligonucleotides	dilution (1:200)	1
Quick Ligase Buffer (NEB)	2x	5
Nuclease-free water		3.2
Subtotal	10	10
Quick Ligase Buffer (NEB)		1
Total	11	11

2.2.6.1.3 Packaging CRISPR constructs into lentiviral particles.

To produce lentivirus, the plasmid was co-transfected with the transfer vector viral packaging (psPAX2, AddGene 12260): viral envelope (pMD2G Add Gene12259) into HEK293T cells. 4x105 HEK293T cells were seeded per well in 6 well plates in a total volume of 1.6 ml. Transfection was performed according to table 29. First, the sgRNA-CRISPR packaging plus mix was incubated for 15 min at room temperature. Subsequently, 200 µl of lipofectamine mix were added and mixed gently by pipetting up and down. Incubation for 15 min was followed at room temperature. Finally, the complexes were carefully given to the cells (400 µl per well). After 12 to 18 h of incubation, the transfection medium was removed, and 2 ml of DMEM medium supplemented with 10% FCS and 1% PS was added. After 24 h incubation, cells were centrifugated for 5 min at 1000 g. Viral supernatant was filtered through a 0.44 µm filter, and aliquots were stored at -80 °C.

Table 29. Packaging of LentiCRISPRv2 plasmid mixes.

Reagent	Concentration	Per replicate (µl)
Packaging-Plus mix		
OPTI-MEM		190
PACKAGING MIX psPAX2: pMD2.G 2:1 (500 ng/ul)	820 ng	2.5
	410 ng	12.75
Plus Reagent		2.5
sgRNA-CRISPR	50 ng	5
To each replicate, 195 µl of packaging mix		
Lipofectamine-mix		
OPTI-MEM		197
Lipofectamine LTX (Invitrogen)		3.7
		18.87
To each replicate, 200 µl of packaging mix		

2.2.6.1.2.4 Transduction in ALK+ ALCL cells.

ALK+ ALCL cell lines (SUDHL-1 and KiJK) were cultured one week before the infection and split in case of confluency. On the day of transduction, $5x10^5$ ALK+ ALCL cells per well (SUDHL-1 and Karpas 299) were seeded in 12-wells plate, resuspended in 1.6 ml of RPMI medium containing 8 µg/ml polybrene. The virus was carefully given 0.8 ml per well. Centrifugation was followed at 2500 RPM for 1.5 h at 30°C. Cells were incubated after 72 h antibiotic selection with RPMI medium containing puromycin antibiotic (1 µg/ml). After an extra 72 h of incubation, the antibiotic medium was discharged, and cells were supplemented with 2 ml of fresh RPMI medium with 10% FCS and 1% PS. Cells were counted using a hemocytometer and 4000 cells/per in the well A1 of a 96-well plate. Limiting dilution was performed for each condition. Cells were incubated for two weeks, and once a cell pellet was visible, the clones were selected and subsequently seeded in a 6-wells plate. When the concentration of the cells was enough, the cells were seeded in T25 flask. Once the concentration of $3x10^5$ cells per cm^2 was reached, cell pellets for protein extraction were collected, and the rest of the cells were stored for subsequent experiments.

2.2.6.2 shRNA knockdown.

The shRNA-induced KD represents an additional method to study gene functions through gene silencing using the endogenous RNA interference (RNAi) system

[175,176]. The RNAi system is an endogenous mechanism from mammalians for transcriptional gene-specific degradation of host mRNA through the cytoplasmic delivery of double-stranded RNA (dsRNA) identical to the target sequence. The degradation of target gene expression is achieved by an enzymatic pathway involving the RNA-induced silencing complex (RISC), which recognizes one strand of the dsRNA and processes it with the assistance of the Argonaute (Ago) proteins and double-stranded RNA-binding proteins. The complementary mRNA is identified and cleaved by Ago. The cleaved mRNA is further degraded by other endogenous nucleases [177]. This technology silences genes by replacing the endogenously occurring dsRNA with artificially synthesized si- or shRNAs.

Five different synthetic shRNAs to CD147-KD were designed by our group (BLOCK-iT™ RNAi Designer (Thermo Fisher Scientific) online tool) or taken from the literature as homologous to the cDNA of the target gene [173,174]. The CD147 and MCT1 shRNA sequences are enlisted in table 30.

Table 30. ShRNA oligonucleotides.

CD147 shRNA	Primer 5′ to 3′
A	AGCTTTTCCAAAAAGTCGTCAGAACACATCAACTCTCTTGAAGTTGATGTGTTCTGACGACGGG
B	TGACAAAGGCAAGAACGTCTCTCTTGAAGACGTTCTTGCCTTTGTCA
C	AGCTTTTCCAAAAAGGTTCTTCGTGAGTTCCTCTCTCTTGAAGAGGAACTCACGAAGAACCGGG
D	AGCTTTTCCAAAAAGCTACACATTGAGAACCTGAATCTCTTGAATTCAGGTTCTCAATGTGTAGCGGG
E	GCTTTTCCAAAAAGGCTGTGAAGTCGTCAGAACATCTCTTGAATGTTCTGACGACTTCACAGCCGGG

The oligonucleotides were cloned in the pSuper vector, which contains the RNA polymerase II promoter. The H-1 promoter (RNA polymerase II) and shRNA were cloned subsequently in the pFUGW transfer vector carrying the Green Fluorescent Protein *(*GFP) reporter gene to confirm the transfection rate as previously described [111 178]. The shRNA efficiency was assessed in He-LA cells. Due to the high efficiency of the vector carrying the *CD147* A and B sequences, they were selected for further investigation.

2.2.6.2.1 Lentiviral production in HEK293T cells.

Lentiviral-mediated transduction was elected since it provides a convenient method of introducing shRNA into dividing or non-dividing cells, especially in hard-to-transfect lymphoid cells and, in general, is less toxic to the cells than adenoviral-mediated transduction. HEK293T cells were seeded 7 days before virus production and split in case of confluency. On the day prior to virus production, the cell cultures were combined into one cell culture flask, and cells were counted. $6*10^6$ cells were seeded per Petri tissue culture plate diluted in DMEM 10% FCS 1% P/S. A total of ten tissue culture plates were seeded for each transfer plasmid: an empty pFUGW plasmid (pF-S) and a pFUGW plasmid with a scrambled insert (Heat shock protein homolog, pF-SS1) and pFUGW plasmid with CD147 shRNA A (p-F-CD147A). Cells were incubated for 20 h, allowing the cells to form a cell lawn. One-hour before transfection, the antibiotic medium was removed and replaced with 5 ml DMEM medium without penicillin/streptomycin with 10% FCS.

All further experiments were performed in a biosafety level 2 laboratory. For transfection, a transfection master mix (mix-1) was prepared and incubated for five min at room temperature. This mix-1 contained the transfection reagent lipofectamine 2000 dissolved in OptiMEM medium (20 µl of Lipofectamine 2000 in 500 µl of OptiMEM medium per Petri plate. In a subsequent step (mix-2), transfection vector mixes were prepared and dissolved in 500 µl of OptiMEM containing: 5 µg of the VSVG envelope plasmid, 7 µg of the packaging vector pCMVDR8.9 and the pFUGW transfer corresponding vector according to condition. Each transfection batch was mixed and placed in a 50 ml tube. Mix-2 was mixed with 5 ml per batch and incubated for 20 min at room temperature. Then, 1 ml of the final transfection mixtures were gently dropped on their respective plates. After 6 h incubation, the medium was removed and replaced with 7 ml of DMEM 10% FCS 1% P/S medium with addition of pyruvate. The cells were incubated under standard conditions for 48 h until virus collection. Cells were assessed under the fluorescence microscope since the GFP expression will be present in successfully transfected cells. The supernatant from each condition was collected in a 50 ml reaction falcon tube and centrifuged at 2000 rpm at room temperature for 5 min. To remove all cell debris, the supernatant was filtered at 0.45 µm (Stericup Millipore

SCHVU01RE). To concentrate the virus, the supernatant was filtered on (Avantor, Vivaspin® 20) by a centrifugation for 3 h at 3000 rpm. Finally, the virus was collected in 1.5 ml Eppendorf tubes and in aliquots of 50, 100, and 200 µl and stored at -80 °C.

2.2.6.2.2 Virus infection in ALK+ cell lines (SUDHL1 and KiJK).

ALK+ ALCL cell lines (SUDHL-1 and KiJK) were cultured one week before the infection and split in case of confluency. On the day of infection, of $2*10^6$ cells in 500 µl RPMI 10% FCS 1% P/S containing (8 µg of polybrene/ml) were seeded in a 12-well plate. Each condition was seeded in triplicate.

The infection medium was prepared with 25 µl virus (pF-S, pF-SS1-e, pF-CD147A, pF-CD147B and pF-CD147D) in 475 µl RPMI 10% FCS 1% P/S containing (8 µg of polybrene/ml). The virus suspension was gently dropped in the corresponding well. After this step, the 12-well plates were centrifuged for 1.5 h at 800 g (2224 rpm approx.) at 37 °C followed by 4 h incubation, at 37 °C and 5% CO^2, to direct the cells to the bottom of the well. Medium was removed and cells were resuspended in 5 ml RPMI 10% FCS and 1% P/S and transferred to T25 cell flasks and further incubated at same conditions for 72 h. During this time the cells were supplemented with medium according to its density. After incubation, infection rate was assessed by Flow Cytometry (FACS) analysis. A second infection was performed after incubation time, following the same procedure as described for the first infection. After second infection, FACS analysis was accomplished again to confirm the infection rate.

2.2.6.2.3 Efficiency analysis by FACS.

For FACS analysis, 1.5 ml cells suspension were centrifuged (800 rpm, 5 min) and resuspended in 1 ml FACS buffer. This buffer contained 1% propidium iodide (PI) to label the dead cells. During the FACS analysis, PI and GFP are excited by lasers with suitable wavelengths and the resulting fluorescence signal is assessed according to the percentage of infected cells (fraction of cells positive for GFP) and dead cells by percentage of cells staining for PI. The FACS measure-

ment was carried out according to the manufacturer's standard protocol and the software FlowJo™ v10.7 was used for the assessment.

2.2.6.3 Confirmation of the KO or KD using NGS analysis and WB.

To elucidate the effect of the most relevant miRNAs target genes (CD147, GLUT3, and CD93) in ALK+ ALCL cell lines (SUDHL1, KiJK and Karpas 299), these genes were silenced using shRNA KD and/or CRISPR/Cas9 system KO.

2.2.6.3.1 Bradford assay for protein quantification.

The protein concentration was determined using the BCA (bicinchoninic acid assay) protein assay reagent (Thermo Fisher Scientific). The BCA protein assay is a colorimetric method used for protein quantification which consist in two reactions. In the first reaction, also known as the biuretic reaction, Cu2+ ions are reduced to Cu+ cations by peptides. The amount of Cu+ cation reduced is proportional to the amount of protein present in the solution. In the second reaction, two molecules of bicinchoninic acid complex with a reduced Cu+ cation producing a strongly purple colored reaction product. The BCA-copper complex shows a strong linear increase in absorbance at 562 nm with increasing protein concentrations. The amount of protein present in the solution was calculated using a standard curve. BSA (Bovine Serum Albumin, 1 mg/ml) was used as a standard, diluted with T-Per buffer (Thermo Fisher Scientific) to generate a standard curve with concentrations of 0, 50, 100, 200, 400, 600, and 800 ng/µl. The protein solutions were diluted (1:10). To prepare the working solution the reagents A and B were mixed in a ratio of 51:1. From this mixture, 1 ml was given to each of the different samples. The samples were mixed, incubated at 60 °C for 15 min, and then transferred by duplicate 300 µl each to transparent 96-well plates to measure four absorbance values from each sample. Absorbance was measured using the iMark Microplate Absorbance Reader (Biocompare). Protein concentrations were determined from the absorbance values minus the blank values using the standard straight line.

2.2.6.3.2 Western Blot.

For the Western Blot (WB), the proteins were separated by SDS-PAGE (sodium dodecyl sulphate- polyacrylamide gel electrophoresis). SDS-PAGE is a system for separating proteins according to their molecular weight, on the basis of their different migration rates through a gel under the influence of an applied electric field. By using SDS and polyacrylamide gel the influence of the structure and charge of the proteins is eliminated, and the proteins are separated solely based on polypeptide chain length. In this system, the anionic SDS detergent, present in the running buffer denatures and binds to the proteins to make them uniformly charged to balance the chamber flow rate and allow them to separate according to their protein size. The PAGE is cast as a separating gel topped by stacking gel with high porosity buffer at 6.8 whereas the separating gel contains high percentage of acrylamide and is cast in Tris-Cl buffer pH 8.8. Proteins-SDS move through the gel and are separated through a sieving effect.

To prepare the samples for the electrophoretic separation, volume of samples was calculated for 30 µg of a total protein mixture diluted with T-per buffer. The correct volume of protein was supplemented 2x Laemmli buffer to stain the proteins (2:1 ratio). This buffer contains 2 beta-mercaptoethanol (3:1 ratio), which is necessary to denature the proteins. The protein mix samples were denatured for 5 min at 95 °C in a shaking heating block. After denaturation, the samples were briefly cooled on ice and centrifuged. Criterion XT Bis-Tris gels 4-12% (Bio-Rad) of 12 or 18 wells were used depending on the number of samples. Gels were placed in the Criterion (Bio-Rad) gel chambers. Pockets were rinsed (1x XT-MES) and chamber was filled with running buffer (1x XT-MES). Samples and a protein size marker (Precision Plus Protein, Western C, Bio-Rad) were loaded and chamber was locked. Electrodes were connected to power supply (power Patmc 300, Bio-Rad). Total running time depended on the protein size and marker, approximately 15 min at 135 V, followed by 120 min at 145 V. During the procedure, the running chamber was in ice bath to regulate the temperature. After separation, the gel cast was dismantled. Proteins were transferred from the gels to nitrocellulose membranes, which were previously cut and rinsed in autoclaved distilled water and then in transfer buffer. For transfer the gel and membrane were

arranged in “sandwich” manner. This "sandwich" was placed between the transfer plates and clamped tightly to avoid air bubbles. The whole was dangled in the blot chamber filled with transfer buffer. Chamber was locked and connected to the power supply. Transfer took 2.5 h with the following parameters: 2 h at 330 mA and 30 min at 250 mA. The chamber temperature was also controlled by cooling elements and ice bath. After transfer, membranes were stained with Ponceau-S solution to control the transfer efficiency. Subsequently, the membrane was rinsed with ddH2O in several washing steps until no more staining was visible. To prevent protein contamination, the remaining binding sites of the membrane were blocked using 5% skim milk/1x TBS-T solution in a shaking water bath at 37 °C for one hour. After blocking, membranes were washed with 1x TBS-T in two rapid washing steps, followed by a 15 min and 5 min washing steps on the shaker. Membranes were incubated with the corresponding specific primary antibody (Table 2.1.1.1), overnight at 4 °C on a shaker. Membranes were washed again in 1x TBS-T with two rapid washing steps, followed by one 15-minuteminand two 5 min washing steps on the shaker. The secondary antibody was given according to the specie of the first antibody (Table 2.1.1.1). Most of the antibodies were diluted in 5% skim milk/TBS-T solution. Only in case of sensibility to phosphatase activity, 3% BSA / TBS-T solution was used. In addition, 0,4 ul of Precision protein TM Strep Tactin-horseradish peroxidase (HRP, Bio-Rad) for every 10 ml antibody dilution was supplemented for the colorimetric detection. 2 more 15 min washing steps were done.

Development was made by enhance chemiluminescent (ECL) and detected by x-ray film or by using LI-COR imaging systems. ECL is based on the production of the light through the interaction of the HRP labeled antibody and its substrate. For detection, two substrates were used according to the level of sensitivity required: Super Signal TM West Femto Maximum Sensitive Substrate and Super Signal TM West Pico PLUS Chemiluminiscent Substrate (Thermo Fisher Scientific). Membranes were incubated with the substrate for 5 min in the dark and placed in the X-ray film cassettes. In the dark room, x-ray films (Typon Contatyp CX-BL, Hasternstein) were exposed to the membranes from 1 to 90 min. Finally,

x-ray films were then developed in the Curix 60 development machine (AFGA CP1000).

WB digital imaging was performed using the LICOR technology in the Odyssey XF imager. This technology has two modes, near-infrared fluorescence (NIF) and chemiluminescence, allowing to perform either quantitative WB or chemiluminescent WB. To identify the fluorescent signal, an immunofluorescence secondary antibody was used. Protein quantification was performed by measuring the optical density of the WB bands by using the Image Studio Lite software (Version 5.2).

2.2.6.3.3. NGS analysis using fusion method.

To validate the CD147-KO, pathogenic mutations leading to CD147 protein inactivation were investigated using targeted NGS analysis. 25 ng DNA of CD147-KO cell clones were sequenced on the Ion S5™ System (Thermo Fisher Scientific, South San Francisco, CA, USA). Mutations were studied using the bidirectional sequencing using the fusion method (Thermo Fisher Scientific, Thermo Fisher Scientific), according to manufactures' protocol. This method allows the overamplification of short amplicons (<150 bp) by PCR, using two fusion primers to attach the amplicons to the adapters, Ion A and truncated P1 (trP1). Design of the primers was carried out with the freely available online program Primer3web (version 4.0.0). The primers forward (5' GGTTCCAGGCTCCTCTCTC 3') and reverse (3' CTCCTTGGCTTCTCACCTTG 5') were used in order to amplify the *CD147* region of interest near to the PAM region in a standard PCR. The subsequent workflow was made according to manufactures' protocol: purification of the amplicon libraries targets using beads, preparation of the equimolar concentration and dilution of the pool of the amplicon library. The templates were sequenced and the sequence reads of the samples were analyzed in the freely available program Integrative Genomics Viewer (IGV, Broad Institute) [156].

2.2.7 Comprehensive analysis of CD147-KD and KO *in vitro* and *in vivo*.

2.2.7.1 Cell analysis in vitro.

2.2.7.1.1 Cell Proliferation and Viability Assay (CellTiter 96® AQueous One Solution Cell Proliferation Assay).

Cell viability and growth retardation were assessed using CellTiter 96® AQueous One Solution Cell Proliferation Assay (Promega) in SUDHL-1 and KiJK cells with and without CD147-KD [42]. This assay is a colorimetric method used to assess cell proliferation, viability, and cytotoxicity using two compounds: MTS and phenazine ethosulfate (PES), an electron coupling reagent that builds a stable solution. The MTS compound is named after its inner salt [3-(4,5-dimethylthiazol-2-yl)-5-(3-carboxymethoxyphenyl)-2-(4-sulfophenyl)-2H-tetrazolium. During the assay, the MTS component is reduced by the cells into a colored formazan dye soluble in the cell culture medium. The number of living cells is directly proportional to the quantity of formazan dyze measured at 490 nm absorbance in a plate reader. KiJK and SUDHL-1 cells with and without CD147-KD or CD147-KO to achieve a cell density of $3x10^5$ /cm^2 in 4 ml RPMI medium supplemented with 10% FBS and 1% P/S in T25 cell culture flasks per triplicate. For CD147-KD and controls (SUDHL-1 and KiJK cells), the assay was performed 72 h after the second infection. In the case of SUDHL-1 CD147-KO cells and controls, the assay was performed when single clones reached a density of $3x10^5$/cm^2. The assay was implemented every 24 h from day zero. Every cell suspension was correctly mixed. 100 µl of cell suspension was pipet in 96-Well Black/Clear Bottom Plates (Thermo Fisher Scientific) by triplicates. 10 µl of MTT solution (Promega) was added, and plates were incubated for 2 h at 37 °C and 5% CO^2 in the dark. After incubation, samples were measured at 490 nm absorbance using the iMARK iMark™ Microplate Absorbance Reader (Bio-Rad).

2.2.7.1.2 Cell cycle and cell apoptosis analysis.

The distribution of cells at specific cell cycle stages was evaluated using flow cytometry (FACS Calibur), as described previously by Nuesse *et al*., 1994 [179]. This analysis comprises two different treatments of the cells. The first comprises a salt solution containing a detergent, followed by additional treatment with a second solution containing citric acid and sucrose (Table 32). This two-step treatment destroys the cellular membrane and the cytoplasm, and nuclei and micro-

nuclei are released in suspension. In this experiment, SUDHL-1 cells with CD147-KD and controls at a density of $5x10^5$ were centrifuged and disposed in FACS tubes. 500 µl of the first solution containing propidium iodide (PI) (ratio 1:40) was given, cells were resuspended and incubated for 1 hour in the dark. After incubation, 500 µl of the second solution was given, cells were resuspended, and incubated at 4 °C until FACS measurement. The samples were analyzed for cell cycle distribution using ModFit LT, version 4.0 (Verity Software House, Inc.,).

Table 31. Solutions for the cell cycle analysis.

First solution	(For 500 ml volume)
NaCl	292 mg
Tri-Na-Citrate	500 mg
RNAse A (50 mg/ml)	5 mg
Nonidet P-40	150 µl
PI-Solution (1 mg/ml)	1:40 (add before using)
Second solution	(For 500 ml volume)
Citronensäure-Monohydrat	7.5 g
Sucrose (0.25 M)	85.57 g
Sterile filtration	

Apoptosis analysis was performed by using annexin V (AnnexinV-APC, Invitrogen) and PI (Sigma-Aldrich) staining following the manufacturer protocols and assessed by flow cytometry (FACS Calibur, BD).

For the staining, SUDHL-1 cells with CD147-KD and controls were disposed in FACS tubes with a $3x10^5$ cellular density and centrifuged at 1200 rpm for 5 min. Cells were resuspended with 200 µl of Annexin-Buffer (Table 32) and then centrifuged for additional 5 min. Next, cells were resuspended again in 100 µl Annexin-Buffer and incubated for 15 min at room temperature in a dark room. After incubation, 400 µl Annexin-Buffer were added, and cells were incubated at 4 °C until measurement by FACS. FACS data were analyzed in the FlowJo™ V9.9.6 Software (BD Life Sciences).

Table 32. Annexin Buffer

Annexin Buffer	**(For 50 ml volume)**
$CaCl_2$ (MW 147g) 100mM (1.47g)	2.5 ml

HEPES (MW 26.3g) 100mM (2.603g) pH 7.4	5 ml
NaCl 1M	7 ml

2.2.7.1.3 Mitochondrial Membrane Potential (ΔΨm) Analysis by FACS.

Mitochondrial membrane potential (ΔΨm) constitutes a fundamental aspect of the energy storage process and serves as a pivotal indicator of mitochondrial fitness. It provides valuable insights into the underlying electron transport and oxidative phosphorylation processes essential for ATP production. The term "mitochondrial membrane potential" refers to the electrical potential difference (charge gradient) established across the inner mitochondrial membrane. This phenomenon arises due to the uneven distribution of ions and the orchestrated activity of diverse ion transport proteins.

The analysis of mitochondrial membrane potential involves the utilization of afluorescent dyes with selective accumulation properties within the mitochondria, contingent on their charge. MitoTracker dyes (ThermoFisher Scientific), a class of fluorescent probes, were used in the analysis of mitochondrial dynamics and functions. These dyes exhibit preferential accumulation within the mitochondria and exhibit discernible changes in fluorescence intensity upon binding to the organelles. MitoTracker Green (MG) is a cell-permeable, cationic dye that accumulates in mitochondria due to the negative membrane potential. It emits intense green fluorescence in healthy, polarized mitochondria, but the fluorescence decreases in damaged or depolarized mitochondria. On the other hand, MitoTracker Deep Red (MDR) another cationic dye with a longer wavelength emission, it is accumulated in the mitochondria based on their membrane potential, showing a deep red fluorescence in healthy and polarized mitochondria, but reduced the fluorescence in depolarized or dysfunctional mitochondria. During this experiment, Oligomycin a specific inhibitor of the mitochondrial F0F1 ATP synthase, was used. This enzyme complex is crucial for ATP synthesis during oxidative phosphorylation in mitochondria, as it couples the proton flow across the inner mitochondrial membrane to the production of ATP from ADP and inorganic phosphate (Pi). By employing oligomycin to inhibit ATP synthesis and monitoring its impact on mitochondrial membrane potential, facilitates the analysis of mitochon-

drial respiration, coupling efficiency, and the assessment of the functional integrity of the electron transport chain.

Therefore, to assess if CD147 is related to mitochondrial damage, membrane potential (ΔΨm) was measured in SUDHL-1 cells carrying CD147-KO, and SUDHL-1 cells with CD147 WT were used as control. Cells were cultured in T25 culture flasks one week before the infection and split in case of confluency. The SUDHL-1 CD147 WT cells were divided into two conditions, one under standard conditions and the other under hypoxic conditions (6 days of starvation). In total, six different conditions were used for the future experiment: SUDHL-1 cells untreated (CD147 WT), SUDHL-1 under hypoxic conditions (CD147 WT), SUDHL-1 CRISPR neg control (CD147 WT), SUHDL-1 CD147-KO1 and KO2. On the measurement day, $1.2x10^6$ cells per condition were seeded per duplicate in 6-wells plates and diluted in 1 ml RPMI containing 10% FBS, 0.1 β-ME, and 1% P/S. One duplicate was not treated, and the other received 10 µM Oligomycin A (Sigma-Aldrich). All conditions were incubated in the incubation chamber for 2.5 h at 37 °C and 5% CO^2. After incubation, cells were split in triplicate ($1x10^6$ cells per replicate). Every replicate was stained with 100 nM Mito Tracker Green and 10 nM Mito Tracker Deep Red. Cells were incubated for 15 min in the incubator chamber at 37 °C with 5% CO^2. Cells were collected and centrifuged at 850 rpm for 5 min, the medium was discharged, and cells were resuspended in PBS containing 10% FBS. FACS analysis was performed by FACS Calibur (Becton Dickinson), and data were analyzed using FlowJo™ V9.9.6 Software (BD Life Sciences). For normalization and standardization of FACS parameters, SUDHL cells untreated stained only with 100 nM Mito Tracker Green (MG, Thermo Fisher Scientific) or 10 nM Mito Tracker Deep Red (MDR, Thermo Fisher Scientific), and both stains were used. MG was measured in a range of 490/516 nm (FL-1), and MDR was assessed in the range of 644/665 (FL-4). Finally, relative mitochondrial activity was determined based on the fold change of population staining for MDR/MG between untreated and treated groups.

2.2.7.1.4 Transmission Electron Microscopy (TEM).

To evaluate the morphological changes induced by CD147 *in vitro*, cells were evaluated by Transmission Electron Microscopy in the core facility by Dr. Petra Fallier-Becker in the Institute of Pathology of Tübingen. ALK+ALCL cells (SUDHL-1 and KiJK) with CD147-KD and their respective controls were fixed using 2.5% Glutaraldehyde (Electron Microscopy Science) in sodium cacodylate buffer (Merck KGaA), as previously described [180]. Embedding in Araldite (Serva) was performed in Leica EM TP (Leica). The samples underwent polymerization at 60°C, and then ultrathin sections (50-70nm) were obtained by ultramicrotome (Leica) with a diamond knife. Finally, these ultrathin sections were mounted on copper grids for further analysis. Petra Fallier-Becker performed TEM analysis, and TEM images were acquired with an EM10 electron microscope (Carl Zeiss) and a digital camera (Tröndle, Germany). Further inquiries of the mitochondria structural disturbances were quantified in all mitochondria of at least 10 cells per condition (*n*=10 controls and n=10 KD).

2.2.7.2 Experimental mice.

Female 6-8 weeks old NOD scid gamma immune-deficient mice (NSG; Charles River Laboratories, Sulzfeld, Germany) were subcutaneously implanted with 1.5 $x10^6$ ALCL cells (KiJK or SUDHL-1 controls or respective cells with CD147-KD) under anesthesia with 1.5% isoflurane (Abbott, Wiesbaden, Germany) and 98.5% O_2. Animal experiments were authorized by the Regierungspräsidium Tübingen, Germany, and conducted following the German Animal Protection Law's animal use and care protocols. The sample size was calculated in cooperation with the Institute for Clinical Epidemiology and Applied Biometry, University Hospital Tübingen, for exploratory study criteria. In case of suffering, signs of toxicity, intolerance of the treatments, 20% body weight loss, ulceration of the skin, animals were excluded from the study. After three and four weeks, further assessments were performed, including tumor engraftment, tumor growth, tumor glucose uptake, and protein expression using immunohistochemistry.

2.2.7.2.1 PET/MRI analysis to evaluate the xenografts tumors.

PET/MRI scans evaluated tumor engraftment, growth, and glucose tumor uptake. PET/MRI analysis was performed in the Werner Siemens Imaging Center by Dr. Christoph M. Griessinger and supervised by Prof. Dr. Bernd J. Pichler. Mice were injected intravenously with 13±2 MBq of [^{18}F] FDG in a volume between 50-100 µ ofl 0.9% NaCl. Mice were scanned on the Inveon Small Animal PET-Scanner (Siemens Preclinical Solutions, Knoxville, Tennessee, USA) for 10 min after 60 min uptake under anesthesia. Subsequently, the mice were transferred to a 7T BioSpec MRI scanner (Bruker BioSpin MRI GmbH, Ettlingen, Germany). The MRI scans were performed using a rat whole body coil and a T2-weighted 3D TurboRARE sequence (repetition time = 1800 ms; echo time = 66.7 ms; 0.3 mm resolution; averages: 2). PET-image reconstruction a 2D was achieved by a 2D ordered-subsets expectation maximation (OSEM) algorithm with four iterations by using Inveon Acquisition Workplace (Siemens Preclinical Solutions) which results in a pixel size of 128x128 and a matrix size of 0.79x0.79 mm^2. The tumor volumes of interest (VOI) were drawn on the tumors, and the [^{18}F] FDG-uptake was calculated by percentage (%) injected dose per cm^3 (%ID/cm^3).

2.2.7.2.2 Immunohistochemistry of the tumors.

Tumor evaluation of mice was performed in the mouse pathology core facility in the Institute of Pathology of the University of Tübingen by. Ursula Kohlhofer and supervised by Leticia Quintanilla-Martinez. The xenografts tumors were dissected and fixed in 4% formalin and paraffin-embedded. For further histology analysis, 3-5 µm-thick sections were cut and stained with H&E. Immunohistochemistry was performed to evaluate the protein expression of ALK1, CD30, CD31, phospho-Stat3, VEGFR2, MMP7, and MCT1. Appropriate positive and negative controls were used to confirm the adequacy of the staining. CD31 and VEFGR2 histoscore. he histoscore was quantified by multiplying the vessels scale (low=1, moderate=2, and high=3) by the percentage of tumor area presenting the scale grade, rendering a histoscore scale from 0 to 300.

2.2.7.3 Targeted and non-targeted metabolomics was assessed in vitro and in vivo analysis.

Metabolic investigation of the CD147 function in ALCL was evaluated by targeted and non-targeted metabolomic profiling to study both known and unknown metabolites in ALCL cells followed CD147-KD and their respective controls in the xenograft tumors. These experiments were performed in the Institute for Clinical Pharmacology of the Margarete Fischer-Bosch-Hospital in collaboration with Matthias Schwab by Ute Hofmann, Mathias Haag, and Elke Schaeffeler.

2.2.7.3.1 Non-targeted metabolomic profiling.

To identify the small molecular biomarkers, specific to CD147KD, untargeted metabolomic profiling was performed by liquid chromatography quadrupole time-of-flight mass spectrometry (LC-QTOF-MS) analysis, as previously described [181]. First, the frozen xenograft tumors were homogenized in methanol/water (1:1, v/v). Then, the lipids were extracted using methyl *tert*-butyl ether (MTBE)/methanol (3:1, v/v), and two phases were identified. The dried aqueous and dried lipid extracts were restored at a tissue/solvent ratio of 0.03 mg/µl in acetonitrile: water (95:5, v/v) and isopropanol: methanol (3:1, v/v). Following hydrophilic interaction, liquid chromatography (HILIC) separation of the aqueous extracts were analyzed, and further lipid analysis was performed after (Reverse Phase Liquid Chromatography) RPLC separation. Finally, targeted feature extraction of annotated metabolite species was performed. The peak areas were log2 transformed and normalized by median normalization prior to assessing fold changes between tumors with and without CD147 silencing.

2.2.7.3.2 Targeted Metabolomics.

Targeted quantification of metabolites was achieved through Gas Chromatography-Mass Spectrometry (GC-MS) for targeted metabolomics, as outlined in a previous study [182]. This approach enables accurate measurement of specific metabolites of interest, including lactate and a range of intermediates in the tricarboxylic acid (TCA) cycle such as alanine, serine, glucose, pyruvate, fumarate, malate, cis-aconitate, isocitrate, and citrate. The analysis encompassed both tumor tissue homogenates (1 mg) and ALCL cell lines, each subjected to duplicate

measurements. Metabolite extraction from cell pellets (1x106) involved a mixture of 200 µl methanol, acetonitrile, and water (2:2:1, v/v) to ensure proper extraction and integrity preservation. The samples were then stored at -20°C. Quantification of targeted metabolites relied on 10 µl or 20 µl aliquots, with concentrations derived from calibration curves created using known standards of respective metabolites. GC-MS quantification was performed using a TSQ 700 mass spectrometer (Finnigan MAT, Bremen, Germany) operating in Electron Ionization (EI) mode (70 eV) with Selected Ion Monitoring (SIM) capability. This mode selectively monitors specific mass fragments corresponding to target metabolites, enhancing both sensitivity and specificity. Coupled to the mass spectrometer was a 5890 II gas chromatograph (Hewlett Packard, Waldbronn, Germany) equipped with an Rtx-5MS column (30 m, 0.25 mm i.d., dimethylpolysiloxane with 5% phenyl groups, 0.25 mm film thickness; Restek, Bad Homburg, Germany) to facilitate efficient chromatographic separation. The GC analysis employed a split-less mode using helium as the carrier gas at an inlet pressure of 100 kPa, ensuring optimal chromatographic performance. Automated sample injections were facilitated by an A200S autosampler (CTCAnalytics, Zwingen, Switzerland), minimizing potential variability sources and enhancing precision. The chosen standard injection volume of 2 µl and injector temperature set at 280°C were carefully determined to optimize peak resolution and reproducibility.

2.2.7.3.3 XF Cell Mito Stress Test using Seahorse XFe96 Analyzer.

To evaluate mitochondrial fitness in cells with CD147KD, a Seahorse XF Cell Mito Stress calculation was performed. During this experiment, different parameters were investigated, including basal respiration, oxygen consume rate (OCR), and maximal and reserve capacities. First, the XF 96-well cell culture plate was coated with Cell-Tak, following the manufacturer's protocol. Next, cells were settled down for Seahorse XFe96 analysis by centrifugation, according to the protocol for immobilization of non-adherent cells. Cells were subsequently seeded at a density of 7.5 x 10^4 cells per well in 50 µl pre-warmed assay medium (Seahorse XF Base Medium supplemented with 10 mM glucose (Sigma-Aldrich), 2 mM glutamine (Biozym Scientific GmbH), and 1 mM sodium pyruvate (Thermo Fisher

Scientific) pH 7.4). Lastly, relative levels of basal, as well as maximal respiration and OCR, were calculated by Seahorse Wave software (Agilent).

2.2.8 Statistical Analysis.

Descriptive statistics were used to describe the data. Continuous variables were expressed as mean and standard deviation (SD) or median and interquartile range according to their distribution. The distribution was evaluated using the Shapiro-Wilk test and by examining kurtosis, skewness, Q-Q plots, and histograms. Furthermore, the data are presented as bar plots and boxplots and/or as mean ± standard error of the mean (SEM) of a representative experiment in triplicate using Prism Graph-Pad8. Bivariate analysis was performed to compare two groups, Unpaired student's t-test was used for continuous normally distributed variables, while the Wilcoxon rank-sum test was used to evaluate skewed variables. One-way analysis of variance (ANOVA) was used to compare continuous variables in more than two groups. Before analysis, several assumptions were tested, including normal distribution of residuals and homoscedasticity by Levene's test. A pairwise comparison was made using Bonferroni correction. All reported p-values were two-sided, and the significance level was set at ≤0.05. All the analyses were conducted using the statistical program for social sciences IBM SPSS software version 27.0 (IBM, New York, NY, USA) and Prism Graph-Pad8. Figure legends provide specific details on statistical tests for individual experiments.

3. Results.

3.1 Preliminary work evidences target genes of miR-181a and miR-26a.

3.1.1 Efficient overexpression of the miR-181 family and miR-26a in the ALK+ ALCL cell lines.

The tumor suppressors miR-181a and miR-26a were overexpressed in ALK+ALCL cell lines (SUDHL-1 and Karpas 299) in triplicate to identify the genes deregulated after the miRNA transient transfection (Figure 11).

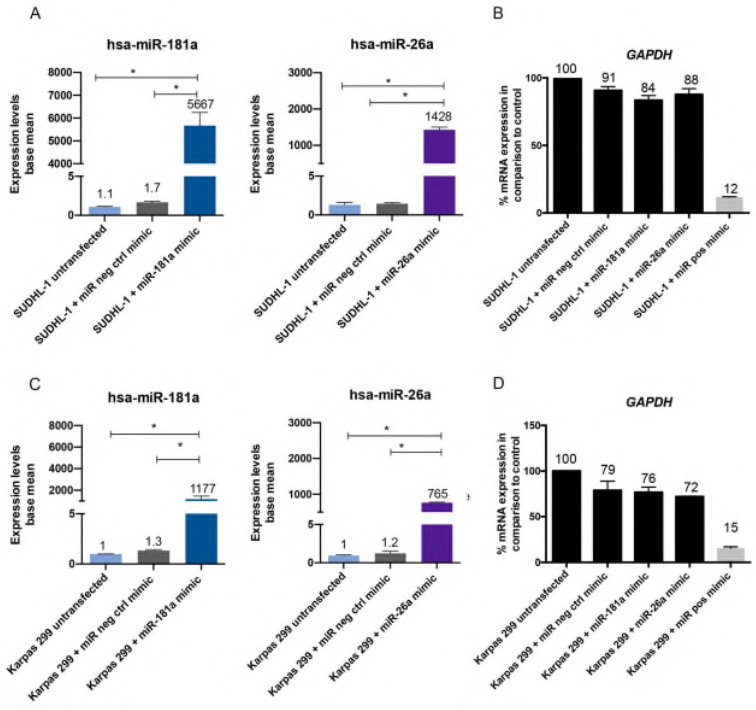

Figure 11. Efficient miR-181a and miR-26a overexpression in ALK+ ALCL cell lines.

A C. Representative graph plots depicting relative expression miRNA 181a and 26a in SUDHL-1 and Karpas 299 by RT-qPCR, 72 h after transfection with miRNA mimics. RT-qPCR was carried out in three independent biological replicates and reactions were performed in technical duplicates, values were normalized to miR-106b, and data were analyzed according to the 2-ΔΔ CT method. **B, D.** Representative graph bars demonstrating the efficient *GAPDH* downregulation. RT-qPCR analysis of *GAPDH* relative expression in SUDHL-1 and Karpas 299, 72 h after transfection with miRNA mimics. RT-qPCR was carried out in three independent biological replicates and reactions were performed in technical duplicates, values were normalized to the housekeeping gene TBP, and data were analyzed using the 2-ΔΔct method. Bars represent the median and the ± SD of the corresponding replicates. Non-published data.

After 72 h, RT-qPCR analysis showed strong overexpression of miR-181a (5203 to 6317 and 975 to 1279 folds higher expression) in transfected SUDHL-1 and Karpas 299 cells, respectively, in comparison to controls. MiR-26a displayed 1346 to 1488 and 754 to 776 folds higher expression in ALK+ ALCL cells (SUDHL-1 and Karpas 299) transfected compared to controls. To further assess the transfection efficiency, the miRNA positive housekeeping control *GAPDH* mimic, which leads to the *GAPDH* gene downregulation, was transfected in parallel. *GAPDH* gene was effectively downregulated in the positive control; *GAPDH* mRNA levels were reduced in 72-88% in SUDHL-1 cells and 57-85% in Karpas 299 cells, with miRNA positive control *GAPDH* transfection in comparison to the SUDHL-1 cells untransfected and SUDHL-1 cells transfected with miR-181a, miR-26a, and negative control mimics.

3.1.2 Transcriptome analysis using Next Generation sequencing displays genes significantly deregulated by miR-181a and miR-126a.

3.1.2.1 Transcriptome analysis.

To identify the genes deregulated after miRNA transient transfection, transcriptome analyses were performed in the cells transfected with miRNA mimics and controls. In summary, more than 40,000 million fragments (100 bp in length) were generated for each sample, above 90% of these fragments were mapped to the reference human genome, and only above 80% of fragments were required for expression quantification (Table 33).

The hierarchical clustering showed a distinct distribution of the gene expression profile between the different groups: SUDHL-1 cells without miRNA overexpression, SUDHL-1 cells with miR-negative mimic, miR-181a and miR-26a overexpression triplicates (Figure 12). The difference in the gene distribution between SUDHL-1 cells with miRNA overexpression and controls represents the differentially expressed genes between the samples. According to the different binding sequences to the target genes of miR-181a and miR-26a (SEED sequences: miR-181a: ACAUUCA; miR-26a: UCAAGUA) 85,100, these miRNAs have differ-

ent target genes, confirmed by the different gene expression distribution between the SUDHL-1 cells with miR-181a and miR-26 overexpression.

Table 33. Fragments used for expression quantification.

ID RNA	n of raw fragments (million)	n of mapped fragments (million)	PFS (%)	NFEQ (million)	PFEQ (%)
SUDHL untransfected	47,829	43.709	91.4	36.086	82.6
SUDHL-1 +miR-NTC-1	56, 432	52.726	93.4	44.106	83.7
SUDHL-1 +miR-NTC-2	57,187	53.425	93.4	44.200	82.7
SUDHL-1 +miR-NTC-3	41,462	38.884	93.8	32.566	83.8
SUDHL-1+miR-181a-1	72,915	68.254	93.6	57.308	84
SUDHL-1+miR-181a-2	50.370	46.772	92.9	39.236	83.9
SUDHL-1+miR-181a-3	100,868	95.293	94.5	80.337	84.3
SUDHL-1+miR-26a-1	78,502	72.554	92.4	61.164	84.3
SUDHL-1+miR-26a-2	48,018	44.225	92.1	36.705	84.3
SUDHL-1+miR-26a-3	42,403	39.664	93.5	33.451	84.3

Abbs: n: number, Pfs: Proportion of sequenced fragments, NFEQ: Number of fragments used. Non-published data.

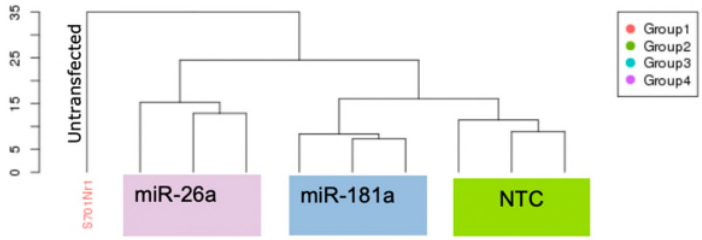

Figure 12. Hierarchical clustering (Euclidean distance) of expression gene analysis in SUDHL-1 cells with miRNA overexpression and controls.

The technical triplicate samples are clustered according to their similarity of rlog-transformed expression data (Euclidean distance) of all genes with at least one sample read. The rlog-transformation from the DESeq2-R-package is used so that all genes contribute equally to the distance between samples. Samples are colored according to the group. The groups are well identified. S701Nr1 represents SUDHL-1 cells untreated; miR-26a represents SUDHL-1 cell triplicates with miR-26a overexpression; miR-181a represents SUDHL-1 cell triplicates with miR-181aa overexpression, NTC, represents SUDHL-1 cell triplicates with non-target miRNA overexpression. Non-published data.

3.1.3 *SLC2A3* is a potential target gene of miR181a, evidence by miR-181a functions related to metabolism.

One thousand four hundred sixty-eight genes were identified as potential target genes of miR-181a as their expression diverged between the control group and the SUDHL-1 with miR-181a overexpression. Among them, only 792 genes (54%) were significantly downregulated (Figure 13 A). 13 target genes were selected as the top candidates based on their differential expression, including (genes depicted in blue): Solute Carrier Family 2 Member 3 (*SLC2A3,* also known as *GLUT3),* Granzyme B (*GZMB*)*,* Carbohydrate Sulfotransferase 2 (*CHST2),* Dynein Axonemal Heavy Chain 1 *(DNAH1),* Collagen Type XVI Alpha 1 Chain (*COL16A1),* Peptidylglycine Alpha-Amidating Monooxygenase *(PAM),* Myosin IF *(MYO1F),* Kinesin Family Member 3B (*KIF3B),* Absent In Melanoma 1 Protein *(AIM-1),* Dual Specificity Phosphatase 6 (*DUSP6),* Pleckstrin Homology Like Domain Family A Member 1 (*PHLDA1),* Misshapen Like Kinase 1 (*MINK1),* ETS Homologous Factor *(EHF), RP5-1028K7.2,* and Macrophage Receptor With Collagenous Structure (*MARCO).*

Among all potential target genes, *SLC2A3* was highlighted as the best candidate gene according to its normalized expression (29151,2 base mean) and its differential expression among the probes (Log2 Fold Change: 0,75, p-value adjusted by FDR: 1,07E-54).

3.1.3.1 miR-181a functions are related to G protein-coupled receptors (GPCR) signaling, ECM organization, and metabolism.

GSEA of differentially expressed genes from a pre-ranked list showed that miR-181 downregulated genes demonstrate a noticeable accumulation of functions related to G protein-coupled receptors (GPCR) signaling, ECM organization, and diseases of metabolism (FDR $p<0.05$). Other functions with higher enrichment scores (FDR $p>0.05$) were related to platelet activation and aggregation, neutrophil degranulation, and metabolism of vitamins, among others (Figure 13 B).

Edge analysis using GSEA highlighted the significant genes leading to the edge subset (Figure 14). The heatmap illustrates the main pathways under miR-181a influence, genes highly enriched, including cubilin (*CUBN*), versican (*VCAN*), and syndecan 3 (*SDC3*). From those, *SLC2A3* was tagged as the top candidate gene

based on their enrichment score, highlighting the function of miR-181a in metabolic reprogramming and ECM organization. Enrichment plots demonstrate the distribution of the gene set and their enrichment score. Positive regulation by miR-181a downregulated genes in pathways such as GPCR ligand signaling (ES 0.70), ECM organization (ES 0.53), GPCR signaling (ES 0.44), and metabolic diseases (ES0.53) is represented by a high number of genes with those functions that rank high on the transcriptome regulation ranking list.

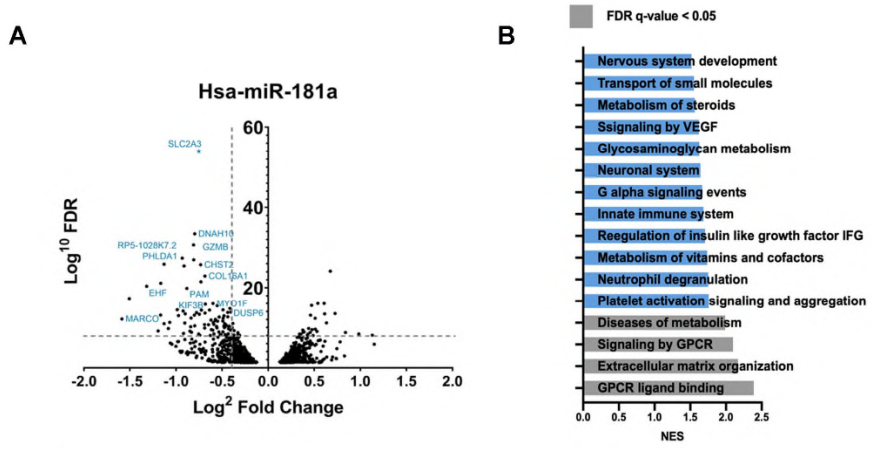

Figure 13. Transcriptome analysis identifies the differentially expressed genes upon overexpression of miR-181a and their related signaling pathways.

A. Deregulated genes in SUDHL-1 cells with miR-181a overexpression. Volcano plot representation of differential expression analysis of genes deregulated in SUDHL-1 cells with miR-181a overexpression in comparison to untreated SUDHL-1 cells in independent biological triplicates. The log2 (FC) (fold change) is plotted on the x-axis, and the negative log10 (FDR, q-value) is plotted on the y-axis. The genes marked in blue highlight the differentially downregulated and potential target genes by miR-181a. **B.** Gene set enrichment analysis (GSEA) of differentially expressed genes in cells with and without miR-181a overexpression. Bar graph plot of the enriched Gene Ontology pathways from GSEA according to their normalized enrichment score (NES) of the pre-ranked genes (Log^2 Fold Change) targeted by miR-181a. Non-published data.

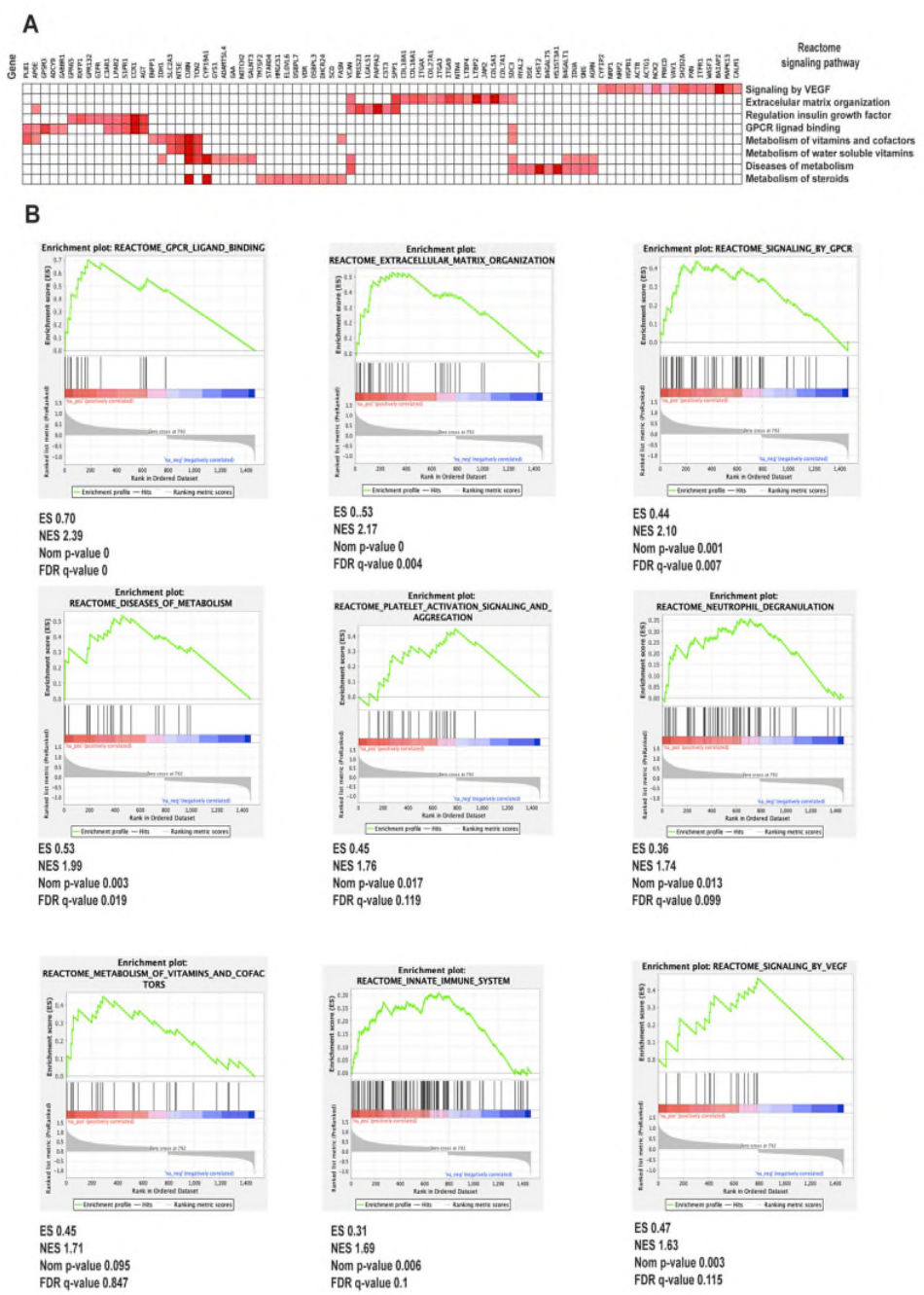

Figure 14. GSEA of genes downregulated by miR-26a.

A. Heat map of the main enriched target pathways; red intensity is related to its enrichment score. **B.** Enrichment analysis illustrates the distribution of the gene set and their enrichment score. The peak of the green line represents the ES and the expression of the target set of genes. In the blot below are depicted the rest of the genes in the pathway set and their position in the pre-ranked list. Non-published data.

3.1.3.2 SLC2A3, KIF3B and COL16A1, are recognized as potential target genes of miR-181a.

Among all differentially expressed genes, 104 candidate genes were selected as potential target genes since these showed a high expression (at least 100 base mean) and were significantly differentially expressed (log^2 Fold Change >0.4). Moreover, from the 104 genes matching these criteria, only 68 genes were predicted as miR-181a target genes according to the binding site prediction algorithms (Supplemental table 1).

According to their function, the miRNA prediction, and their downregulation after the miRNA overexpression, three genes were selected and further validated, including the *SLC2A3*, Glucose transporter 3 *(GLUT3),* and *COL16A1*. The downregulation was corroborated in an independent assay by triplicate using RT-qPCR, displaying a downregulation from 33 to 69% in the selected genes (Figure 15A)

3.1.3.3 miR-181a targets SLC2A3 in ALK+ ALCL cell lines.

miR-181a showed a reproducible downregulation of *GLUT3* of 29 to 51% by RT-qPCR in three different ALK+ALCL cell lines (SUDHL-1, Karpas 299, and KiJK, Figure 15B). In addition, the deregulation of *GLUT3* in ALCL was investigated in vitro in ALK+ and ALK- ALCL cell lines. Relative expression of *GLUT3* showed a reduced expression in ALK- ALCL compared to ALK+ ALCL cell lines (SUDHL-1, Karpas, and KiJK). However, the difference was not statistically significant (Figure 15C). Additional analysis in a comprehensive database showing the expression profile of ALK-dependent genes (GSE6184), using arrays to profile doxycycline-induced or non-induced ALK in ALCL cell lines (SUDHL-1 and SUP-M2), confirmed the high expression of *GLUT3* in ALK+ ALCL and its differential expression between ALK or inducible ALK+ ALCL cells in vitro (Log2 Fold change: 0.52, p-adjusted value: 1,16E-03)[183].

Further validation at protein level was performed using GLUT3 immunostainings on TMAS from primary samples of ALCL patients (n=6, 3 ALK+, and 3 ALK-) and controls (lymph node n=2). Neoplastic cells of ALK+ALCL cases displayed in-

tense (+++) and membranous staining (n=3), in contrast to the inconsistent but substantial homogeneous staining of ALK-ALCL cases (n=2 of 3 cases). Interestingly, the lymph nodes demonstrated a T cell zone selective staining in germinal centers since GLUT3 immunostaining was negative in most of the B-cell population (Figure 15D).

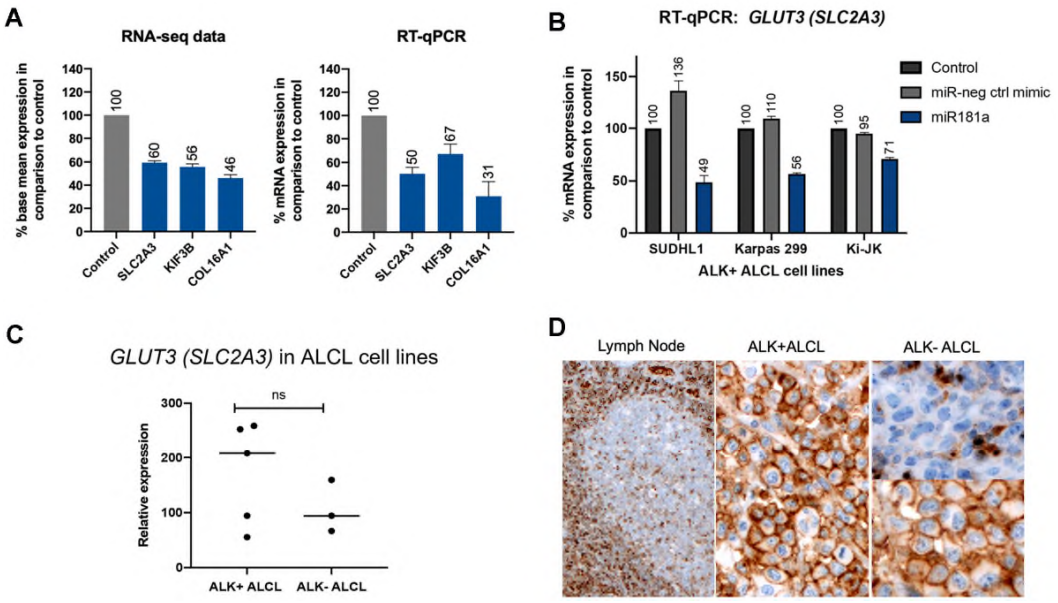

Figure 15. MiR-181a targets *GLUT3,* which is highly expressed in ALK+ ALCL tumor cells.

A. RNA sequencing data and RT-qPCR analysis in ALK+ ALCL cell line (SUDHL-1) 72 h after transfection with miRNA mimics. Graph plots depicting the relative expression of target genes. RT-qPCR was carried out in three independent biological replicates and PCR reactions were performed in technical duplicates; values were normalized to the housekeeping gene *GAPDH,* and data were analyzed using the $2^{-\Delta\Delta}$CT method. Bars represent the median and the ± SD of the corresponding replicates. **B.** *GLUT3* downregulation after miR-181a overexpression. Graph bar depicting the *GLUT3* relative expression evaluated by RT-qPCR in ALK+ALCL cell lines biological triplicates and (SUDHL-1, Karpas 299, and KiJK) with miR-181a overexpression. PCR reactions were performed in technical duplicates. Bars represent the median and the ± SD of the corresponding replicates. **C.***GLUT3* relative expression investigated by RT-qPCR in ALCL cell lines. For analysis, ALK+ (SUDHL-1, Karpas 299, KiJK, SR768, and SUPM2) and ALK− (Fe-PD, Mac1, Mac2a) ALCL cell lines were used. Every point represents the average of the measurements by triplicate. Mann-Whitney-U-Test p=0,3. **D.** GLUT3 IHC in FFPE tissues from patients diagnosed as reactive lymph nodes or as ALK+ or ALK− ALCL. Lymph node: reactive lymph node shows a strong homogeneous cytoplasmatic staining in the T cell-rich zone in comparison to the B cell-rich areas, which show no staining (GLUT3 IHC, original magnification 200x). ALK+ ALCL tumor cells depict strong and homogenous staining compared to the heterogenous staining seen in ALK- ALCL neoplastic cells (GLUT-3 IHC, original magnification 400x). Non-published data.

3.1.3.4 Comprehensive analysis of GLUT3 in ALK+ ALCL.

So far, we have demonstrated the downregulation of *GLUT3* by miR-181a at mRNA level and its high expression in ALCL, apparently independent of ALK status. However, since miR-181a and G*LUT3* functions are enriched in energy metabolism pathways, the exploration of the function of *GLUT3* in ALCL was partially pursued by KO single clones using CRISPR/Cas-9 system. *GLUT3* sgRNA was successfully cloned into pLentiCrispr-V2 (Figure 16). After lentiviral transduction of pLentiCrispr-V2-control and pLentiCrispr-V2-*GLUT3* into Karpas 299 cells, puromycin single clone selection was successful. Western blot of the GLUT3 KO clones demonstrated two potential single KO clones (B and C), depicted in figure 16.

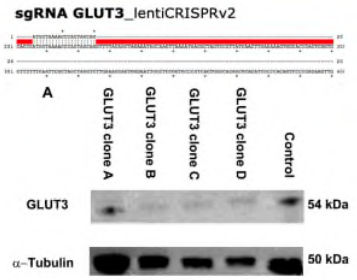

Figure 16. GLUT3 silencing in ALK+ ALCL cell line (Karpas 299).

The upper panel shows a diagram of the selected sgRNA, and the target region edited by CRISPR/Cas 9. Western Blot analysis of GLUT3 in transduced cells using CRISPR/CAS9 KO system. For analysis, 30 µg of proteins were loaded, and α-Tubulin was used as loading control. Non-published data.

3.1.4 *CD93* is a potential target gene of miR-26a, evidence by miR-26a functions related to angiogenesis.

The statistical analysis identified 3694 deregulated genes in SUDHL-1 cells with miR-26a overexpression when compared to control. 488 (12.3%) of these genes were significantly downregulated. Differentially expressed genes across SUDHL-1 cells with and without miR-26a are represented in a volcano plot, which highlights the potential target genes such as ChaC Glutathione Specific Gamma-Glutamylcyclotransferase 1 (*CHAC1*), Leucine Rich Repeat And Ig Domain Containing 1 *(LINGO-1),* Cluster of Differentiation 93 *(CD93),* Thrombospondin Repeat-Containing Protein 1 *(ADAMTSL4*), Myoferlin (*MYC*), Osteoclast Associated Ig-Like Receptor (*OSCAR*), SC2H2C-Type Zinc Finger Transcription Factor (*ST18)* and Mitogen-Activated Protein Kinase 13 (*MAPK13),* Potassium Voltage-Gated Channel Subfamily A Regulatory Beta Subunit 2 (*KNABC2*) and Leucine Rich Repeat Containing 15 *(LRRC15*) (Figure 17A).

3.1.4.1 miR-26a functions are related to immunoregulatory interactions and ECM organization.

Gene enrichment set analysis GSEA of differentially expressed genes from a pre-ranked list showed that miR-26a downregulated genes reveal noticeable accumulation of functions related to immunoregulatory interactions between lymphoid, and non-lymphoid cells, collagen formation and ECM organization (FDR p<0,05, Figure 17B).

Similarly, to the screening of miR-181a function according to its target genes, a GSEA edge subset analysis of miR-26a was performed. The heat map below illustrates the clusters of genes downregulated by miR-26a according to the edge subset, evidencing little overlap between them. Moreover, genes encoding the alpha chain of one of the non-fibrillar collagens did overlap with integrins, as both sets of genes have cell-cell interaction functions. Other integrin family members genes, such as *ITG82,* implicated in cell-cell interaction were also emphasized. In summary, GSEA analysis highlights the role of miR-26a in cell-cell interaction and immune exchange by regulating integrins or genes encoding non-fibrillar collagen.

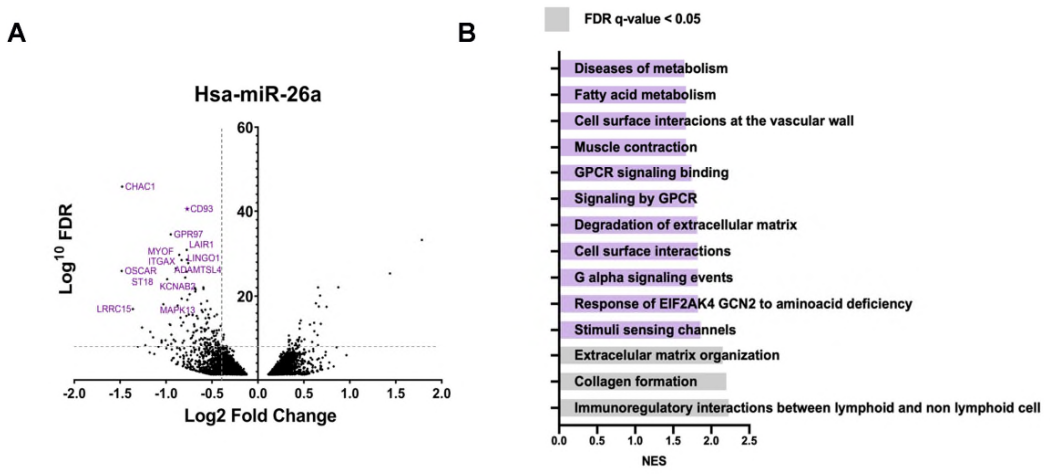

Figure 17. Transcriptome analysis identifies the differentially expressed genes upon overexpression of miR-26a and their related signaling pathways.

A. Deregulated genes in SUDHL-1 cells with miR-26a overexpression. Volcano plot representation of differential expression analysis of genes deregulated in SUDHL-1 cells with miR-26a overexpression compared to control, using independent biological triplicates. The log^2 Fold change is plotted on the x-axis and the negative log10 (FDR, q-value) is plotted on the y-axis. The genes marked in purple highlight the differentially downregulated and potential target genes of miR-26a**. B.** Gene set enrichment analysis (GSEA) of differentially expressed genes in cells with and without miR-26a overexpression. Bar chart indicating the main Gene Ontology pathways resulted from GSEA and normalized enrichment score (NES) of the pre-ranked genes targeted by miR-26a according to the RNA seq data. Non-published data.

The plots of enrichment of the analysis are shown in Figure 18. These plots confirm and explain in detail the enrichment of positive regulation by miR-26a top-ranking regulated genes in signaling pathways such as immunoregulatory interactions between a lymphoid and non-lymphoid cell (ES 0.61), collagen formation (ES 0.60) and matrix organization (ES 0.43).

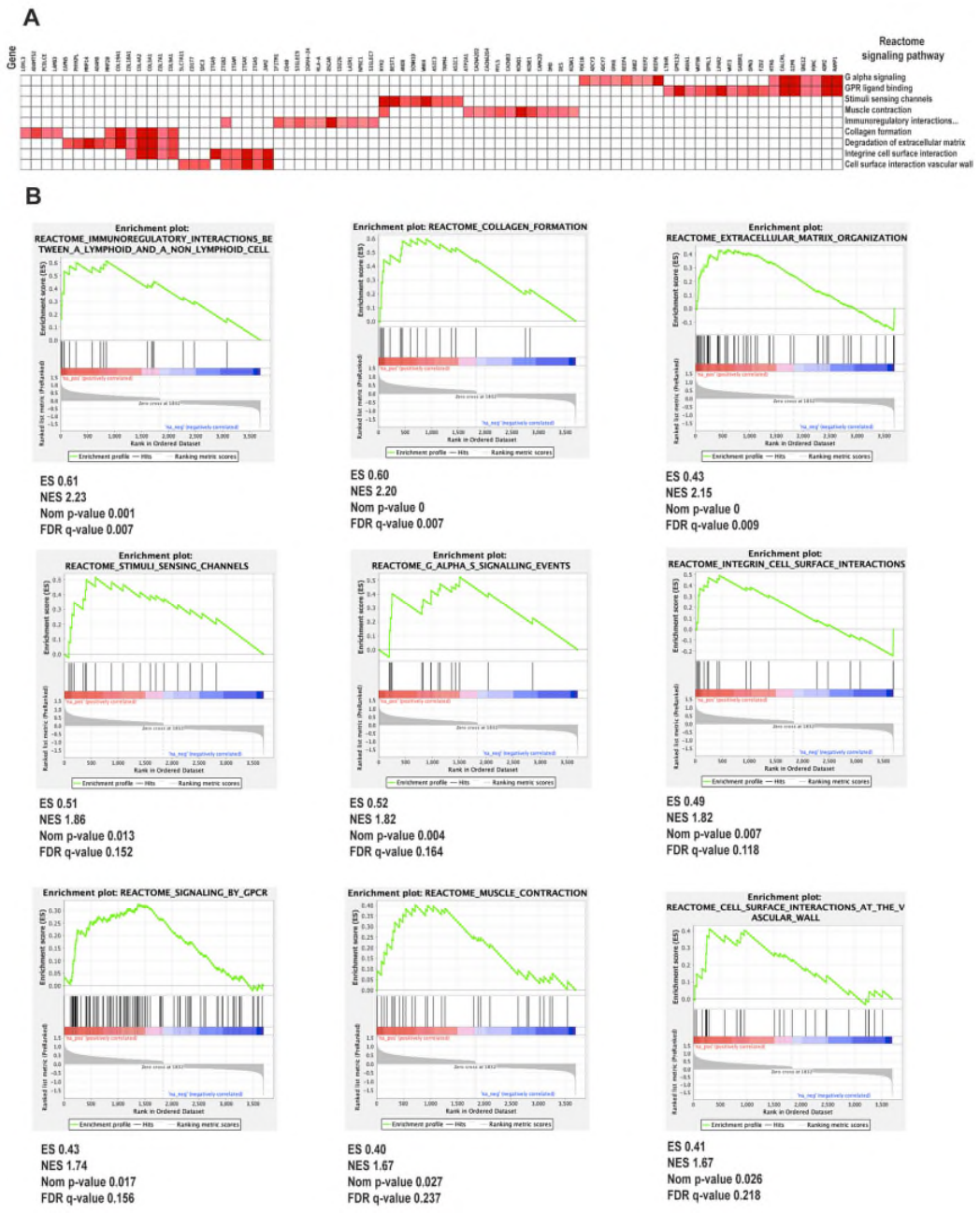

Figure 18. GSEA of miR-26a regulated genes.

A. Heat map of the main enriched target pathways, red intensity is related to its enrichment score. **B.** Enrichment plots of the main pathways involved in GSEA analysis. Non-published data.

3.1.4.2 LINGO1 and CD93, are recognized as potential target genes of miR-26a.

Following the same selection criteria that were established for miR-181a, 96 genes were selected as the best miR-26a candidate target genes; all of them were significantly downregulated ($p < 0.05$), highly expressed (> 100 base mean), and predicted as miR-26 target gene by miRNA target gene prediction algorithms. The genes selected are enlisted in table 33.

From the 96 best regulated genes, ten potential candidate genes were selected for further analysis according to their function and its differential expression including: *CHAC1, LINGO-1, CD93, CLU, SPON2; BCL9L. ITGA5, MAPK13, ST18* and *PLEKGH5*. Validation of these genes by RT-qPCR in an independent miR-26a transfection demonstrated reliable downregulation of three genes (*CD93*, *LINGO*1 and *ITGA5*) of 23 to 66% in SUDHL-1 cells after miR-181a overexpression when compared to control (Figure 24). RNA seq data from transcriptome analysis supported the effect of downregulation demonstrating comparable values: 23 to 42% downregulation according to base mean expression towards miR-181a transfection when compared to control. *ITGA5* regulation was proved to have only a slight effect. In contrast, the downregulation impact was greater in *LINGO1* and *CD93.* The gene *CHAC1* was the best down-regulated gene according to the transcriptome data. However, validation of its downregulation was not achieved due to its low expression in SUDHL-1 cells in RT-qPCR analysis (data not shown).

3.1.4.3 miR-26a targets CD93 in ALK+ ALCL cell line (SUDHL-1).

CD93 was downregulated by miR-26a at least 53% after 72 h transfection when compared to untransfected or transfected with scrambled in SUDHL-1 cells in independent transfection (Figure 19A). However, its downregulation was not striking in the other cell lines such as Karpas 299 anmmed KiJK, in which the expression difference was not perceptible among scramble and cells with miR-26a overexpression (9 to 13% downregulation, Figure 19B). Since miR-26a is an ALK regulated miRNA, the ALK-dependency of its target gene *CD93* was further explored. mRNA expression of *CD93* in ALK− and ALK+ ALCL *in vitro* using RT-qPCR was performed. *CD93* expression in ALK+ ALCL cell lines showed a higher

overexpression, up to 10000-fold times higher than in ALK- ALCL. However, the difference was not statistically significant (p=0.143, Figure 19 C).

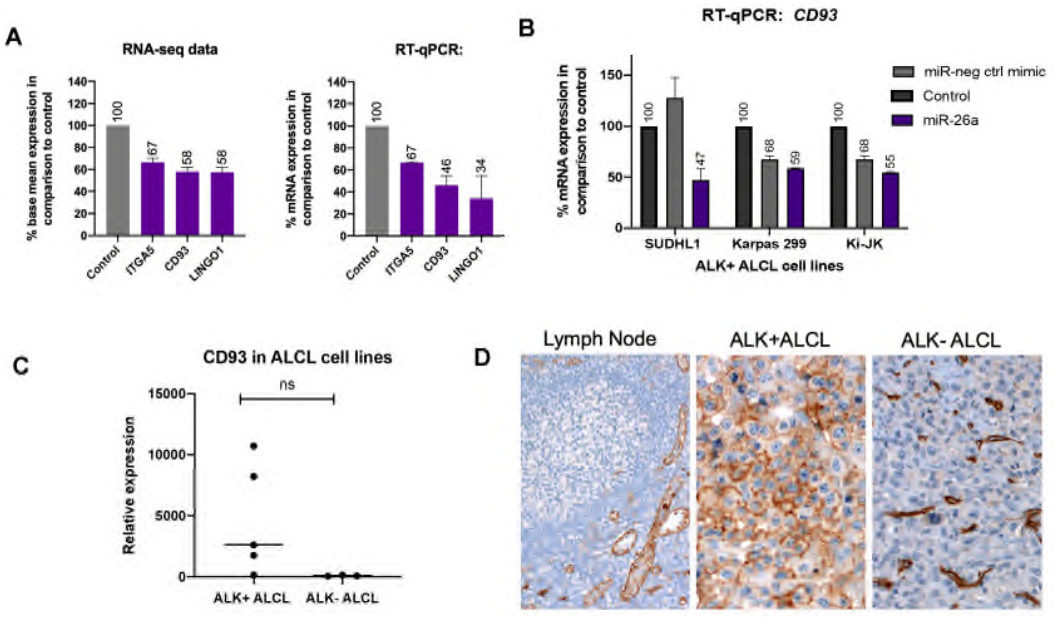

Figure 19. CD93 is overexpressed in ALK+ ALCL and is targeted by miR-26a.

A. Analysis of potential target genes of miR-26a using RNA sequencing data and RT-qPCR analysis in ALK+ ALCL cell line. Analysis was achieved in SUDHL-1 cells, 72 h after transfection with miRNA mimics. RT-qPCR was carried out in biological triplicates and PCR reactions were performed in technical duplicates, values were normalized to the housekeeping gene *GAPDH*, and data were analyzed according to the $2^{-\Delta\Delta}$ct method. Bar plots represent the median and ±SD values of replicates. **B.** *CD93* is highly expressed in ALK+ ALCL and downregulated after miR-26a overexpression. *CD93* relative expression evaluated by RT-qPCR in ALK+ ALCL cell lines (SUDHL-1, Karpas 299 and KiJK) after miR-26a transfection. Bar plots represent the median and ±SD values of biological triplicates and performed in technical duplicates.**C.***CD93* relative expression in ALK+ ALCL cell lines. Graph depicts the relative expression of *CD93*, which was investigated by RT-qPCR in ALK+ (SUDHL-1, Karpas 299, KiJK, SR768 and SUPM2) and ALK− (Fe-PD, Mac1, Mac2a) ALCL cell lines, Mann-Whitney-U-Test P=0.143. Every point represents the average of three independent measurements. **D.** CD93 IHC in primary samples diagnosed as reactive lymph nodes, ALK+ or ALK− ALCL. Lymph node: reactive lymph node shows a homogeneous strong staining limited to the blood vessels (original magnification 200x). ALK+ ALCL tumor cells showing a strong and homogenous membranous staining in comparison to the ALK- ALCL sample, which shows only positive staining in the blood vessels (positive control) (original magnification 400x). Non-published data.

Further analysis in a comprehensive database showing the expression profile of, ALK-dependent genes database (GSE6184), using arrays described previously confirmed the significant differential expression of *CD93* in ALK+ ALCL comparing ALK- or inducible ALK+ ALCL cells *in vitro* (Log^2 Fold change: 0.46, p-adjusted value: 4,48E-03) [183].

Moreover, CD93 immunostainings were performed on TMAS from primary samples of ALCL patients (n=6, 3 ALK+ and 3 ALK-) and controls (lymph node n=2). Interestingly, CD93 IHC showed a limited staining to the blood vessels in the reactive lymph nodes (n=2) and ALK− ALCL biopsies (n=3/3). In contrast, a strong membranous staining in more than 90% of neoplastic cells was observed in the ALK+ ALCL cases (n=2 of 3 cases) (Figure 19D).

3.1.4.4 Comprehensive analysis of CD93 functions in ALK+ ALCL.

Heretofore, we were able to demonstrate the downregulation of *CD93* by miR-26a in ALK+ ALCL (SUDHL-1 cells) at mRNA level in vitro. This regulation seems to be related to the ALK status according to the mRNA and IHC stains. Given the known function of CD93 in angiogenesis and tumorigenesis in solid neoplasms, we decided to further investigate the role of CD93 in ALCL. We pursued CD93 KO single clones using CRISPR/Cas-9 system. *CD93* sgRNA was successfully cloned into pLentiCrispr-V2 (Figure 28). After lentiviral transduction of pLentiCrispr-V2 control and *CD93* into Karpas 299 cells, puromycin single clone selection was successful. Western blot of the clones was performed, CD93 KO (clone A) is depicted in figure 20.

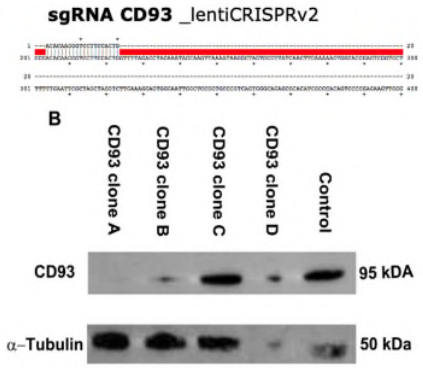

Figure 20. CD93 silencing in ALK+ ALCL cell line (Karpas 299).

Upper panel depicts the sgRNA targeting the CD93 edited region by CRISPR/Cas 9. Western Blot analysis of CD93 in transduced cells by CRISPR/CAS9 KO system. 30 µg of proteins were loaded, and α-Tubulin was used as loading control. Non-published data.

3.2 MiR-146a acts a tumor suppressor in ALCL and targets CD147.

miR-146a showed a different expression when comparing T cells CD3+ to ALK- ALCL and ALK+ ALCL cells. The reduced expression in ALK+ALCL cell lines (SUDHL-1, KiJK, Karpas 299) is at least seven times lower than in T-cells, denoting the tumor suppressor activity by this miRNA (Figure 21).

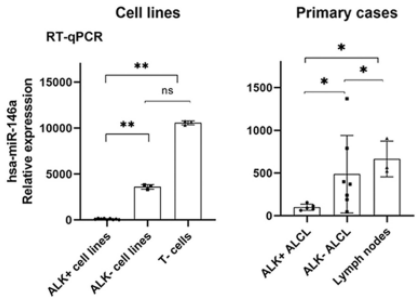

Figure 21. MiR-146a relative expression in ALCL cell lines and primary cases.

The miR-146a expression in the ALK+ ALCL cell lines (SUDHL-1, KiJK and Karpas 299) was compared with the expression in the ALK- ALCL cell line (Mac-1) and in the CD3+ T cells of 3 healthy donors. Five ALK+ ALCL primary cases, seven ALK- ALCL cases and four reactive lymph nodes were also compared. Each point represents the mean value of three independent measurements. The bar graphs represent the median and the ±SD values of the technical triplicates. RT-qPCR values were normalized to miR-106b and analyzed using the 2-ΔΔCp method. Unpaired t-test: ns, non-significant, *p<0.05, **p<0.01. These data were adapted from previous work of Dr. Julia Steinhilber et al. [79,184]

The low expression of miR-146 in ALK+ ALCL was further corroborated in ALCL primary cases and compared to reactive lymph nodes, demonstrating a similar pattern. miR-146a relative expression was reduced at least 10 folds in epithelial cancers, T- or B- cell leukemias, and lymphomas compared to its normal expression seen in T cells (Figure 22) [184]. To identify the target genes of miR146a, its mimic miRNA was transfected in ALK+ ALCL cell lines (SUDHL-1 and Karpas 299), achieving strong overexpression in comparison to controls (Figure 23). In parallel, the transfection efficiency was confirmed by *GAPDH* downregulation by the miR-positive control, as previously described for miR-181a and miR-26 (Figure 23B). Downregulation of positive control reached more than 80% gene downregulation in both cases.

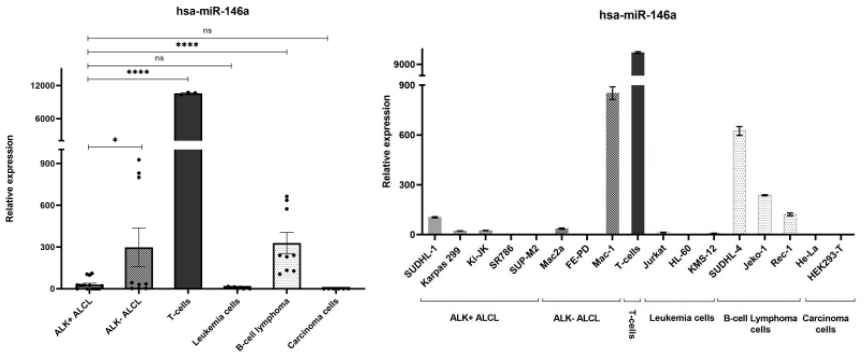

Figure 22. Relative expression of miR-146a in cancer.
Detailed expression of miR-146a in cell lines: ALK+ ALCL cells (SUDHL-1, Karpas 299, KiJK, SR786, and SUP-M2), ALK- ALCL cells (Mac2a, FE-PD, and Mac-1), CD3+ T cells from 3 healthy donors, leukemia cells (Jurkat, HL-60, and KMS-12), B-cell lymphoma cells (SUDHL-4, jeko-1 and Rec-1) and carcinoma cell lines (HeLa and HEK293-T). RT-qPCR values were normalized to miR-106b internal control and analyzed using the 2-ΔΔCp method. Every plot depicts the mean ± SD of three independent measurements. Unpaired t-test: ns, non-significant, *p<0.05, ****p<0.0001. Data published by Montes-Mojarro et al.,[181]

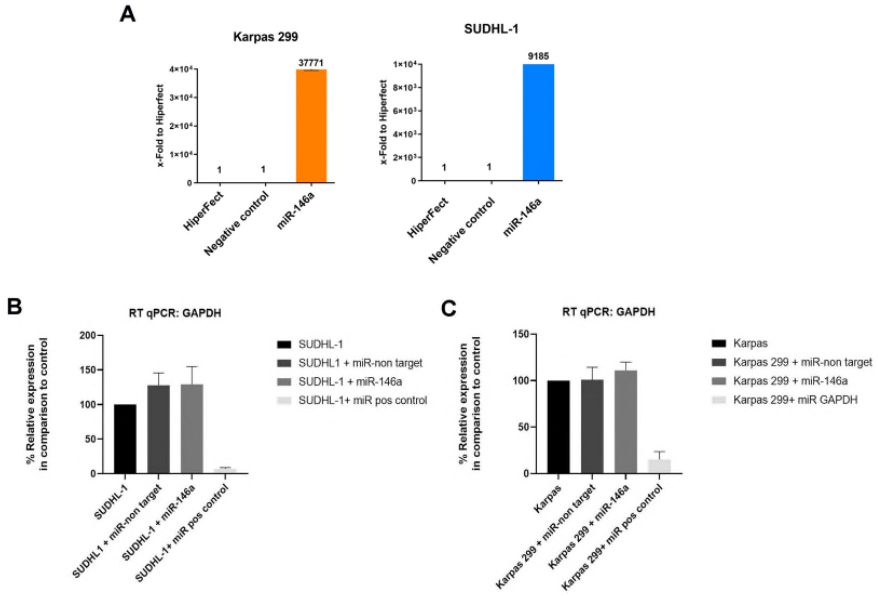

Figure 23. Efficient overexpression of miR-146a in ALK+ ALCL cell lines (SUDHL-1 and Karpas-299) transfected with miR-146a mimic, compared to control.
A. Expression of miR-146a in cell lines 72 h after transfection using biological triplicates. CT values were normalized to the internal control (miR-106b). Data were further analyzed according to the $2^{-\Delta\Delta Cp}$ method for RT-qPCR quantification. The results represent the median of the relative expression in comparison to the levels of the HiperFect treated cells. **B, C.** Representative RT-qPCR of transfection efficiency. The transfection efficiency was calculated by the parallel transfection of the miR-positive control which targets GAPDH. RT-qPCR data indicate the average from biological triplicates and each bar blot is the median and standard deviation

(±SD) per group. These data were adapted from previous work of Dr. Julia Steinhilber et al. [79,184]

Untreated control cells and SUDHL-1 cells transfected with miR-146a were analyzed by transcriptome analysis. More than 100 million reads were generated for both samples, mapped to the human genome. Statistical analysis demonstrated at least 113 genes differentially expressed in SUDHL-1 cell lines with miR146a overexpression compared to control (Figure 24, data adapted from previous work of Steinhilber *et al.*). For further analysis, a similar approach was adopted as for the miRNA previously studied. GSEA data set analysis revealed statistically significant enrichment scores (NES, FDR q-value < 0,5) in the gene ontology pathways associated with vascular endothelial growth factor and phospholipase C activating protein. This analysis highlights the role of miR-146a in angiogenesis.

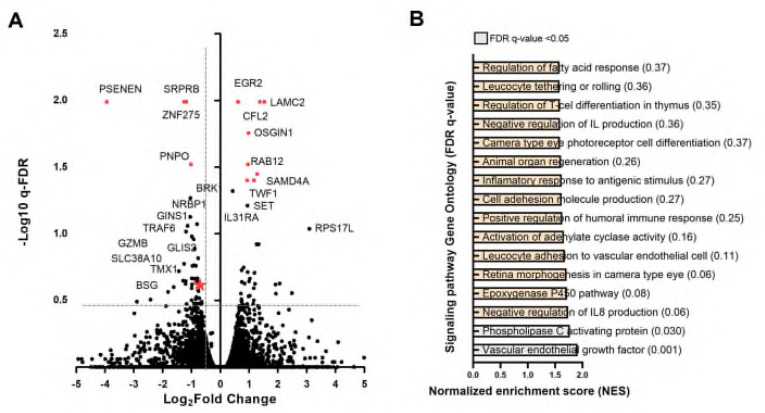

Figure 24. Transcriptome analysis identifying the differentially expressed genes upon overexpression of miR-146a.

A. Volcano plot representation of differential expression analysis of genes deregulated in SUDHL-1 cells with miR-146a overexpression in comparison to untreated SUDHL-1 cells. The log2 (FC) (fold change) is plotted on the x-axis, and the negative log10 (FDR, q-value) is plotted on the y-axis. The genes marked in orange dots highlight the significantly regulated and potential target genes of miR-146a. CD147 is highlighted using an orange star. **B.** Bar graph plot of the enriched Gene Ontology pathways resulted from GSEA. The statistically significant signaling pathway (FDR q-value <0,05) is highlighted in grey. These data were adapted from previous work of Dr. Julia Steinhilber et al. [79,184]

From all potential miR-146a target candidates, four genes were validated, including Pyridoxamine 5'-Phosphate Oxidase *(PNPO),* Signal Recognition Particle Receptor Subunit Beta *(SRPRB), CD147,* and Zinc Finger Protein 275 *(ZN275*). RT-

qPCR confirmed the downregulation of these genes compared to controls (cells untransfected and transfected with non-targeted mi-RNA) of 44 to 54% in SUDHL-1 and 31 to 67% in Karpas 299 cells after miR-146a overexpression (Figure 25).

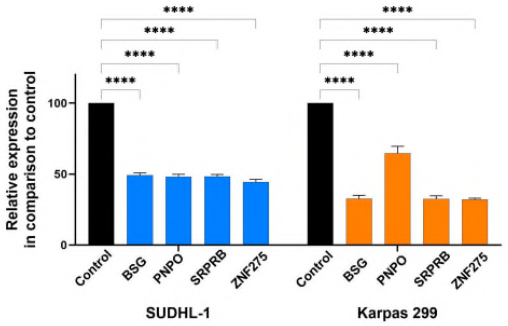

Figure 25. Validation by RT-qPCR of the potential miR146a target genes.

Relative expression levels of the miR-146a candidate genes (*ZNF275*, *SRPRB*, *PNPO,* and *CD147*) were assessed by RT-qPCR analysis in untreated cells and cells upon miR-146a overexpression, SUDHL-1 (blue) and Karpas 299 (orange). RT-qPCR quantification was measured in biological triplicates normalized to ACTB internal control and analyzed using the $2^{-\Delta\Delta Cp}$ method. Bar plots represent the median and ±SD values of replicates. For statistical analysis unpaired t-test was performed [79,184]. Unpaired t-test: ****p<0.0001. These data were adapted from previous work of Dr. Julia Steinhilber et al. [79,184]

WB analyses proved the downregulation of CD147 protein after 72 hours of miR-146a overexpression in ALK+ ALCL (SUDHL-1) cells compared with controls. The reduction of CD147 protein occurred despite the intact function of the activity of the known oncogenic proteins ALK and p-STAT3 (Figure 26).

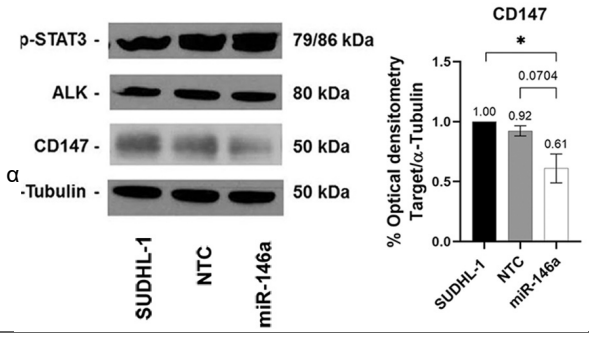

Figure 26. Protein CD147 downregulation upon miR-146a overexpression.

WB analysis of p-STAT3, ALK, and CD147 in SUDHL-1 protein extract with miR-146a overexpression and controls (SUDHL-1 untransfected and transfected with non-targeted mi-RNA). Every line contains 15 µg protein extract, and α-Tubulin was used as loading control. On the left, bar graph of the protein quantification of CD147 by optical densitometry of independent biological triplicates. Bar plots represent the median and ±SD values of replicates. For quanti-

fication, the values were normalized to α-tubulin control and for statistical analysis unpaired t-test was used, *p<0,05. These data were adapted from previous work of Montes Mojarro, Mol. Med. Achim Rau and Dr. Julia Steinhilber et al. [79,184]

3.2.1 MiR-146a directly regulates CD147 in ALK+ ALCL *in vitro.*

3.2.1.1 Successful cloning of the CD147 binding region (3-UTR) into the pmirGLO Dual-Luciferase miRNA Target Expression Vector.

The cloning of the 3 UTR region of *CD147* in the digested pmirGLO dual-luciferase miRNA target expression vector rendered a product of 7780 bp, depicted in figure 27. In this image, the 3'UTR of *CD147* insert is in the multiple cloning sites located just after the firefly luciferase gene.

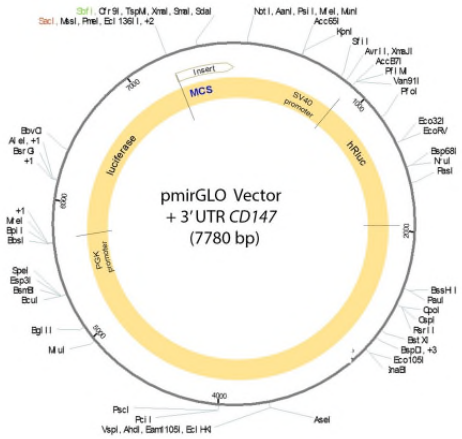

Figure 27. Assembly of pmirGLO vector and 3 UTR CD147 insert.

Assembly was performed using benchling software considering restriction enzymes (Sac I and Sbf I) and insert sequence. Abbreviations: SV40 enhancer and early promoter; hRluc: r*enilla* luciferase; PGK, mouse phosphoglycerate kinase 1 promote, MCS: multiple cloning sites.

Further screening to evaluate the success of cloning carried out by colony-PCR detected effective clones in many samples. Undigested pmirGLO expression vector yielded a product of 227 bp, the expected product conferring the designed primers without the insert. Successful cloning expanded the product size to 702bp in the two approaches (insert:vector ratios: 150:100 ng and 100:100 ng, Figure 28).

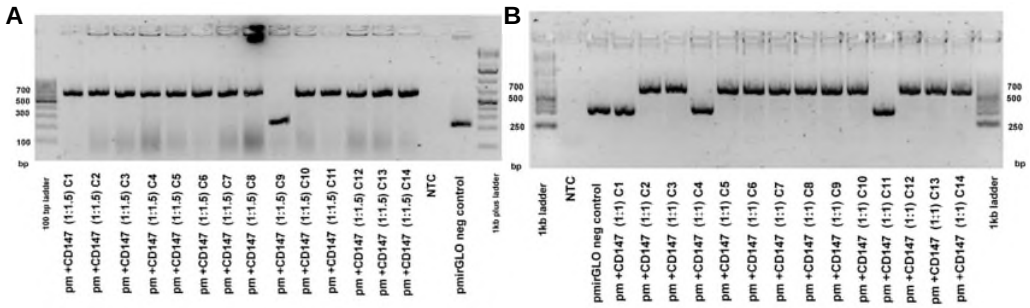

Figure 28. Gel electrophoretic separation of the products for the screening PCR.
A. Insert: Vector 100/150 ng. **B.** Insert: Vector 100/100 ng. Verification of the successful integration of the 3`-UTR segment of mRNA into the pmirGLO dual-luciferase miRNA target expression. 14 bacterial colonies were used as a template and assessed in a 1.5% agarose gel at 140 mV electrophoretically. The PCR product of negative control showed approximately 250 bp, the same size as the undigested vector.

For future experiments, only three clones were chosen and subsequently sequenced using sanger sequencing; an example depicted in Figure 29 highlights the miR-146a binding site in light yellow.

Clone 10, Approach 2. Forward Sanger sequencing

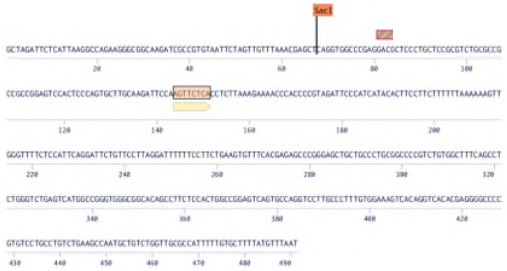

Clone 10, Approach 2. Reverse Sanger sequencing

Figure 29. Verification of the *CD147* 3'UTR segment into the pmirGLO dual-luciferase vector.
Sanger Sequencing of the pmirGLO+CD147 vector (Sample 10, approach 2). Binding site is highlighted (AGTTCTCA). Sequences were uploaded in blenching program for their representation.

3.2.1.2 Luciferase assay detects the miR-146-CD147 direct downregulation.

Potential miR-146a direct regulation was evaluated for *CD147*. Since *SRPRB* was previously confirmed as a miR-146a target gene by Gersmann *et al.* [111]. pmirGLO carrying *SRPRB* insert was used as a positive control for this assay. The relative luciferase activity in He-La and HEK293T cells was significantly reduced for *CD147* in both cell lines after transfection of miR-146a, in comparison to negative controls. Analogous results were demonstrated for the positive control *SRPRB*, confirming that *CD147* and *SRPRB* are likely direct target genes of miR-146a (Figure 30).

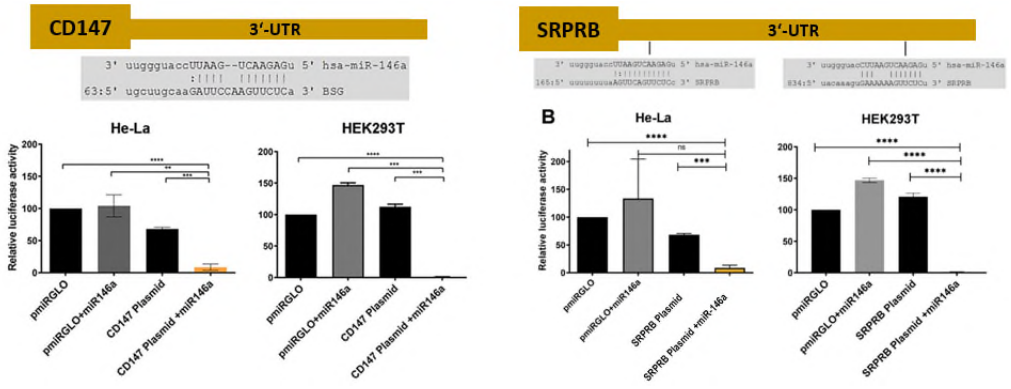

Figure 30. Direct regulation of *SRPRB* and *CD147* by miR-146a using luciferase reporter assays.

The luciferase activity was assessed in the pmirGLO vector containing the *CD147* region targeted by miR-146a. The upper panel depicts the binding site of miR-146a located within the 3´-UTR of the genes according to miRNA *in silico* prediction (www.microrna.org/). The inferior plots display the dual luciferase reporter assays in two cell lines (HeLa and HEK293-T cells), transfected with miR-146a mimic and pmirGLO reporter vector with and without *CD147*-3´-UTR construct. After 40 h of transfection, the relative luciferase activity was assessed (*firefly* LUC / *renilla* LUC). The mean of the triplicates in transfected HEK293-T and HeLa represents the l*uciferase* activity depicted in blots. Unpaired t-test, **p<0.01, ***p<0.001, ****p< 0.0001 [184]. These data were adapted from previous work of Montes Mojarro and Dr. Ann-Kathrin Gersmann [79,184]

3.2.2 CD147 is differentially expressed in ALK+ and ALK- ALCL.

To investigate the CD147 expression in ALCL, ALCL cases were analyzed at mRNA and protein levels. For the mRNA expression levels, three ALK- (Mac-1, Mac-2a, and Fe-PD) and five ALK+ ALCL cell lines (SUDHL-1, Karpas 299, KiJK, SUP-M2, and SR-786) were investigated. ALK- ALCL cells showed a reduced

CD147 expression, but the difference was not statistically significant (p= 0,28, Figure 31A). Simultaneously, 10 ALCL cases were studied, showing higher CD147 expression in ALK+ ALCL cases compared to ALK- cases (p= 0,21, Figure 31B). To further analyze the expression of CD147 at protein level, 95 FFPE ALCL primary cases were investigated, including 81 ALK+ and 14 ALK- ALCL. ALK- ALCL neoplastic cells showed an absent to weak CD147 staining when compared to the ALK+ ALCL tumor cells, which showed moderate to strong staining in most of the cells, rendering a statistically significant higher histoscore in ALK+ ALCL (127.14 +/- 105 vs. 264.64 +/-40, P <0,0001, Figure 31C and D).

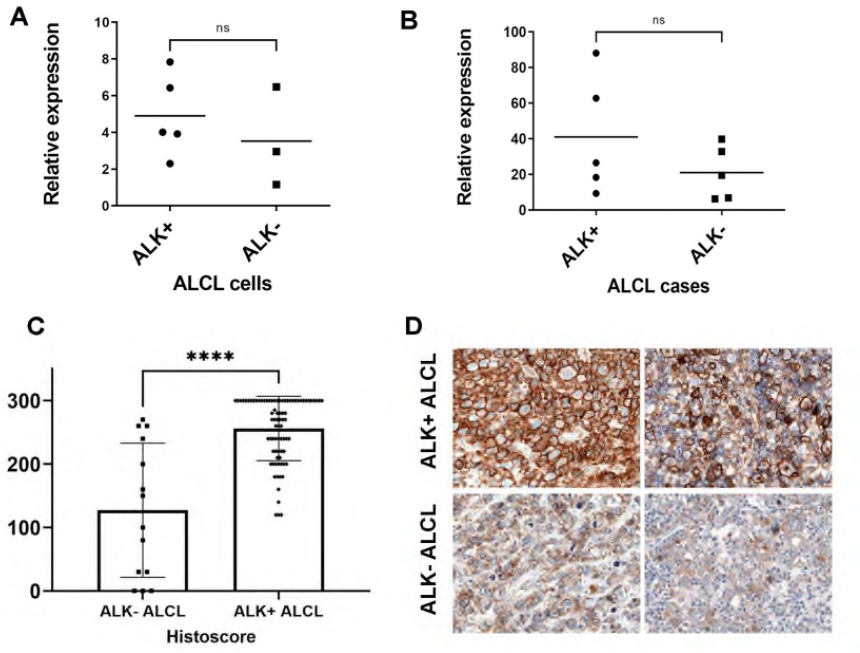

Figure 31. CD147 expression is significantly different in ALK+ and ALK- ALCL.

A. RT-qPCR analysis of *CD147* relative expression in three ALK- (Mac-1, Mac-2a, and Fe-PD) and five ALK+ ALCL cell lines (SUDHL-1, Karpas 299, KiJK, SUP-M2, and SR-786). **B.** *CD147* relative expression in five primary ALK+ and five ALK- ALCL cases using RT-qPCR. For RT-qPCR quantification, the values of the target gene were measured in technical triplicate normalized to ACTB. Results are represented as plots of the ratio of *ACTB*/*CD147*, each single point represents the average of the independent measurements. Wilcoxon rank-sum test (p=0.28 and p=0,21, respectively). **C.** IHC quantification of CD147 in primary cases. Values are expressed as histoscore (intensity/percentage of staining cells). Every point depicts a case. Bar plots represent the median and ±SD values of replicates. Wilcoxon rank-sum test ****p=<0,0001. **D.** Representative cases of ALCL showing the different IHC staining patterns of CD147 in ALCL. ALK- ALCL cases depicts weak membranous staining in comparison to the strong and homogenous staining of ALK+ALCL cases (magnification 400x) [184].

A and B. Data adapted and reproduced from previous work of Dr. Julia Steinhilber et al. **C and D.** Data from Montes Mojarro. Data published [181]

3.2.3 ALK inhibition leads to CD147 inhibition and subsequent increase in miR-146a.

To study in more detail the dependency of the expression of CD147 and miR-146a on ALK, the ALCL cell lines (Karpas 299 and SUDHL-1) were treated with increasing crizotinib concentrations (25, 50, and 100 nM) for a period of 48 hours *in vitro*. WB analysis confirmed the inhibition of ALK activity, which decreased in p-STAT3 and CD147 (Figure 32A, B, and C) expression, which led to an increase in the relative expression of miR-146a. These results pointed out that ALK regulates miR-146a and CD147.

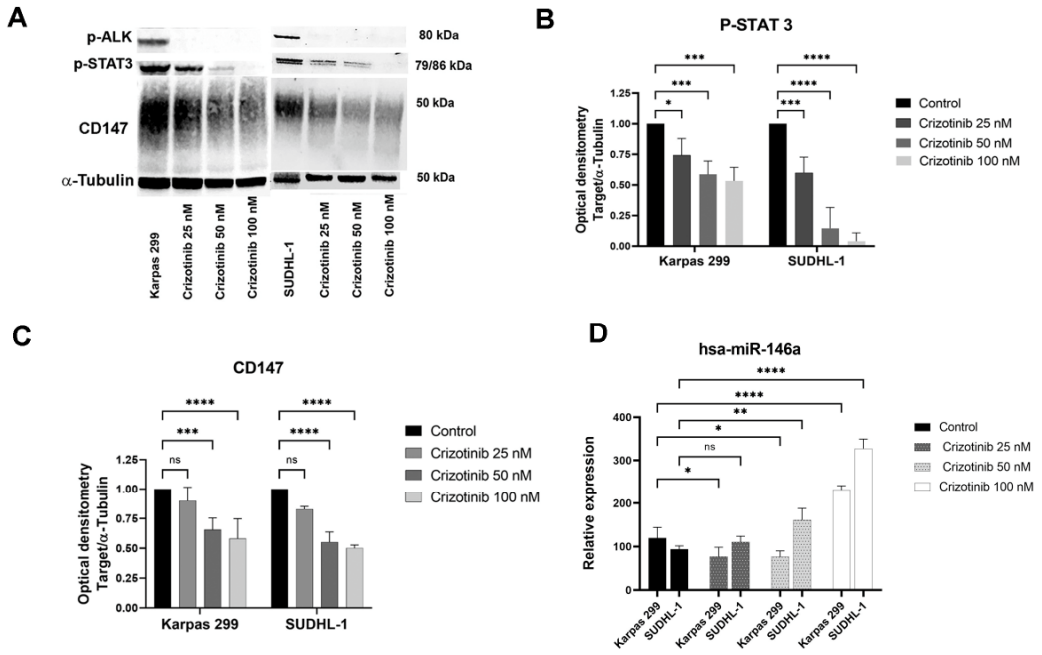

Figure 32. Increasing doses of Crizotinib results in CD147 inhibition with a consequent increase in miR-146a.

A. WB analysis in ALCL cell lines (SUDHL-1 and Karpas 299) after 48 h treatment with increasing doses of Crizotinib. Untreated cells were loaded as control and α-Tubulin as loading control. The proteins P-ALK, CD147, and p-STAT3, were analyzed as indicated. Each lane was loaded with 25 µg protein extract. **B and C**. Bar graphs show the average of three independent optical densitometer measurements of the P-STAT3 or CD147/control ratio. Unpaired t-test was used, *p<0,05, ***p<0,001, ****p< 0,0001. **D**. Relative miR-146a expression levels by RT-qPCR in ALCL cells with increasing Crizotinib doses. Every bar graph shows the average of the corresponding biological triplicates. Unpaired t-tests, **p<0,01, ***p<0,001, ****p<0,0001. Bar plots represent the median and ±SD values of replicates [184]. Data published by Montes-Mojarro et al.,[181]

3.2.4 CD147 promotes survival and proliferation of ALK+ ALCL *in vitro.*

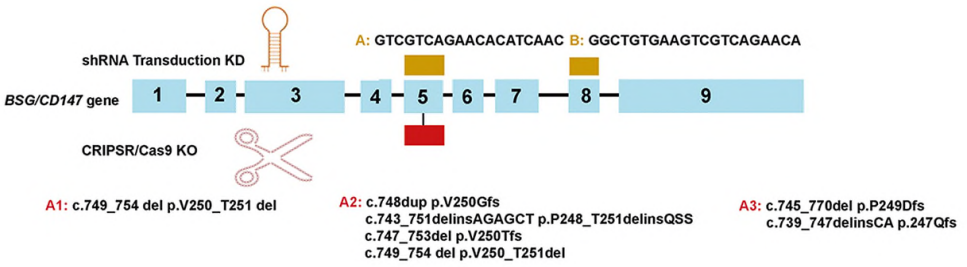

Figure 33. Overview of the *CD147* silencing approaches to investigate the role of CD147 in ALCL.

In the upper diagram, the shRNA hairpins and its targets regions are depicted in gold rectangles, whereas in the lower diagram, the CRISPR/Cas 9 KO approach is represented by showing the target exon and the resulting clones harboring pathogenic mutations (A1, A2, A3). Data published by Montes-Mojarro et al.,[181]

To investigate the effect of CD147 in ALCL, we used a double-tracked approach to eliminate methodological bias and provide robustness to our data (Figure 33). One method was the CD147-KD by transduction of shRNA, while the second approach comprised CD147-KO using CRISPR/Cas9 system.

3.2.4.1 shRNA CD147-KD in ALK+ ALCL cell lines.

Due to their high efficiency in downregulating CD147, the CD147 shRNA "A" and "B" constructs were selected for further analysis. CD147-KD in different ALK+ ALCL cell lines (SUDHL-1 and KiJK) was performed by lentiviral transduction using *CD147* shRNA (pF-CD147) constructs. After 72 h of the second virus infection, efficiency was measured through GFP fluorescence by FACS, which indicated 97.6% to 99.4% infection rates and only 1.9 to 13.8% of cell death, highlighted by PI staining (Figure 34).

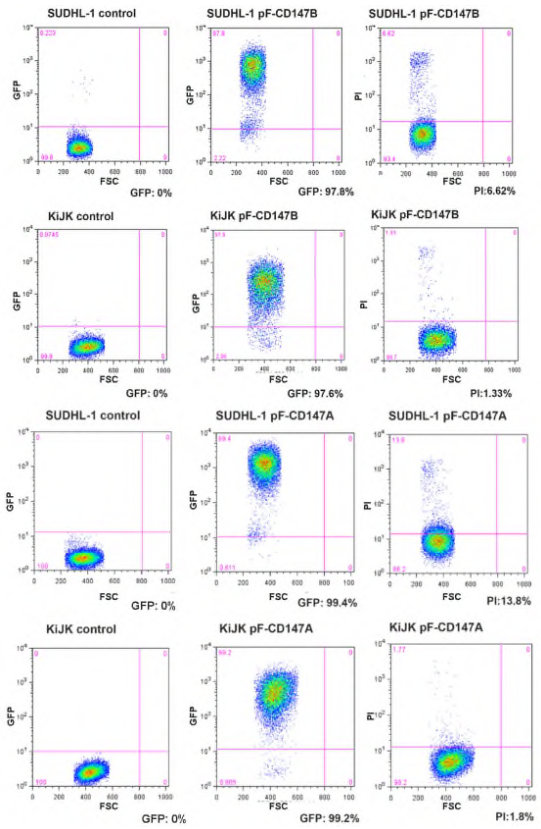

Figure 34. Infection rates after CD147-KD in ALK+ ALCL cells.

Representative FACS analysis of infected and uninfected SUDHL1 and KIJK cells is depicted 72 h after the second infection, measured by GFP-positive cells. Flow cytometric analysis of transduced SUDHL-1 and KiJK cells and untreated controls three days after second infection. The percentage of GFP-positive cells represents the percentage of infected cells whereas the percentage of cells positive for propidium iodide (PI) indicate the dead cells. Forward scatter (FSC). Data published by Montes-Mojarro et al.,[181]

After 7 days of infection, the CD147 downregulation was confirmed at mRNA and protein levels by RT-qPCR and Western blot, respectively. RT-qPCR corroborates the CD147 downregulation of the mRNA in at least 92% in SUDHL1 cells and in 91 and 90% in KiJK cells compared to control cells (Figure 35 A). Western Blot also confirmed the downregulation, demonstrated by a complete absence of CD147 protein in comparison to control in both cell lines (Figure 35 B and C) and the intact expression of the oncogenic proteins ALK, P-STAT3, P-STAT5, and P-STAT1 (Figure 35 B). The growth rate of cells treated with both shRNAs was assessed by MTS assay up to seven or eight days after the second infection to determine the impact of CD147 downregulation. CD147 shRNA-infected cells (pF-*CD147*) exhibited a significant decrease in CD147 protein levels on day eight

of infection, resulting in a growth delay of 59% in SUDHL-1 and 47% in KiJK cells (Figure 35 B and D). Validating lower cell viability and growth retardation in SUDHL-1 and KiJK cell lines infected with pF-*CD147*-A and B (data previously reported by our group).

3.2.4.2 CD147-KO using CRISPR/Cas9 system.

KO of CD147 after CRISPR/Cas9 editing was confirmed at the protein level in single cell clones harboring different deleterious CD147 mutations (A1, A2, A3) targeted by the CD147 sgRNA sequence shown, and characterized by maintenance of CD30, ALK, and p-STAT3 expression but reduction of MCT1 levels (Figure 35 E and F). Growth curves of the single SUDHL-1 CD147-KO clones demonstrated a growth retardation of 48-68% compared to control (Figure 35 G).

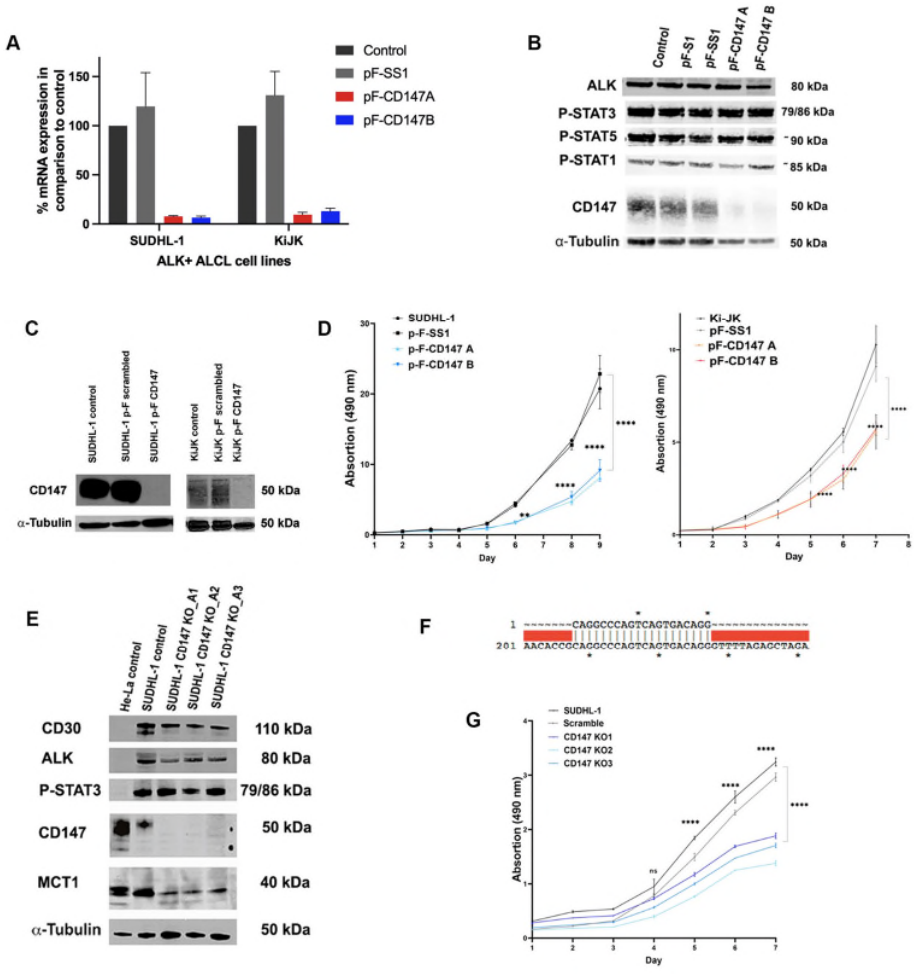

Figure 35. *CD147-KD* and KO in ALK+ ALCL cell lines (SUDHL1 and KiJK).

A. RT-qPCR to assess CD147 relative expression. The triplicates were normalized to control (ACTB) and data were analyzed according to the $2^{-\Delta\Delta Cp}$ method. **B and C.** Western Blot analysis of CD147, ALK, and P-STAT3, P-STAT5 and P-STAT5 in SUDHL-1 and KiJK cells transduced with *CD147* shRNA "A" and "B" seven days after the second infection. For loading, 30 µg protein was used, and α-Tubulin was used as internal control. **D.** Proliferation curves of ALK+ ALCL cell lines with and without CD147-KD up to 8 or 7 days after the second infection, respectively. **E**. Western Blot analysis in SUDHL-1 cells after CRISPR/Cas9 editing. Three different KO clones are displayed for assessment of MCT1, CD147, P-STAT3, ALK, and CD30, using 60 µg of protein. α-Tubulin was used as loading control. For protein detection, lysates of He-LA, and SUDHL-1 cells were used. **F.** sgRNA targeting the CD147 sequence for CRISPR Cas9 is depicted. **G**. Proliferation curves of cells with and without CD147-KO are shown. Error bars indicate ±SD (n=3). For statistical analysis, ANOVA was performed using Bonferroni correction.

Abbreviations: SUDHL-1or KiJK=uninfected cells, F-PSS1=virus containing non-target shRNA, pF-CD147A or B=virus containing the CD147A or B shRNA sequence. SUDHL-1 control=uninfected cells, KO A1-A2 and A3: three knockout (KO) single clones by different mutations.

A, C and D. Proliferation curves performed on by Mol. Med. Achim Rau and replicated by Montes-Mojarro. Data published by Montes-Mojarro et al., [184].

3.2.5 CD147 silencing leads to G0/G1 cell cycle arrest and an increase in apoptosis.

Cell cycle analysis was subsequently performed to investigate the effects of CD147-KD effects in ALCL *in vitro* 4 days after the second infection using pF-*CD147* "B". SUDHL-1 cells with CD147-KD showed an increase in G0/G1 of 8.9 to 15.4% and decreased S phase of 11 to 19.2% when compared to controls (untreated cells or infected with pF-S1 or p-FSS1, Figure 36 A and B). These findings demonstrate that CD147 promotes G0/G1 cell cycle arrest. Apoptosis assessment using flow cytometric with annexin V/propidium iodide stains also corroborated a subsequently increase in the percentage of SUDHL-1 cells with CD147-KD undergoing apoptosis (24.6%) when compared to controls (10 to 12.76%, Figure 36 C and D).

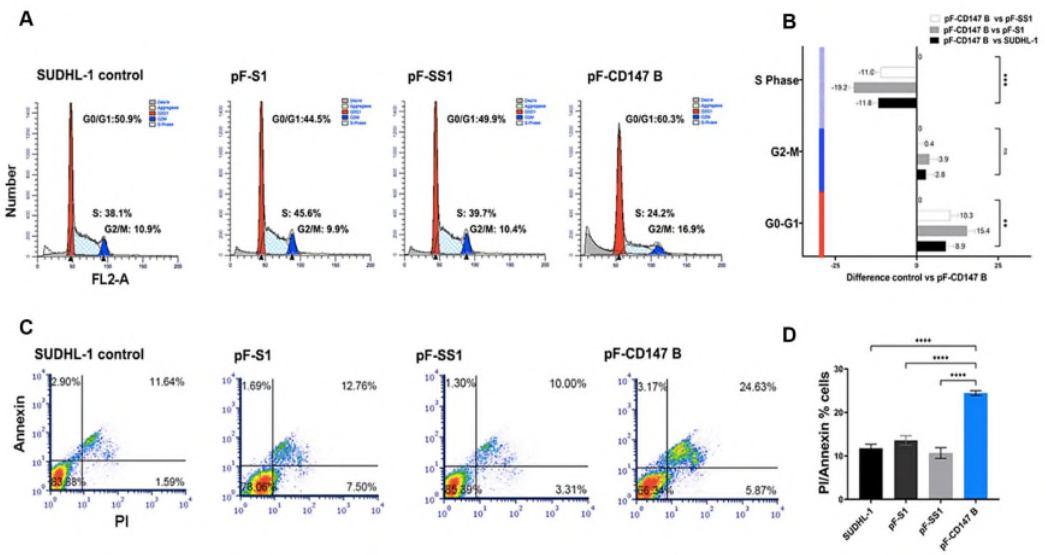

Figure 36. Cell cycle and apoptosis analysis SUDHL-1 cells with CD147-KD.

A. Representative Flow cytometry analysis of the cell cycle distribution of the SUDHL-1 with CD147-KD *vs*. controls (pF.CD147B *vs*. untreated, pF-S, and pFSS1). **B.** The graph plots display the percentages of the CD147-KD cells in comparison to controls in the cell cycle phases; every plot shows the median and standard deviation (±SD) of three independent biological measurements. **C**. Representative Flow cytometry analysis of the percentage of staining cells using annexin V/PI in cells with and without CD147KD. **D.** Graph plots represent the median and ±SD of the three independent biological replicates. For statistical analysis, unpaired t-test, ns = non-significant, *p < 0,05, **p < 0,01, ***p < 0,001. Data published by Montes-Mojarro et al., [184].

Apoptosis assessment using flow cytometric with annexin V/propidium iodide stains also corroborated a subsequently increase in the percentage of SUDHL-1 cells with CD147-KD undergoing apoptosis (24.6%) when compared to controls (10 to 12.76%, Figure 36 C and D).

3.2.6 CD147 silencing contributes to the retarded tumor growth and reduced engraftment *in vivo.*

The influence of CD147-KD was further investigated in a xenograft mouse model. In addition, the NOD scid gamma immune-deficient mice with the previous subcutaneous implementation of ALK+ ALCL cells were analyzed using PET/MRI. All these experiments were performed in collaboration with the Werner Siemens Image Center by Christoph M Griessinger under the supervision of Bernd J. Pichler; only a summary is presented in this thesis. To evaluate tumor engraftment,

four different assays were performed. In the first two assays, different amounts of ALCL cells (SUDHL or KIJK with intact CD147 overexpression, 1,5 $x10^6$ to 3 $x10^6$) were injected to decide the number of cells needed to induce 100% of engraftment. In this assay, all injections induced 100% engraftment when the cell number was equal or > 1,5 $x10^6$ (SUDHL-1 9/9, KijK 9/9, data not shown).

For further evaluation, mice were subcutaneously implanted with 1,5 $x10^6$ ALK+ ALCL cells (n= 5 KiJK, 5 SUDHL-1) with and without CD147-KD. After three weeks, KiJK-1 tumors with CD147-KD resulted in successful transplantation in only 3 out of 5 animals (60%), compared to 5 out of 5 (100%) animals implanted with untreated KiJK-tumors. Similarly, a lower transplantation rate was observed for SUDHL-1 tumors with CD147-KD, as successful transplantation was observed in only 2 out of 5 animals (40%) with CD147-KD, compared with 5 out of 5 (100%) of control animals (Figure 37 A). After 3- and 4- weeks of cell implantation, imaging of the mice revealed reduced tumor growth and engraftment. Tumors harboring CD147-KD were reduced in size 75-fold compared with KiJK tumors with intact CD147 expression (CD147-KD tumors 3.42 ± 4.37 mm^3 vs. untreated tumors: 256.4 ± 153.7 mm^3). Implantation of SUDHL-1 cells harboring CD147-KD also reduced tumor size (CD147-KD :9.4 ± 12.06 mm3; untreated: 324±117.2 mm^3, Figure 37 B and D).

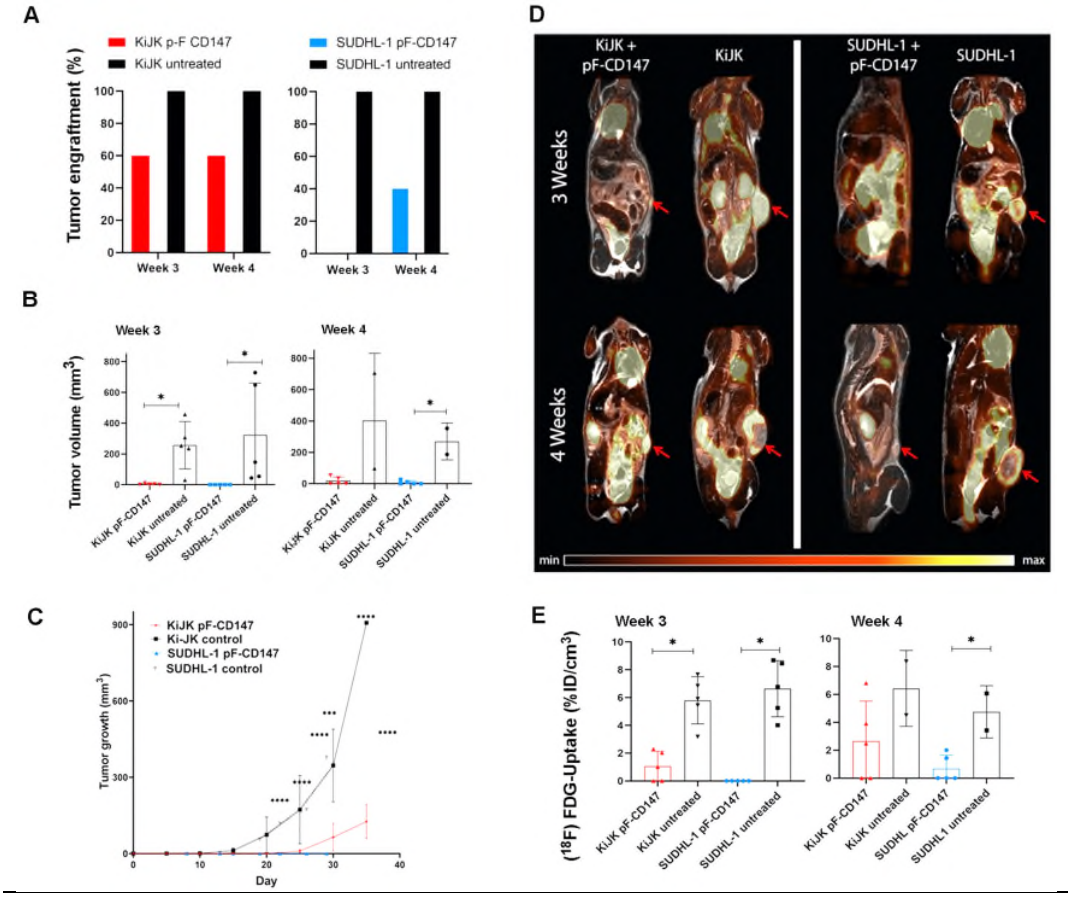

Figure 37. Xenograft mouse model, evaluation of engraftment, tumor growth, and glucose consumption of KiJK and SUDHL-1 cells with CD147KD.

A. Graph plots displaying the engraftment (%) of KiJK- and SUDHL-1-tumors with and without CD147-KD (KiJK tumors: untreated n = 5, uCD147-KD n = 5; SUDHL-1 tumors: untreated n = 5, CD147-KD n = 5). **B**. Tumor volumes assessed by MRI at 3- and 4-weeks after tumor cell implantation. Graph plots depict the mean ± SD of the values, each symbol depicts a tumor measurement. Only two controls were used for measurements at week 4 since 3 animals died before assessment. Wilcoxon rank-sum test was used, *p < 0,05**. C.** Tumor growth curve showing the MRI-derived tumor volume until day 29 after tumor cell implantation (lines represent the mean ± SD, the SD is shown by non-continuous lines; untreated: n = 5, CD147-KD: n = 5). Unpaired t-test was used and repeated measures ANOVA using Bonferroni correction: **p < 0.01 ****p < 0,0001. **D.** PET/MR-scans of mice at 3- and 4-weeks post tumor cell implantation of untreated or KiJK and SUDHL-1 cells with CD147-KD (pF.CD147) (red arrows show the tumors). **E** Graph plot of [18F] FDG uptake in tumors with CD147-KD and controls, means ± SD are depicted, each symbol represents one measurement (untreated: n = 5, CD147KD n = 5). Wilcoxon rank-sum test, *p < 0,05. Experiments performed mainly by PD. Dr. Irina Bonzheim and Dr. Julia Steinhilber and Montes-Mojarro. PET-MRT image analysis by Dr. Griessinger Data published by Montes-Mojarro et al,. [184].

Some mice were sacrificed before the last PET/MRI at week four since tumors reached their final stage. The tumor growth curve validated the growth retardation in tumors with CD147KD compared to the control (Figure 37 C). These findings confirmed that the presence of CD147 in ALCL tumors is essential for the growth

and engraftment of ALCL. PET analysis also showed lower uptake of the glucose analog [18F] FDG in tumors with CD147-KD compared with controls (Figure 37 E). These results demonstrate that ALCL tumors display an increased glycolysis demand, a phenomenon known as the Warburg effect, which in this case is conditional on lactate transport activity mediated by the CD147-MCT1 complex.

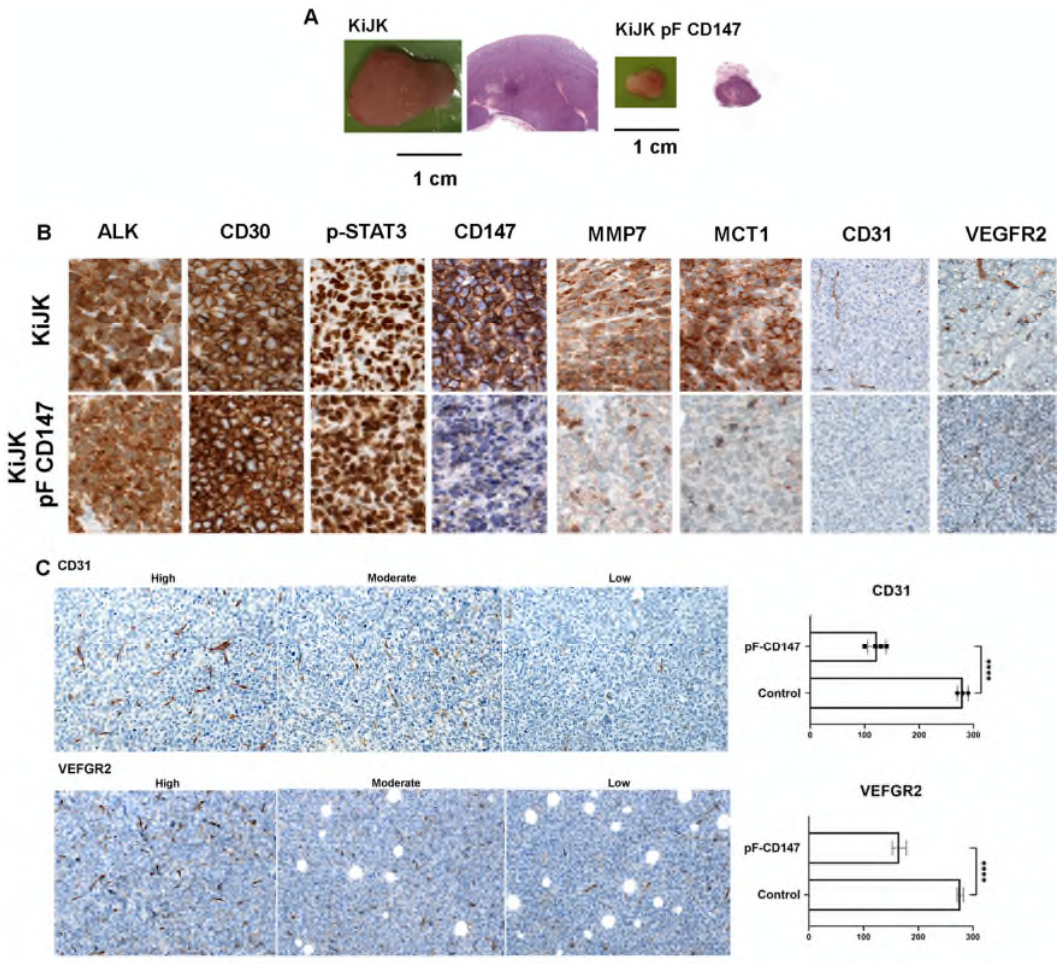

Figure 38. Histological and immunohistochemical evaluation of mouse tumors confirmed the absence of CD147 and the reduction of its functions.

A. Macroscopic representative pictures of tumors with and without CD47KD (H&E, original magnification 12.5×). **B.** IIHC stainings of tumors with CD147-KD and controls showing ALK, CD30, p-STAT3, CD147, MMP7, MCT1 (original magnification 400x), CD31, and VEGFR2 (original magnification 200x). **C.** Representative images of the scale used for CD31 and VEFGR2 quantification. High score was used for areas with more than 20 visible large vessels or more than 30 small vessels; medium score for areas with 10 to 30 small or large vessels; low score for areas with less than 15 small vessels (original magnification, 200x). Quantification is depicted in graph plots representing the mean ± SD (n=3 control tumors and n=3 tumors with CD147KD were used). Unpaired t-test ****p < 0,0001**.** Experiments performed mainly by Prof. Dr. Leticia Quintanilla-Martinez, PD. Dr. Irina Bonzheim and Dr. Julia Steinhilber and Montes-Mojarro. Data published by Montes-Mojarro et al., [184].

For further examination, the mice tumors were examined histologically and by IHC. Mouse tumors with CD147-KD were significantly smaller and lacked CD147-MCT1 complexes than tumors with intact CD147 expression (Figure 38 A-B). The oncogenic proteins ALK, CD30, and P-STAT3 stained strongly and homogeneously in tumors with and without CD147 expression. To further investigate the known functions of CD147 in the context of engraftment, metabolism, and angiogenesis, MMP7, MCT1, VEGFR2, and CD31 were stained (Figure 38 B). Staining showed a considerably reduced number of positive cells for MMP7, CD31 and VEFGR2. To quantify reduced angiogenesis in CD147KD tumors, CD31 and VEFGR2 were used, confirming a reduced histoscore for CD31, and VEFGR2 in tumors with CD147KD compared with controls (Figure 38C).

3.2.7 Mitochondrial damage and accumulation of polarized mitochondria associated to CD147 silencing.

Previous findings indicated the important role of CD147 in reprogramming metabolism by upregulating glycolysis, which is one of the main energy sources of lymphoma cells. Therefore, functions related to tumor metabolism and mitochondrial function were assessed in cells and tumors with CD147-KD and their respective controls. Flow cytometry analysis *in vitro* confirmed decreased mitochondrial potential ($\Delta\Psi m$) by demonstrating a reduction in mitochondrial activity in ALK+ ALCL cells (SUDHL-1) with CD147 silencing compared with the control group. The decreased mitochondrial fitness was confirmed in CD147-KO cells by a higher percentage of cells with low MDR/MG fluorescence compared to the lower percentage seen in control group. In contrast, cells with CD147KD depicted a lower percentage of cells with MDR/MG high fluorescence, indicating fewer cells with intact mitochondria fitness (Figure 39). In parallel, SUDHL-1 cells undergoing starvation (hypoxic conditions) were analyzed, showing a higher percentage of MDR/MG low fluorescence population, also depicted by a higher MDR/MG ratio (Figure 39 B and C).

Electron microscopy examination of ALK+ ALCL cells showed distortion of mitochondrial morphology in cells lacking CD147 expression compared to controls. ALK+ ALCL cells (SUDHL-1 and KiJK with CD147-KD) showed a reduced num-

ber of mitochondria, and those that remained were swollen with disrupted cristae and a reduced number of cristae per mitochondrion (Figure 40).

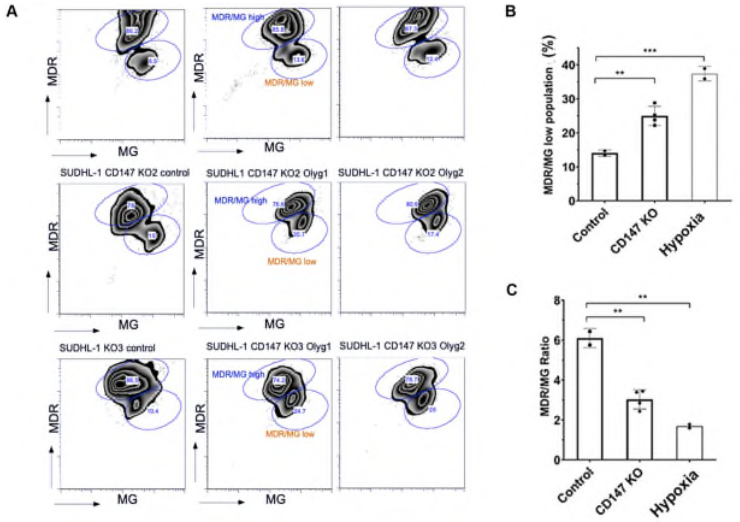

Figure 39. Impaired mitochondrial fitness in ALK+ ALCL cells with CD147-KO.

A. Flow cytometry analysis showing two populations by the fluorescence detection of the MDR and MG dyes, recognized as MDR/MG high and MDR/MG low. Both populations were assessed in SUDHL-1 with intact CD147 expression (CD147 WT, n = 2), in SUDHL-1 cells edited by CRISPR/cas 9 system (CD147-KO, n = 4) and in SUDHL-1 control under starvation conditions (hypoxia). **B.** Graph plot depicts the percentage of cells with MDR/MG low fluorescence. **C.** The MDR/MG ratio for the different conditions is shown in graph plots (every point represents the average of three independent measurements). Unpaired t-test, **p < 0,01, ***p < 0,001**.** Data published by Montes-Mojarro et al., [184]

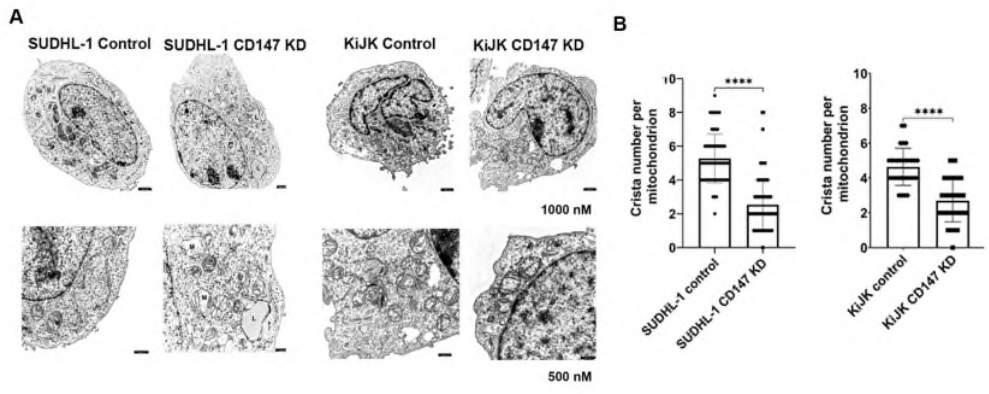

Figure 40. Impaired mitochondrial morphology in ALK+ ALCL cells with CD147-KD.

A. Electron microscopy images in ALCL cell lines (SUDHL-1 and KiJK) with CD147-KD and controls. CD147-KD cells depict reduced number of mitochondria (M). The remained mitochondria are swollen and show reduced number of cristae. In addition, accumulation of lipid droplets is observed**. B.** Graph plots representing the number of cristae per mitochondrion in SUDHL-1 and KiJK with and without CD147-KD. For quantification, all mitochondria in 10 dif-

ferent cells were quantified per cell line (control n = 10 and KD n = 10). Unpaired t-test, **p < 0,01, ***p < 0,001**.**
Electronic microscopy performed in collaboration with Dr. Fallier Becker in the Institute of Pathology and Neuropathology. Data published by Montes-Mojarro et al., [184]

3.2.8 CD147 participates in glucose and lipid metabolism *in vitro* and *in vivo.*

To explore further the impact of CD147 on cellular metabolism, studies such as targeted metabolomics, triglyceride profiling, and XF Cell Mito Stress Test from Xenografts tumors and ALCL cell lines with and without CD147-KD were conducted in collaboration with Dr. Prof. Dr. Matthias Schwab at the Dr. Margarete Fischer-Bosch-Institut für Klinische Pharmakologie. A summary of the main findings is described below.

Metabolomic analyses using liquid chromatography to determine the metabolomic profile comparing mice tumors with and without CD47KD showed that the most important changes in metabolites were concentrated in amino acid metabolism, nucleotide biosynthesis, and lipid metabolism. Tumors with CD147 showed an increase of lyso-phospholipids (e.g., Lyso PC 16:0), free fatty acids, and TAG species, confirming the data of the microscopy image analysis, which show an accumulation of lipid vesicles in the cells with CD147-KD in comparison to controls (Figure 41 A).

Mass spectrometric methods were used to assess the TCA cycle dynamics, depicting a higher rate of glucose entry in CD147-KD tumors. In addition, higher amounts of citrate, aconitate, and α-ketoglutarate (AKG) were also found in the CD147-KD tumors. However, the downstream intermediates of AKG (succinate, fumarate, and malate) showed similar or decreased concentrations. These findings are related to an impaired electron transport chain (ETC) and can be correlated with compromised mitochondrial damage previously reported. In addition, an increased AKG/ratio is reported in tumors and corroborated in ALCL cell lines due to the increased amount of glutamine entry in the TCA cycle, with its subsequent reductive carboxylation of AKG to citrate, as an indicator of reductive glutamine carboxylation (Figure 41 B and C).

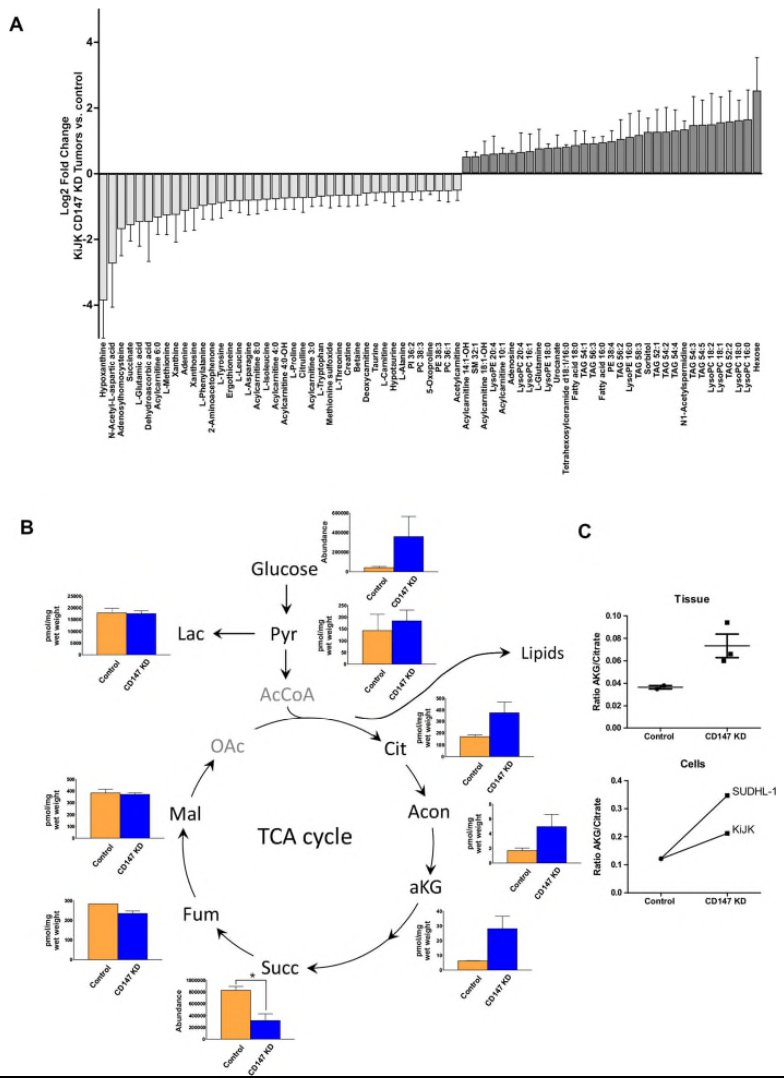

Figure 41. Metabolic profile of tumors and cells with and without CD147-KD.

A. Graphic plot depicting the metabolomic profile of the metabolites that differ between CD147-KD-KiJK-1 tumors and controls. Lots represent mean ± SEM of the log2 fold change >0,5. **B.** Diagram of the TCA cycle demonstrating the concentrations of the TCA intermediates by graph plots. **C.** Ratio α-ketoglutarate (AKG) / citrate in CD147- KiJK tumors, controls, and cell lines (SUDHL-1 and KiJK). For analysis in tumors n = 2 for controls, n = 3 CD147-KD tumors were used. Unpaired t-test, *p < 0,05. Collaboration Dr. Prof. Dr. Matthias Schwab at the Dr. Margarete Fischer-Bosch-Institut für Klinische Pharmakologie. Data published by Montes-Mojarro et al. [184].

Mitochondrial function was further assessed using OCR, a monitor of mitochondrial respiration. Increased basal and maximal respiration values were recog-

nized in ALK+ ALCL cells upon CD147-KD (SUDHL-1 and KiJK) compared to the cells with intact CD147 expression (Figure 42).

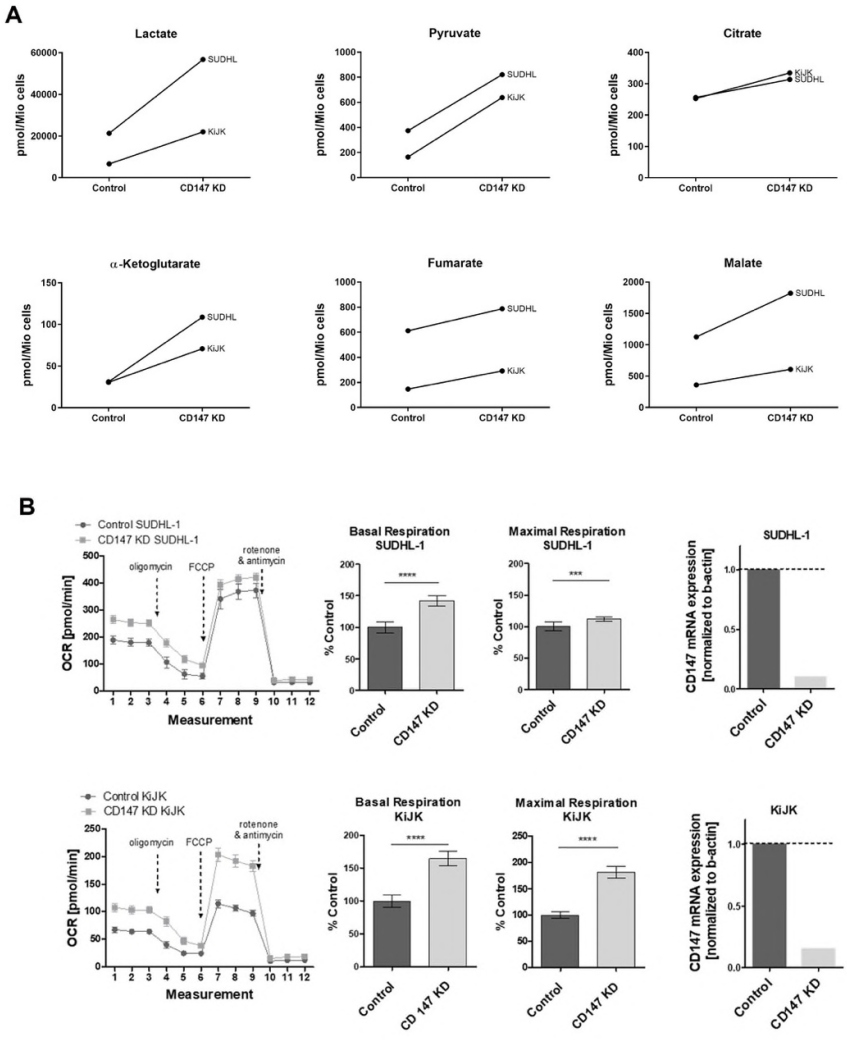

Figure 42. TCA intermediates quantification and OCR measurement in cells ALK+ ALCL cells with CD147-KD.

A. Intracellular concentration TCA cycle intermediates in ALK+ ALCL cell lines with CD147-KDcompared to controls. **B**. Graph plots depicting the oxygen consumption rate in ALK+ ALCL cell lines (SUDHL-1 and KiJK) upon CD147-KD cells compared to controls (each point represents a biological replicate per cell line). CD147 relative expression by RT-qPCR in cells used for metabolic analysis. Unpaired t-test, *p<0,05, **p<0,01, ***p<0,001, ****p< 0,0001. Collaboration Dr. Prof. Dr. Matthias Schwab at the Dr. Margarete Fischer-Bosch-Institut für Klinische Pharmakologie. Data published by Montes-Mojarro et al. [184].

4. Discussion.

Over the past decades, miRNAs emerged as a distinct cellular component differentially expressed in neoplastic and normal cells [185]. Advances in miRNA biology have demonstrated the importance of miRNAs in cancer through their post-transcriptional regulation of gene expression, which is critically dependent on the pairing to their mRNA target [186]. The effects of miRNAs on gene expression may influence oncogenesis by regulating intrinsic cellular processes such as proliferation, differentiation, apoptosis, metabolism, invasion, and metastasis [187]. In addition, numerous studies *in vitro* and i*n vivo* have highlighted the broad clinical potential of these molecules as inhibitors of oncogenesis or as adjuvants of treatment resistance [187,188]. Several studies have identified different miRNA signatures in ALCL by comparing neoplastic cells to normal T cells [79,110]. miRNA profiles related to ALK and C/EBPβ expression are described, recognizing that the oncogene ALK and its target gene *C/EBPβ* have the potential to regulate gene expression by repressing miRNAs, which in normal T-cells act as tumor suppressors [79,110,150]. The study of miRNAs regulated by ALK and C/EBPβ consequently emerged to investigate the role of these miRNAs in tumor development and their potential therapeutic benefit in ALCL cases relapsing to the first-line therapy.

In this work, we focused on exploring the significantly downregulated miRNAs in ALK+ ALCL, including miR-181a, miR-26a, and miR-146a. These miRNAs show moderate expression in ALK- ALCL, low expression in ALK+ ALCL cell lines, and high expression in T cells. Indeed, their expression levels suggest their ALK-dependence and role as tumor suppressors. On top of that, their functions are linked to immune response, angiogenesis, and tumor development, suggesting that these miRNAs represent tumor suppressors whose restitution could be a therapeutic approach in ALCL. Therefore, this thesis aimed to identify the downstream targets of miR-181a, miR-26a, and miR-146a; and to comprehend their function in ALK+ ALCL.

4.1 Issues and difficulties in miRNA target gene identification by transcriptome analysis.

Since each miRNA may have more than 100 target genes in the human genome, identifying and validating miRNA-mRNA targets is essential. Thus far, the most common experimental technique for determining miRNA targets is the assessment of effects on gene expression levels (mRNAs and proteins) after transfection of miRNA mimics or inhibitors such as anti-miRs, antagomiRs, and miRNA sponges [189-191]. Gene expression profiling analysis is available through multiple methodologies, including RT-qPCR, microarrays, RNA-seq, western blotting, and two-dimensional electrophoresis stable isotope labeling amino acids in cell culture (SILAC). In this work, we employed RNA-seq after transient miRNA mimic transfection, given that this method represents a sensitive tool to detect minor changes in gene expression profiles with a broad spectrum of detection. To further investigate the functions of the selected miRNAs, we pursued the identification of their target genes. Given their putative tumor suppressor activity due to their low expression in ALK+ ALCL, we focused on the genes downregulated after miRNA transfection (log^2 fold change >0.5). We applied a low threshold for fold change, considering that the activity of miRNAs on their target genes can be subtle but may still display a robust consequence on biological processes [185].
One of the main challenges of RNA-seq data analysis is the enormous number of genes regulated by a single miRNA. Another foreseeable difficulty is that only a minority of those regulated genes represent direct target genes and the majority of them are due to non-desire side effects of transfection or indirect regulations. RNA seq data analysis following miR-181a and miR-26a mimic transfection revealed a vast list of significantly regulated genes. Inferential statistics and graphical representations narrowed down the number of target genes and exposed the most relevant targets. Nevertheless, the employment of the predictions *in silico*, as previously described [192], represented the ideal guide in selecting the best candidate genes by reducing false positives, genes not predicted as target genes by the computational algorithms [192].

The identification of physiologically relevant targets by computational methods enabled by the recognition of mature miRNA sequences has contributed significantly to the success of miRNA target prediction, especially after identifying the miRNA seed region [193-195]. However, some studies suggest that seed pairing does not always represent a robust predictor since not all pairings show an active biological function. Therefore, experimental validation of predicted miRNA-mRNA binding sites is required. This interaction could be explored using reporter systems such as luciferase reporter assay [196]. In addition, further GSEA analysis assessing the frequency of specific genes and the signaling pathways involved in the significantly de-regulated genes by miR-181a and miR-26a gives some clues to the function of these miRNAs [60], despite the presence of potential false positive target genes in the analysis and predictions.

Since RNA seq data are not adequate to discern between indirect and direct interactions, further experiments are required for these miRNAs to validate and identify the putative target genes, in this case, the luciferase reporter assay. The Argonaute protein cross-linking and immunoprecipitation (Ago-CLIP) method represents an alternative assay. However, this assay has some difficulties in human T cells or lymphoma cell lines since, compared to epithelial cell lines, ALCL cell lines are usually problematic to transfect [195].

In summary, the assessment of miR-181 and miR-26a target genes using RNA-seq remain only pioneer studies that provide an insight into the function of these miRNAs and uncover new target genes in ALK+ ALCL. However, these targets require complementary validation *in vitro* and *in vivo.* Some of the inferences of the exploratory analysis are described in the following sections.

4.2 Understanding the role of miR-181a and *GLUT3*, its primary target gene in ALK+ ALCL.

MiR-181a is one of the many miRNAs conserved among vertebrates, highly expressed in B and T cells. In B cells, its expression is related to differentiation during hematopoiesis [197]. However, in T cells, this miRNA seems to play a role in the adaptative immune response by regulating the TCR signaling pathway and the peripheral T-cell responses [85-87, 68]. In solid tumors, such as prostate carci-

noma, miR-181a is involved in other cancer hallmarks, most notably the regulation of cell metabolism and gene expression. Moreover, the overexpression of miR-181a triggers G1 cell cycle arrest and decreased cell proliferation [198].

In this work, analysis of ALK+ ALCL cells *in vitro* recognized 792 potential target genes of miR-181a. Among all significantly regulated genes, only 68 (8.6%) show a predicted binding site according to the bioinformatic algorithms, excluding >90% of the genes significantly downregulated. Gene enrichment analysis of signaling pathways from monocyte cell lines with miR-181a silencing using Ago-CLIP revealed that the highest ranked genes are involved in MAPK signaling and the regulation of signal transduction, metabolism, immune system regulation, and myeloid leukocyte differentiation [199]. The GSEA analysis in ALK+ ALCL cells *in vitro* revealed that the functions of miR-181a are potentially related to enriched signaling pathways, including the G protein-coupled receptors (GPCR) signaling, the ECM organization, and metabolism.

Considering the commonly regulated activity of GPCRs driving oncogenesis through miRNAs, the matching function of miR-181a is predictable. GPCR molecules are involved in signal transduction, and part of their activity is related to cell motility, differentiation, gene expression, and tumor growth [200]. Hence, induction of GPCRs by miR-181a is not new in cancer; being previously described in chondrosarcomas, in those tumors, miR-181a acts as an oncogene by inducing the expression of RGS16, promoting tumor angiogenesis and metastasis [201].

The interaction between miR-181a and the ECM organization is hallmarked by the deregulation of collagen fibers, integrins, and VCAN. Since the ECM is an essential structural component of the tumor microenvironment that provides a niche for normal and tumor cells and facilitates their proliferation and differentiation [202], the interplay of miR-181a with these processes enhances the invasion mechanism. For instance, in breast and colon cancer, miR-181a promotes cell migration by inhibiting metalloproteinases [203].

An additional essential pathway influence by the activity of miR-181a is metabolic reprogramming. Cancer cells have a high-energy demand, and reconfiguration in the metabolic pathways is crucial for their oncogenesis. Beforehand, the functions of miR-181a were deeply related to metabolism by regulating aerobic gly-

colysis by targeting SIRT1 and ACLS4 in non-small lung cancer cells [204]. In this study, the *GLUT3 (SLC2A3)* member of the glucose solute carrier transporters (GLUTs) is highlighted as the principal target gene of miR-181a in the ALK+ ALCL cell line (SUDHL-1).

GLUT3 overexpression is recognized in neurons, but its expression in other organs is rather low [205]. Its high expression has been previously reported in other cancers such as bladder and DLBCL, distinguishing *GLUT3* as an oncogene [206], which participates in the proliferation of the cells under hypoxic conditions. In DLBCL, its expression is related to the Ki-67 status, confirming the involvement of this oncogene in cell proliferation [207]. In this work, experiments in vitro in ALK+ ALCL cell lines demonstrate that *GLUT3* represents a potential target of miR-181a and confirm that transient transfection of this miRNA leads to downregulation of *GLUT3*, a mechanism previously described in prostate cancer cell lines [198]. However, experiments to elucidate the direct or indirect miRNA-mRNA interactions are required to broaden our understanding of the miR-181a/GLUT3 interaction. *GLUT3* overexpression was confirmed in ALK+ ALCL using RNA-seq data and the database available from previous work by Bonzheim et al [183]. Expression profiling by the array in doxycycline-induced or non-induced ALK in ALCL cell lines also demonstrated differential and ALK-dependent *GLUT3* expression [208] [183]. In this thesis, due to the limited number of cell lines and TMAs employed, it was impossible to confirm this hypothesis further. However, these exploratory experiments confirm that *GLUT3* represents a potential target in ALK+ ALCL, possibly involved in the proliferation and glucose metabolism of ALCL cells.

4.3 Elucidating the role of miR-26a and identifying CD93 as its primary target gene in ALK+ ALCL.

miR-26a is a tumor suppressor miRNA, described initially in pancreatic cancer, acting as a stimulator of proliferation and apoptosis inhibitor. Until now, different target genes of this miRNA are described in various solid tumors, including breast, prostate, and thyroid carcinoma, as well as in hepatoblastoma. In the context of hematological malignancies, miR-26a participates in the differentiation of

AML targeting peroxiredoxin III (PRXIII), a protein with antioxidant properties that can affect oncogenesis [209].

In this work, the tumor suppressor activity of miR-26a in ALCL was investigated by identifying its main target genes *CHAC1, LINGO1, CD93,* and *ITGA5,* which according to their functions and signaling pathway analysis, are majorly related to axon regeneration, immune response, and cell surface adhesion [93-99,210]. Furthermore, subsequent GSEA analysis also confirmed the critical role of miR-26a in immunoregulatory interactions. This likely reflects that miR-26a may influence the immune response, as noted previously in colitis and colon cancer, wherein miR-26a is associated with down-regulation of the immune response through inhibition of nuclear factor κB (NF-κB)/STAT3 and interleukin 6 (IL-6) production [210]. In addition, previous work demonstrated the interaction of miR-26a and INOS, which has an important impact on the inflammatory pathway. However, according to our sequencing data, iNOS was not found among the main targets of miR-26a since the interplay between iNOS and miR-26a in ALK+ ALCL may be discrete and focus on other tumor signaling pathways such as differentiation, cell surface interaction, or angiogenesis [211].

Among all potential genes of miR-26a, *CD93* was selected further as one of the main targets and we focus on its study. *CD93* is a protein usually expressed in endothelial cells, stem cells, and bone marrow [212]. Its expression in immune cells is related to adhesion and invasion, promoting angiogenesis, by promoting the endothelial cell adhesion, making it an ideal target in the study of ALCL [213]. *CD93* represents a tumor biomarker of poor prognosis in various malignant tumors, probably due to its role in the immune response against the tumor [214]. In addition, *CD93* can influence the tumor microenvironment by interacting with the ECM glycoprotein multimerin-2 binding to integrinα5β1 and regulating the activity of integrinβ1 and fibronectin fibrillogenesis *in vitro* [215].

CD93 is a protein mainly expressed in microglial and neuronal cell membranes [216], and its dependence on ALK has interesting implications for cellular signal differentiation, as ALK is also a protein mainly restricted to the developing central and peripheral nervous system [217].

The well-known function of *CD93* as an angiogenic activator may favor the tumor growth of ALCL cells. However, the role of *CD93* in ALCL has not been studied.

According to our data and information obtained from the human protein atlas, the expression of *CD93* is mostly exclusive of ALK+ ALCL [218]. In 46 lymphomas, Hodgkin and non-Hodgkin reported in this database, CD93 expression was absent in all cases, and only blood vessels from the tumor stroma demonstrate homogenous ans specific staining. *CD93* staining in the blood vessels various neoplasias is displayed, including retinoblastoma, melanoma, endometroid carcinoma, Ewing sarcoma, thyroid carcinoma, and ovarian carcinoma. Proposing that the main function of CD93 in those entities is merely related to the activity as an activator of angiogenesis [212].

However, the immunohistochemistry analysis of CD93 in ALCL shows a different outcome than in other solid cancers. In ALCL, CD93 expression is not only exclusive to vascular structures, but also homogenous and strong positive in ALK+ ALCL tumor cells, which raises the question of whether overexpression of this protein plays a significant role in oncogenesis and whether this function is ALK-dependent. The ALK dependency was partially investigated by the CD93 differentially expression in the ALCL cell lines. However further investigation is required to address these questions. As part of this thesis, the CD93 KD using the CRISPR-Cas9 system in an ALK-ALCL cell line was successfully achieved.

In conclusion, this work points to the ALK-miR-26a-CD93 axis in ALK+ ALC cell lines. However, ALK dependence and direct miR-26a interactions, as well as the possible role of CD93 in ALK+ ALCL *in vitro* and *in vivo* remain open questions for future research.

4.4 MiR-146a serves as tumor suppressor in ALK+ ALCL and targets CD147.

In cancer, miR-146a plays a dual function, working as a tumor suppressor in certain cancers but as oncogenic miRNA in others [103]. Its main targets participate in the regulation of key signaling pathways involved in cell proliferation and inflammation, including *NOTCH*, *NF-kB*, *TGFB*, Epidermal Growth Factor Receptor (*EGFR*), arachidonic acid, *PI3K,* and *VEFG* [103]. In ALL, AML, and T-cell lymphoma, miR-146a acts as an oncomir, whereas in B-cell lymphomas and myeloid

malignancies acts as a tumor suppressor. In NK cell and T-cell malignant lymphoproliferation, miR-146a shows low expression levels, acting as a tumor suppressor. Restoring its function *in vitro* resulted in NF-κB signaling inhibition through TNF Receptor Associated Factor 6 (*TRAF6*), inhibiting cell proliferation and activating apoptosis [109].

4.4.1 ALK, miR-146a, and CD147 axis.

Previous work by our research group exhibited the different expression levels of miR-146a in T cells and ALCL, validating and revealing its role as a tumor suppressor [79]. Subsequent comparison of the levels of miR-146a in lymphoma and carcinoma cell lines confirmed miR-146a levels correlates negatively with the expression of ALK, and its low expression is comparable to the expression seen in other carcinomas or leukemias. These data suggest that miR-146a expression correlates negatively with the proliferation of these cancers, as reported for some squamous cell carcinomas [219].

Transcriptome analysis revealed at least 103 potential miR-146a target genes in ALK+ ALCL cell lines with miR-146a overexpression [110]. However, only 9/103 (8.7%) were statistically and bioinformatically predicted as direct target genes. Four genes of these were confirmed as potential target genes of miR-146a, including *ZNF275* (zinc finger protein 275), *SRPRB* (signal recognition particle receptor, B subunit), *PNPO* (pyridoxamine 5'-phosphate oxidase), and C*D147*. All these genes were validated as possible direct target genes at mRNA level, validating a direct or indirect association with miR-146. In addition, CD147 is overexpressed in ALK+ ALCL compared to ALK- ALCL, suggesting that its expression is dependent on ALK expression [34]. Therefore, we direct our further studies to investigate the interaction between miR-146a and CD147 and the role of CD147 in ALCL. Since SRPRB was detected previously as a direct target gene of miR-146a using a luciferase reporter assay in vitro, we employed SRPRB as the positive control for future experiments to prove miRNA-mRNA interactions [111]. Analysis *in silico* by bioinformatic computer algorithms identified the binding site of miR-146a in the 3 UTR region of CD147 and SRPRB, and further studies in HCC supported this data [112]. Experiments *in vitro* using a luciferase reporter

system confirmed the direct interaction between miR-146 and CD147. The binding of miR-146a in the 3 UTR region leads to the downregulation of CD147 in ALK+ ALCL cell lines. This interplay is not exclusive to ALCL and is described in other solid tumors such as NSCLC and kidney tumors [220,221]. miR-146a-CD147 interaction is is limited to the 3 UTR region of CD147. Bioinformatics algorithms poorly predicted other non-canonical bindings and have therefore been poorly evaluated. In order to identify non-canonical bindings is necessary to follow other relatively new strategies, such as the biotin-based pulldown assay [222].

Experiments *in vitro* leading to ALK inhibition by using crizotinib treatment in ALCL+ cell lines (Karpas 299 and SUDHL-1) demonstrated that alterations in ALK expression 24 hours after treatment onset resulted in fluctuations in miRNA expression. In this work, ALK inhibition resulted in the increase of miR-146a and the downregulation of P-STAT3 and CD147 proteins . These assays highlight the sequence and feedback axis of ALK, miR-146a, and CD147. They suggest that inhibition of ALK activity leads to the downregulation of P-STAT3, which affects the overexpression of miR-146a. Consequently, miR-146a directly targets CD147, leading to its downregulation. The miR-146a-CD147 axis has also been proposed to be a key regulator in the oncogenesis of other solid tumors such as HCC, contributing not only to tumor invasion and metastasis but also to the increased angiogenesis [112].

4.4.2 The role of CD147 in ALK+ ALCL

CD147 is a protein enriched in different cancers and stromal cells with various biological functions related to tumor-promoting mechanisms, including cellular proliferation, migration, invasion, increased metabolism, and angiogenesis [115]. Silencing of CD147 resulted in reduced cell proliferation and increased apoptosis. The pathogenic expression and activity of the cell cycle proteins induced by CD147 directly contribute to cancer development and progression in vitro and in vivo, showing CD147 as an important potential therapeutic target in ALCL [223]. However, CD147 also contributes to the lymphomagenesis of ALK+ ALCL by promoting other mechanisms such as tumor invasion, angiogenesis, and cellular metabolism [115]. Imaging analysis using PET-scan displays that the

downregulation of CD147 *in vivo* resulted in reduced tumor engraftment, and reduced tumor growth and reduced [^{18}F] FDG-uptake. Overall, these findings support and underline the function of CD147 in ALK+ ALCL.

Immunohistochemistry assessment confirmed the lack of CD147 expression in treated tumors, and immunohistochemistry evaluation displayed the absence of target proteins related to CD147 oncogenesis. The absent expression MMP7 of tumors was associated with a lack of engraftment of ALK+ ALCL cells or striking tumor growth retardation. These results show that CD147 promotes the invasion and growth of ALK+ ALCL cells. The degradation and organization of the ECM by the induction of MMPs directly influence the tumor microenvironment and create the best scenario for tumor invasion. It was earlier observed that CD147 expression increases the expression and activity of MMPs [123,224,225], resulting in basement membrane disruption and contributing to invasion and metastasis. In addition, MMPs activity enhances VEFG, an activator of endothelial cells, which enhances the permeability in blood vessels stimulating an oncogenic environment by facilitating the transport of oxygen and nutrients to the tumor cells[226]. Silencing CD147 resulted in reduced tumor growth and reduced engraftment of tumors, a mechanism that can be disrupted by the reduced ability of cells to proliferate and invade adjacent tissues. Immunohistochemistry investigation of MMPs in the mice tumors carrying CD147-KD reveals the absence of MMP7 after CD147 silencing, leading us to hypothesize that the CD147 activity supports ECM degradation. The effects of CD147 in tumor proliferation and ECM degradation suggest that CD147 has an essential role in the invasion and cellular growth in ALK+ ALCL, a mechanism shared with other solid cancers [227].

Tumor angiogenesis consists of the proliferation of blood vessels to support tumor growth, promoted by a complex multistep process that involves a broad interaction between stromal/endothelial cells, signaling pathways soluble factors, and ECM components [228] [229]. This mechanism seems to be initiated by the neoplastic cells promoting the secretion of angiogenic factor molecules to respond to the hypoxic demands of the growing tumor. The most critical angiogenic growth factor secreted by the tumor cells is VEFG, predominantly found on endothelial

cells, representing one of the ideal candidates for targeted therapy [230]. Interestingly, in this study, CD147 silencing in mice tumors led to a reduced formation of blood vessels, confirmed by weakened VEFG and CD31 staining and diminished tumor growth. CD31 and VEFG are well-known markers of angiogenesis in the early stage, and their reduction supports the role of CD147 in angiogenesis and its importance for neoplastic cell proliferation. Studies in HCC have focused on the study of the angiogenic role of miR-146, suggesting that miR-146a promotes the expression of platelet-derived growth factor receptor α (PDGFRA) in the endothelial, under the BRCA1 influence, resulting increase in the microvascular invasion, demonstrating another pathway of miR-146 angiogenic regulation (miR-146a BRCA1-PDGFRA1 pathway) [231]. Even though angiogenesis promotes tumor growth, this mechanism is tightly coupled with others hallmarks of cancers such as antiaging, immune response scape, proliferative signaling, invasion and metastases, and maintenance of the high energy tumor demands. Furthermore, angiogenesis plays a specific role by providing oxygen and nutrients for anabolism and removing waste products from cellular metabolism. All these processes and the closed angiogenesis metabolism interaction display and describe a coupled mechanism supporting tumor growth and development [232].

Tumor metabolism takes an essential place in oncogenesis by balancing the high energy demand of cancer cells and maintaining rapid proliferation by promoting aerobic glycolysis, an oncogenic mechanism commonly known as the "Warburg effect" related to the high glucose uptake and glycolysis followed by lactic acid fermentation in cancer cells [233,234]. The activity of CD147 is closely related to the enhancement of the metabolism stimulating aerobic glycolysis and inhibiting mitochondrial oxidative phosphorylation. In this scenario, active aerobic glycolysis is the primary energy source synthesizing macromolecules such as amino acids, metabolites, and lipids needed for rapid tumor growth [233,234].

CD147 can serve as a primary regulator of cell proliferation by promoting reprogramming of glucose metabolism and inhibiting the mitochondrial biogenesis and oxidative phosphorylation of cancer cells [235-237]. A series of studies have indicated that CD147 promotes cell proliferation in T-lymphoma, pancreas carci-

noma, colon carcinoma, and melanoma [116]. CD147 forms complexes of MCTs and amino acid transporters and functions as a chaperone for the folding, membrane expression, and activity of MCT1 [238,239]. The CD147/MCT1 complex leads to upregulation of glucose metabolism and prevents the toxic accumulation of lactate by promoting lactic acid efflux to remove the end product of glycolysis. The function of CD147 in glycolysis reprogramming has been studied using gain and loss of function analysis [126].In addition, CD147 stimulates metabolic reprogramming by suppressing p53 and activating the PIK3/AKT/MDM2 signaling pathway [128]. All these findings led to the conclusion that CD147 overexpression in ALK+ ALL cells leads to a striking decrease in energy metabolism, promoting cell proliferation [127,128].

PET analysis of mice tumors after CD147 silencing showed diminished [^{18}F] FDG-uptake, indicating reduced glucose consumption of ALK+ ALCL tumors, as previously supported by the high intra-tumoral glucose levels indicating reduced aerobic glycolysis in the absence of CD147. Furthermore, *in vitro* studies using EMI also gave some hints about the metabolic changes in CD147-KD and KO assays, denoting the accumulation of TAG metabolites leading to the accumulation of lipid vesicles in ALK+ALCL with CD147-KD. Consistently, our study proves by specific imaging analysis of *in vivo* and *in vitro* that CD147 silencing can robustly reduce glycolytic metabolism and influence tumor growth, as previously described in other studies [126,235]. It also suggests that CD147/MCT1 complexes are necessary for tumor engraftment and may be critical for the viability of ALK+ALCL tumors, pointing out CD147 as an ideal target in this lymphoma.

4.4.3 Mitochondrial damage induced by CD147 silencing.

Further experiments using targeted and non-targeted metabolomic profiling as well as XF Cell Mito Stress Test*, in vivo*, revealed a higher basal respiration rate of ALK+ ALCL cells with CD147-KD denoting that reduction of aerobic glycolysis towards mitochondrial respiration, probably as a mechanism to cope up and fulfill the energy demand of the tumor. This mechanism has been previously reported in colon and lung cancer [240 241].

Reduced mitochondrial potential and morphological mitochondrial alterations seen in ALK+ ALCL cell lines with a lack of CD147 expression may be explained by the metabolic reprogramming induced by CD147. The lack of CD147 and the presence of inactive MCT1 molecules seem to induce mitochondrial oxidative phosphorylation. CD147 absence resulted in the increase of lactate *in vitro* and may have resulted in cellular acidosis inducing remodeling of cristae of the mitochondria triggering changes in mitochondrial respiration and energy production that can be confirmed by the lack of mitochondrial fitness and the presence of swelling mitochondria with disrupted cristae. Such mechanisms are considered to promote survival, are associated with cellular senescence, and have already been identified in hypoxia or stress conditions [242,243]. Interestingly, ALK+ ALCL cells undergoing starvation denote a similar profile to the one seen after CD147-KD. Cells lacking CD147 or under hypoxia conditions show a reduced mitochondrial potential, which possibly increases ROS production and subsequently, cell toxicity [244]. To this extent, hypoxia acts similarly to CD147, promoting glycolysis, but unlike CD147, it inhibits mitochondrial respiratory capacity. These metabolic changes induced by hypoxia favor tumor development and lead to progression, invasion, and metastasis [245].

The metabolic profile observed in ALK+ ALCL after CD147 silencing in this study resembles senescent cells experiencing cell cycle arrest, accumulation of lipid droplets, and showing striking mitochondrial changes [246]. Comprehensive analysis of the mitochondrial remodeling in these cells is essential since mitochondria are not only important as the main source of energy, but these organelles are also essential for plenty of cellular processes, including cell cycle, apoptosis and cellular metabolism [247]. Cellular senescence and mitochondrial impairment represent hallmarks in cancer and aging [246]. As described before, senescence cells show non-functional mitochondrial with a decreased mitochondrial membrane potential, increased proton outflow and increased ROS products, partial uncoupling of oxidative respiration, and increased basal respiration as a mechanism of compensation [246,248]. However, a decreased fatty acid oxidation also results in the accumulation of lipids [249].

Non-targeted metabolomics performed in the mouse xenotransplant model after CD147-KD highlighted the enrichment of glucose levels by the tumor and the

shifting of TCA metabolites. This metabolite profile goes in accordance with the mitochondrial impairment, leading to a reductive glutamine metabolism to maintain the TCA cycle. Reductive glutamine metabolism involves the conversion of a-ketoglutarate to citrate and represents a coping phenomenon to support the growth of cells with mitochondrial impairment. The ketoglutarate/citrate ratio itself is an essential measure of reductive glutamine utilization and an indication of lipid accumulation since reductive glutamine metabolism is a primary source of fatty acid synthesis [250]. The high elevated Ketoglutarate/citrate observed in tumors and cells with CD147 silencing, showed in ALL+ ALCL, denotes only metabolism shifts responding to the mitochondrial impairment.

A hypothesis for the lipid accumulation in ALK+ ALCL cells after CD147-KD is the impaired cholesterol metabolism seen in ALK+ALCL, which leads to downregulation of squalene monooxygenase (SQLE), preventing the cholesterol formation and the accumulation of squalene in lipid droplets. Squalene accumulation is not in all cancers a damaging mechanism but in some tumors, such as lung cancer is related to tumor development [251]. Lipogenesis can also be stimulated in ALK+ ALCL by activation of the transcription factor SREBP1c, which as well as other genes which encode lipogenic enzymes are reported as target genes of CD147 promoting the AKT-mTOR signaling pathway [124]. All this highlights that lipogenesis is a highly active process within cancer cells and can be found in other neoplastic disorders such as HCC. The presence of tumor droplets in lymphoma cells is not exclusive to ALK+ ALCL and has also been reported in other aggressive entities such as Burkitt lymphoma [252], denoting the emerging roles of lipids in the oncogenesis and therapy of these lymphomas [253].

In summary, these findings suggest that CD147 denotes not only a biomarker of ALK+ ALCL. It also represents a promising targetable gene since it regulates cellular metabolism and mitochondrial function by inducing a senescence profile that favors oncogenesis. In addition, CD147 induces tumor proliferation, angiogenesis, invasion, and metastases [234], and its inhibition is deleterious for survival of tumor cells. Accordingly, targeting CD147 has shown some promising results. *In vivo* and *in vitro* assays showed promising results by using the anti CD147 humanized antibody. In HCC, this antibody leads to PI3K-AKT signaling pathway,

resulting in reduced invasion and metastasis. CNTO3899 another CD147 antibody, has also been proved successfully in mouse models of head and neck cancer, resulting in reduced tumor growth and proliferation [254]. Clinical assays using a ^{131}Iodine labeled murine monoclonal antibody against CD147 named Licartin have shown promising results in the treatment not only in patients with HCC but also in melanoma patients [255,256,257]. This antibody is proven to be safe and can be used in the clinical therapy of HCC in China (approval number S20060064). Furthermore, an additional recombinant monoclonal antibody against the C2 extracellular domain of human CD147 (Metuzumab) was developed to enhance its antibody-dependent cellular cytotoxicity activity, resulting in higher affinity and efficacy. This antibody has been tested in esophageal cancer and could represent a therapeutic option for these patients [258]. More recently, new immunotherapies using CD147 a target (CD147-chimeric antigen receptor -CAR) stand also under investigation *in vitro* and *in vivo* in HCC [259]. More recent studies demonstrated that immunomodulatory drugs including thalidomide and its derivatives lenalidomide and pomalidomide also modulate CD147 by interfering with the cereblon-CD147-MCT1 axis, inhibiting tumor development, suggesting an alternative pathway to target CD147-driven tumorigenesis [260].

4.4.4 Deciphering the specific route of miR-146a in ALK+ALCL.

Our data confirmed that low miR-146a expression in ALK+ ALCL correlates with CD147 high-level expression. The strong CD147 expression in ALK+ ALCL contributes to lymphomagenesis in several ways, including enhancing invasiveness through induction of MMPs and angiogenesis and stimulating cell growth through its robust connection to energy metabolism *in vitro* and *in vivo.* Given its involvement in a variety of oncogenic mechanisms, CD147 has the potential to emerge as a novel therapeutic target in ALK+ ALCL [184].

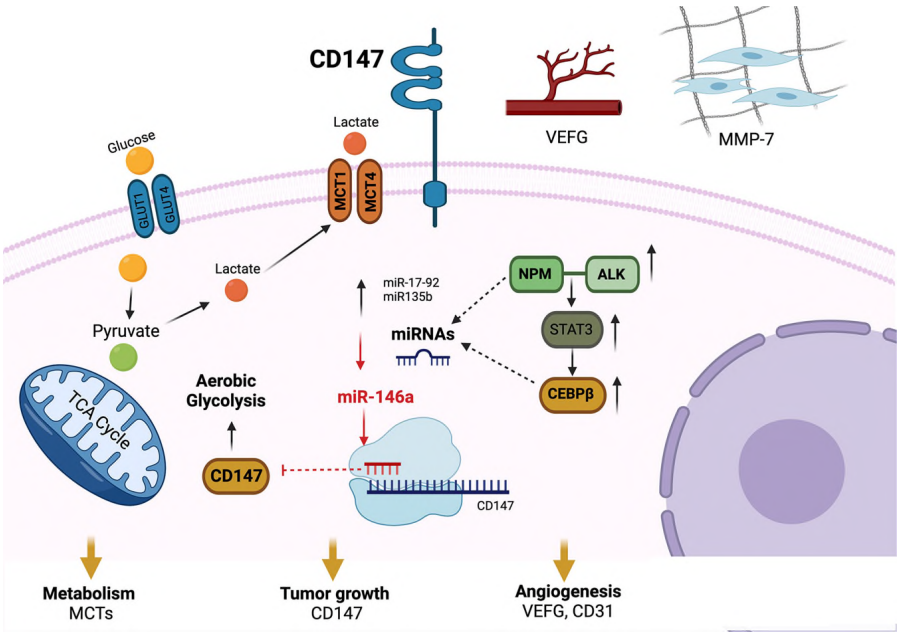

Figure 43. Graphic summary of the role of miR-146 in ALK+ ALCL.

NPM-ALK leads to CD147 expression through downregulation of miR-146a and overexpression of *C/EBPβ* via the STAT3 signaling pathway. CD147 promotes tumor growth and invasion by enhancing metabolism and promoting angiogenesis in ALK+ ALCL [184].

4.5 ALK-regulated miRNAs contribute to the oncogenesis in ALK+ALCL by downregulation of genes related to metabolism, tumor proliferation, and invasion.

The expanding knowledge of miRNAs and their functions opens new avenues for therapeutic intervention in cancer. Further investigation of new gene targets and their impact on cellular pathways is essential for the development of novel therapies. The use of miRNAs specific therapies provides some advantages over other therapies, such as siRNAs since miRNA therapy influence an entire cellular process rather than targeting a single gene. Given that lymphomagenesis is a complex multistep process involving several mechanisms giving cells the ability to proliferate and invade other tissues, the use of comprehensive therapies may be advantageous. However, it is essential first understand the role and the different

cellular processes regulated by each miRNA in order understand the potential effects of miRNA therapy better. The therapy with miRNA can involve different strategies, such as the downregulation of oncogenic miRNAs or the reconstitution of the tumor suppressor miRNAs [261]. However, for their efficient use, some technical approaches need to be investigated further [261]. Until now, some miRNAs have reached clinical development, including a mimic of the tumor suppressor miRNA miR-34, which is under phase I clinical trials for treating cancer [262].

In xenograft models of B-cell non-Hodgkin lymphomas (B-NHL), experiments demonstrated that the regulation of the oncomiRs (miR-17-92, miR-21) and tumor suppressor miRNAs (miR-144/451, miR-181a, miR-27, miR-28-5p, and miR-34a) could increase the sensitivity to R-CHOP chemotherapy components. These miRNAs show some characteristics as immunomodulators being able to regulate the expression of the inhibitory receptor programmed cell death-1 (PD-1) and its ligand PD-L1 [263]. Further Phase I clinical trials have already demonstrated the antioncogenic activity in B-NHL of three different miRNA mimics such as MRX34 (miR-34 mimic), mesomiR-1 (miR-16 mimic), and cobomarsen (anti-miR-155). These trials support the use of miRNAs as a therapeutic alternative [263].

Until now the therapy using miRNAs in ALCL is not available. But as mentioned before, the links of miRNAs and ALK in ALCL are expanding, identifying some of the target genes of the tumor suppressor miRNAs and also identifying the role of these miRNAs in the oncogenic mechanisms[264]. In this work, we have shown that miR-181a, miR-26a, and miR-146a mimics have an integral role in driving oncogenesis in ALCL mainly by regulating the tumor angiogenesis and using metabolic reprogramming., However, the future use of this miRNA, including clinical trials with miRNAs as therapeutic biomarkers and as directed therapies, remains to be explored [261,264].

5. Conclusions and perspectives.

In conclusion, this work shows potential roles of tumor suppressors (miR-181a, miR-26a, and miR-146a) miRNAs regulated by ALK and CEBPβ in ALCL.

First, we have shown that miR-181a and miR-26a mimics have an integral role in driving oncogenesis in ALCL mainly by regulating genes involved in tumor angiogenesis and metabolic reprogramming., However, the studies in miR-26a and miR181a are unripe, and a further comprehensive is needed to validate their target genes and their role by lymphomagenesis. Since *GLUT3* and *CD93* were postulated as their respective target genes, a deep analysis to investigate ALK dependence and the main role of these proteins in ALCL will be valuable.

On the other hand, miR-146a has been further explored showing its low expression in ALK+ ALCL and its ALK dependence, which results in the impairment of the inhibition of CD147, an oncogene involved in multiple pathways of cancer progression including invasion, angiogenesis, and metabolic enhancement. The mechanisms of CD147 have been explored *in vitro* and *in vivo*, demonstrating that lack of CD147 results in growth retardation, reduction of angiogenesis, matrix extracellular degradation, metabolic reprogramming, and mitochondrial function impairment. This upholds CD147 as vital protein to sustain the high energy demand of rapid cell proliferation, promoting lactate export and stresses *CD147* as a desirable target gene, highlighting the oncogenic axis pathway of ALK-miR-146a-CD147 in ALCL.

However, further experiment assays using miR-146a and CD147 as a biomarker to investigate its association to ALK in large cohorts of primary cases are still needed to investigate the biological variability of this pathway. The future use of this miRNA, including clinical trials with miRNAs as therapeutic biomarkers and as directed therapies, remains to be explored. It is necessary to investigate in vitro the possible effects of using miR146a inhibitors in ALK- ALCL cell lines or the use of commercially available anti-CD147 antibodies. Nevertheless, there are various limitations for the use of miRNAs to keep in mind, such as the safe delivery of miRNAs and the possible miRNA's side effects

6. Summary.

The miRNA signature including miR-146a, miR-181a, and miR-26a is differentially expressed in ALK+ and ALK-anaplastic large cell lymphoma (ALCL). In this study, the downstream target genes of these tumor suppressor miRNAs in ALK+ ALCL were investigated by transcriptome analysis, and *CD147, GLUT3*, and *CD93* were identified as their potential targets. Based on their differential expression in ALK+ ALCL compared with ALK- ALCL and normal T cells, these genes revealed to have a role in the pathogenesis of this lymphoma, by regulating metabolism and angiogenesis. In this thesis, we investigated the ALK-miR-146a-*CD147* target gene axis in more detail, confirming *CD147* as a direct target of miR-146. Further studies *in vitro* and *in vivo* in a xenograft mouse model confirmed that CD147 contributes to ALK+ ALCL survival and proliferation. Knockdown (KD) and knockout (KO) of *CD147* resulted in metabolic reprogramming, decreased glucose consumption, retardation of tumor growth, and mitochondrial damage. Metabolomics in CD147-silenced cell lines and tumors revealed a metabolic shift by reducing aerobic glycolysis and increasing basal respiration, the latter as a coupling mechanism due to mitochondrial damage. In summary, our results suggest that ALK-regulated tumor suppressors miRNAs play an important role in ALCL oncogenesis. In particular, miR-146a appears to be essential for the regulation of *CD147*, an oncogene that promotes altered metabolism to meet the energy requirements of ALCL cells for tumor growth. Moreover, the ALK-miR-146a-*CD147* pathway holds great potential as a novel target therapy in this lymphoma and requires further investigation.

6.1 German summary.

ALK+ und ALK- anaplastische großzellige Lymphome (ALCL) weisen unterschiedliche miRNA-Signaturen auf, einschließlich einer niedrigen Expression von miR-146a, miR-181a und miR-26a bei ALK+ALCL. In dieser Studie wurden die nachgeschalteten Zielgene dieser Tumorsuppressor-miRNAs in ALK+ ALCL durch Transkriptomanalyse untersucht, und *CD147, GLUT3* und *CD93* wurden als ihre potenziellen Ziele identifiziert. Ihre unterschiedliche Expression bei ALK+ ALCL im Vergleich zu ALK- ALCL und normalen T-Zellen deutet darauf hin, dass diese Gene eine Rolle bei der Pathogenese dieses Lymphoms spielen, insbesondere bei der Regulierung des Stoffwechsels und der Angiogenese. In dieser Arbeit haben wir die Zielgen-Achse ALK-miR-146a-CD147 genauer untersucht und CD147 als direktes Ziel der miR-146 bestätigt. Weitere Studien in vitro und in vivo in einem Xenograft-Mausmodell bestätigten, dass CD147 zum Überleben und zur Proliferation von ALK+ ALCL beiträgt. Knockdown (KD) und Knockout (KO) von *CD147* führten zu einer metabolischen Umprogrammierung, einem verringerten Glukoseverbrauch, einer Verlangsamung des Tumorwachstums und mitochondrialen Schäden. Metabolomics in Zelllinien und Tumoren, denen *CD147* fehlte, unterstützten diese Ergebnisse, indem sie eine Stoffwechselverschiebung durch verringerte aerobe Glykolyse und erhöhte Basalatmung aufzeigten, letztere als Kopplungsmechanismus aufgrund mitochondrialer Schäden. Zusammenfassend deuten unsere Ergebnisse darauf hin, dass ALK-regulierte Tumorsuppressoren miRNAs eine wichtige Rolle bei der ALCL-Onkogenese spielen. Insbesondere miR-146a erweist sich als entscheidend für die Regulierung von *CD147*, einem Onkogen, das einen veränderten Stoffwechsel fördert, um den Energiebedarf der ALCL-Zellen für das Tumorwachstum zu decken. Darüber hinaus birgt der ALK-miR-146a-CD147-Signalweg ein großes Potenzial als neuartiges Therapieziel bei diesem Lymphom und muss weiter untersucht werden.

7. References.

1. Swerdlow SH CE, Harris NL, Jaffe ES, Pileri SA, Stein H, Thiele J, Arber DA, Hasserjian RP, Le Beau MM, Orazi A, and Siebert R. . *WHO Classification of Tumours of Hematopoietic and Lymphoid Tissues.* 4 th ed. International Agency for Research on Cancer (IARC); 2017:585.
2. Burkhardt B, Zimmermann M, Oschlies I, et al. The impact of age and gender on biology, clinical features and treatment outcome of non-Hodgkin lymphoma in childhood and adolescence. *Br J Haematol*. Oct 2005;131(1):39-49. doi:10.1111/j.1365-2141.2005.05735.x
3. Stein H, Mason DY, Gerdes J, et al. The expression of the Hodgkin's disease associated antigen Ki-1 in reactive and neoplastic lymphoid tissue: evidence that Reed-Sternberg cells and histiocytic malignancies are derived from activated lymphoid cells. *Blood*. Oct 1985;66(4):848-58.
4. Morris SW, Kirstein MN, Valentine MB, et al. Fusion of a kinase gene, ALK, to a nucleolar protein gene, NPM, in non-Hodgkin's lymphoma. *Science*. Mar 04 1994;263(5151):1281-4.
5. Falini B, Pileri S, Zinzani PL, et al. ALK+ lymphoma: clinico-pathological findings and outcome. *Blood*. Apr 15 1999;93(8):2697-706.
6. Stein H, Foss HD, Durkop H, et al. CD30(+) anaplastic large cell lymphoma: a review of its histopathologic, genetic, and clinical features. *Blood*. Dec 1 2000;96(12):3681-95.
7. Filippa DA, Ladanyi M, Wollner N, et al. CD30 (Ki-1)-positive malignant lymphomas: clinical, immunophenotypic, histologic, and genetic characteristics and differences with Hodgkin's disease. *Blood*. Apr 1 1996;87(7):2905-17.
8. Kadin ME, Carpenter C. Systemic and primary cutaneous anaplastic large cell lymphomas. *Semin Hematol*. Jul 2003;40(3):244-56.
9. Savage KJ, Harris NL, Vose JM, et al. ALK- anaplastic large-cell lymphoma is clinically and immunophenotypically different from both ALK+ ALCL and peripheral T-cell lymphoma, not otherwise specified: report from the International Peripheral T-Cell Lymphoma Project. *Blood*. Jun 15 2008;111(12):5496-504. doi:10.1182/blood-2008-01-134270
10. Jaffe ES. Anaplastic large cell lymphoma: the shifting sands of diagnostic hematopathology. *Mod Pathol*. Mar 2001;14(3):219-28. doi:10.1038/modpathol.3880289
11. Delsol G, Lamant L, Mariame B, et al. A new subtype of large B-cell lymphoma expressing the ALK kinase and lacking the 2; 5 translocation. *Blood*. Mar 1 1997;89(5):1483-90.
12. Montes-Mojarro IA, Steinhilber J, Bonzheim I, Quintanilla-Martinez L, Fend F. The Pathological Spectrum of Systemic Anaplastic Large Cell Lymphoma (ALCL). *Cancers (Basel)*. Apr 4 2018;10(4)doi:10.3390/cancers10040107
13. Gruss HJ, Dower SK. Tumor necrosis factor ligand superfamily: involvement in the pathology of malignant lymphomas. *Blood*. Jun 15 1995;85(12):3378-404.
14. Bonzheim I, Geissinger E, Roth S, et al. Anaplastic large cell lymphomas lack the expression of T-cell receptor molecules or molecules of proximal T-cell receptor signaling. *Blood*. Nov 15 2004;104(10):3358-60. doi:10.1182/blood-2004-03-1037
15. Ambrogio C, Martinengo C, Voena C, et al. NPM-ALK oncogenic tyrosine kinase controls T-cell identity by transcriptional regulation and epigenetic silencing in lymphoma cells. *Cancer Res*. Nov 15 2009;69(22):8611-9. doi:10.1158/0008-5472.CAN-09-2655
16. Pulford K, Lamant L, Morris SW, et al. Detection of anaplastic lymphoma kinase (ALK) and nucleolar protein nucleophosmin (NPM)-ALK proteins in normal and

neoplastic cells with the monoclonal antibody ALK1. *Blood*. Feb 15 1997;89(4):1394-404.
17. Lamant L, Gascoyne RD, Duplantier MM, et al. Non-muscle myosin heavy chain (MYH9): a new partner fused to ALK in anaplastic large cell lymphoma. *Genes Chromosomes Cancer*. Aug 2003;37(4):427-32. doi:10.1002/gcc.10232
18. Touriol C, Greenland C, Lamant L, et al. Further demonstration of the diversity of chromosomal changes involving 2p23 in ALK-positive lymphoma: 2 cases expressing ALK kinase fused to CLTCL (clathrin chain polypeptide-like). *Blood*. May 15 2000;95(10):3204-7.
19. Tort F, Pinyol M, Pulford K, et al. Molecular characterization of a new ALK translocation involving moesin (MSN-ALK) in anaplastic large cell lymphoma. *Lab Invest*. Mar 2001;81(3):419-26. doi:10.1038/labinvest.3780249
20. Falini B, Pulford K, Pucciarini A, et al. Lymphomas expressing ALK fusion protein(s) other than NPM-ALK. *Blood*. Nov 15 1999;94(10):3509-15.
21. Cools J, Wlodarska I, Somers R, et al. Identification of novel fusion partners of ALK, the anaplastic lymphoma kinase, in anaplastic large-cell lymphoma and inflammatory myofibroblastic tumor. *Genes Chromosomes Cancer*. Aug 2002;34(4):354-62. doi:10.1002/gcc.10033
22. Feldman AL, Vasmatzis G, Asmann YW, et al. Novel TRAF1-ALK fusion identified by deep RNA sequencing of anaplastic large cell lymphoma. *Genes Chromosomes Cancer*. Nov 2013;52(11):1097-102. doi:10.1002/gcc.22104
23. Hernandez L, Pinyol M, Hernandez S, et al. TRK-fused gene (TFG) is a new partner of ALK in anaplastic large cell lymphoma producing two structurally different TFG-ALK translocations. *Blood*. Nov 1 1999;94(9):3265-8.
24. Lamant L, Dastugue N, Pulford K, Delsol G, Mariame B. A new fusion gene TPM3-ALK in anaplastic large cell lymphoma created by a (1;2)(q25;p23) translocation. *Blood*. May 1 1999;93(9):3088-95.
25. Mason DY, Pulford KA, Bischof D, et al. Nucleolar localization of the nucleophosmin-anaplastic lymphoma kinase is not required for malignant transformation. *Cancer Res*. Mar 1 1998;58(5):1057-62.
26. Rosenwald A, Ott G, Pulford K, et al. t(1;2)(q21;p23) and t(2;3)(p23;q21): two novel variant translocations of the t(2;5)(p23;q35) in anaplastic large cell lymphoma. *Blood*. Jul 1 1999;94(1):362-4.
27. Trinei M, Lanfrancone L, Campo E, et al. A new variant anaplastic lymphoma kinase (ALK)-fusion protein (ATIC-ALK) in a case of ALK-positive anaplastic large cell lymphoma. *Cancer Res*. Feb 15 2000;60(4):793-8.
28. Wlodarska I, De Wolf-Peeters C, Falini B, et al. The cryptic inv(2)(p23q35) defines a new molecular genetic subtype of ALK-positive anaplastic large-cell lymphoma. *Blood*. Oct 15 1998;92(8):2688-95.
29. Abate F, Todaro M, van der Krogt JA, et al. A novel patient-derived tumorgraft model with TRAF1-ALK anaplastic large-cell lymphoma translocation. *Leukemia*. Jun 2015;29(6):1390-401. doi:10.1038/leu.2014.347
30. Abouyabis AN, Shenoy PJ, Lechowicz MJ, Flowers CR. Incidence and outcomes of the peripheral T-cell lymphoma subtypes in the United States. *Leuk Lymphoma*. Nov 2008;49(11):2099-107. doi:10.1080/10428190802455867
31. Honorat JF, Ragab A, Lamant L, Delsol G, Ragab-Thomas J. SHP1 tyrosine phosphatase negatively regulates NPM-ALK tyrosine kinase signaling. *Blood*. May 15 2006;107(10):4130-8. doi:10.1182/blood-2005-06-2421
32. Lamant L, de Reynies A, Duplantier MM, et al. Gene-expression profiling of systemic anaplastic large-cell lymphoma reveals differences based on ALK status and two distinct morphologic ALK+ subtypes. *Blood*. Mar 1 2007;109(5):2156-64. doi:10.1182/blood-2006-06-028969

33. Quintanilla-Martinez L, Pittaluga S, Miething C, et al. NPM-ALK-dependent expression of the transcription factor CCAAT/enhancer binding protein beta in ALK-positive anaplastic large cell lymphoma. *Blood*. Sep 15 2006;108(6):2029-36. doi:blood-2005-10-014258 [pii] 10.1182/blood-2005-10-014258
34. Schmidt J, Bonzheim I, Steinhilber J, et al. EMMPRIN (CD147) is induced by C/EBPbeta and is differentially expressed in ALK+ and ALK- anaplastic large-cell lymphoma. *Lab Invest*. Sep 2017;97(9):1095-1102. doi:10.1038/labinvest.2017.54
35. He JH, Liang XM, Hou JH, Huan YL, Wu QL, Xiao YB. [Study of CD44v6 protein expression in intraductal papilloma and its malignant transformation of breast]. *Ai Zheng*. Jun 2002;21(6):615-8.
36. Liang X, Golitz LE, Smoller BR, et al. Association of expression of CD44v6 with systemic anaplastic large cell lymphoma: comparison with primary cutaneous anaplastic large cell lymphoma. *Am J Clin Pathol*. Feb 2002;117(2):276-82.
37. Pulford K, Lamant L, Espinos E, et al. The emerging normal and disease-related roles of anaplastic lymphoma kinase. *Cell Mol Life Sci*. Dec 2004;61(23):2939-53. doi:10.1007/s00018-004-4275-9
38. Pulford K, Morris SW, Turturro F. Anaplastic lymphoma kinase proteins in growth control and cancer. *J Cell Physiol*. Jun 2004;199(3):330-58. doi:10.1002/jcp.10472
39. Fujimoto J, Shiota M, Iwahara T, et al. Characterization of the transforming activity of p80, a hyperphosphorylated protein in a Ki-1 lymphoma cell line with chromosomal translocation t(2;5). *Proc Natl Acad Sci U S A*. Apr 30 1996;93(9):4181-6.
40. Bischof D, Pulford K, Mason DY, Morris SW. Role of the nucleophosmin (NPM) portion of the non-Hodgkin's lymphoma-associated NPM-anaplastic lymphoma kinase fusion protein in oncogenesis. *Mol Cell Biol*. Apr 1997;17(4):2312-25.
41. Zamo A, Chiarle R, Piva R, et al. Anaplastic lymphoma kinase (ALK) activates Stat3 and protects hematopoietic cells from cell death. *Oncogene*. Feb 7 2002;21(7):1038-47. doi:10.1038/sj.onc.1205152
42. Anastasov N, Bonzheim I, Rudelius M, et al. C/EBPbeta expression in ALK-positive anaplastic large cell lymphomas is required for cell proliferation and is induced by the STAT3 signaling pathway. *Haematologica*. May 2010;95(5):760-7. doi:10.3324/haematol.2009.014050
43. Slupianek A, Nieborowska-Skorska M, Hoser G, et al. Role of phosphatidylinositol 3-kinase-Akt pathway in nucleophosmin/anaplastic lymphoma kinase-mediated lymphomagenesis. *Cancer Res*. Mar 1 2001;61(5):2194-9.
44. Bai RY, Dieter P, Peschel C, Morris SW, Duyster J. Nucleophosmin-anaplastic lymphoma kinase of large-cell anaplastic lymphoma is a constitutively active tyrosine kinase that utilizes phospholipase C-gamma to mediate its mitogenicity. *Mol Cell Biol*. Dec 1998;18(12):6951-61.
45. Werner MT, Zhao C, Zhang Q, Wasik MA. Nucleophosmin-anaplastic lymphoma kinase: the ultimate oncogene and therapeutic target. *Blood*. Feb 16 2017;129(7):823-831. doi:10.1182/blood-2016-05-717793
46. Marzec M, Halasa K, Liu X, et al. Malignant transformation of CD4+ T lymphocytes mediated by oncogenic kinase NPM/ALK recapitulates IL-2-induced cell signaling and gene expression reprogramming. *J Immunol*. Dec 15 2013;191(12):6200-7. doi:10.4049/jimmunol.1300744
47. Chiarle R, Simmons WJ, Cai H, et al. Stat3 is required for ALK-mediated lymphomagenesis and provides a possible therapeutic target. *Nat Med*. Jun 2005;11(6):623-9. doi:10.1038/nm1249
48. Tolomeo M, Grimaudo S. The "Janus" Role of C/EBPs Family Members in Cancer Progression. *International journal of molecular sciences*. Jun 17 2020;21(12)doi:10.3390/ijms21124308

49. Huber R, Pietsch D, Panterodt T, Brand K. Regulation of C/EBPbeta and resulting functions in cells of the monocytic lineage. *Cell Signal*. Jun 2012;24(6):1287-96. doi:10.1016/j.cellsig.2012.02.007
50. Davydov IV, Krammer PH, Li-Weber M. Nuclear factor-IL6 activates the human IL-4 promoter in T cells. *J Immunol*. Dec 1 1995;155(11):5273-9.
51. Greenwel P, Tanaka S, Penkov D, et al. Tumor necrosis factor alpha inhibits type I collagen synthesis through repressive CCAAT/enhancer-binding proteins. *Mol Cell Biol*. Feb 2000;20(3):912-8. doi:10.1128/mcb.20.3.912-918.2000
52. van Dijk TB, Baltus B, Raaijmakers JA, Lammers JW, Koenderman L, de Groot RP. A composite C/EBP binding site is essential for the activity of the promoter of the IL-3/IL-5/granulocyte-macrophage colony-stimulating factor receptor beta c gene. *J Immunol*. Sep 1 1999;163(5):2674-80.
53. Xi S, Yang M, Tao Y, et al. Cigarette smoke induces C/EBP-beta-mediated activation of miR-31 in normal human respiratory epithelia and lung cancer cells. *PLoS One*. Oct 29 2010;5(10):e13764. doi:10.1371/journal.pone.0013764
54. Eyholzer M, Schmid S, Schardt JA, Haefliger S, Mueller BU, Pabst T. Complexity of miR-223 regulation by CEBPA in human AML. *Leukemia Research*. 2010/05/01/ 2010;34(5):672-676. doi:https://doi.org/10.1016/j.leukres.2009.11.019
55. Xiao Y, Su C, Deng T. miR-223 decreases cell proliferation and enhances cell apoptosis in acute myeloid leukemia via targeting FBXW7. *Oncol Lett*. 2016;12(5):3531-3536. doi:10.3892/ol.2016.5115
56. Sun D, Wang C, Long S, et al. C/EBP-β-activated microRNA-223 promotes tumour growth through targeting RASA1 in human colorectal cancer. *British Journal of Cancer*. 2015/04/01 2015;112(9):1491-1500. doi:10.1038/bjc.2015.107
57. Ponomarev ED, Veremeyko T, Barteneva N, Krichevsky AM, Weiner HL. MicroRNA-124 promotes microglia quiescence and suppresses EAE by deactivating macrophages via the C/EBP-α–PU.1 pathway. *Nature Medicine*. 2011/01/01 2011;17(1):64-70. doi:10.1038/nm.2266
58. Lee RC, Feinbaum RL, Ambros V. The C. elegans heterochronic gene lin-4 encodes small RNAs with antisense complementarity to lin-14. *Cell*. Dec 3 1993;75(5):843-54. doi:10.1016/0092-8674(93)90529-y
59. Wightman B, Ha I, Ruvkun G. Posttranscriptional regulation of the heterochronic gene lin-14 by lin-4 mediates temporal pattern formation in C. elegans. *Cell*. Dec 3 1993;75(5):855-62. doi:10.1016/0092-8674(93)90530-4
60. Lewis BP, Shih IH, Jones-Rhoades MW, Bartel DP, Burge CB. Prediction of mammalian microRNA targets. *Cell*. Dec 26 2003;115(7):787-98.
61. He L, Hannon GJ. Micrornas: Small RNAs with a big role in gene regulation. *Nat Rev Genet*. Jul 2004;5(7):522-531. doi:10.1038/nrg1379
62. Esquela-Kerscher A, Slack FJ. Oncomirs - microRNAs with a role in cancer. *Nat Rev Cancer*. Apr 2006;6(4):259-69. doi:10.1038/nrc1840
63. Vasilatou D, Papageorgiou S, Pappa V, Papageorgiou E, Dervenoulas J. The role of microRNAs in normal and malignant hematopoiesis. *European journal of haematology*. Jan 1 2010;84(1):1-16. doi:10.1111/j.1600-0609.2009.01348.x
64. Parpart S, Wang XW. microRNA Regulation and Its Consequences in Cancer. *Current pathobiology reports*. Mar 2013;1(1):71-79. doi:10.1007/s40139-012-0002-7
65. Farazi TA, Spitzer JI, Morozov P, Tuschl T. miRNAs in human cancer. *J Pathol*. Jan 2011;223(2):102-15. doi:10.1002/path.2806
66. Lai EC. microRNAs: runts of the genome assert themselves. *Curr Biol*. Dec 02 2003;13(23):R925-36.
67. Peng RJ, Han BW, Cai QQ, et al. Genomic and transcriptomic landscapes of Epstein-Barr virus in extranodal natural killer T-cell lymphoma. *Leukemia*. Jun 2019;33(6):1451-1462. doi:10.1038/s41375-018-0324-5

68. Baumjohann D, Ansel KM. MicroRNA-mediated regulation of T helper cell differentiation and plasticity. *Nature Reviews Immunology*. 2013/09/01 2013;13(9):666-678. doi:10.1038/nri3494
69. Winter J, Jung S, Keller S, Gregory RI, Diederichs S. Many roads to maturity: microRNA biogenesis pathways and their regulation. *Nature Cell Biology*. 2009/03/01 2009;11(3):228-234. doi:10.1038/ncb0309-228
70. Davis-Dusenbery BN, Hata A. MicroRNA in Cancer: The Involvement of Aberrant MicroRNA Biogenesis Regulatory Pathways. *Genes & cancer*. Nov 2010;1(11):1100-14. doi:10.1177/1947601910396213
71. De Tullio G, De Fazio V, Sgherza N, et al. Challenges and Opportunities of MicroRNAs in Lymphomas. *Molecules*. 2014;19(9):14723-14781. doi:10.3390/molecules190914723
72. Lawrie CH. MicroRNAs in hematological malignancies. *Blood reviews*. May 2013;27(3):143-54. doi:10.1016/j.blre.2013.04.002
73. Calin GA, Dumitru CD, Shimizu M, et al. Frequent deletions and down-regulation of micro- RNA genes miR15 and miR16 at 13q14 in chronic lymphocytic leukemia. *Proc Natl Acad Sci U S A*. Nov 26 2002;99(24):15524-9. doi:10.1073/pnas.242606799
74. Pekarsky Y, Balatti V, Croce CM. BCL2 and miR-15/16: from gene discovery to treatment. *Cell Death Differ*. 2018;25(1):21-26. doi:10.1038/cdd.2017.159
75. Costinean S, Sandhu SK, Pedersen IM, et al. Src homology 2 domain-containing inositol-5-phosphatase and CCAAT enhancer-binding protein beta are targeted by miR-155 in B cells of Emicro-MiR-155 transgenic mice. *Blood*. Aug 13 2009;114(7):1374-82. doi:10.1182/blood-2009-05-220814
76. Laginestra MA, Piccaluga PP, Fuligni F, et al. Pathogenetic and diagnostic significance of microRNA deregulation in peripheral T-cell lymphoma not otherwise specified. *Blood Cancer Journal*. 2014/11/01 2014;4(11):e259-e259. doi:10.1038/bcj.2014.78
77. Liu C, Iqbal J, Teruya-Feldstein J, et al. MicroRNA expression profiling identifies molecular signatures associated with anaplastic large cell lymphoma. *Blood*. Sep 19 2013;122(12):2083-92. doi:10.1182/blood-2012-08-447375
78. Merkel O, Hamacher F, Laimer D, et al. Identification of differential and functionally active miRNAs in both anaplastic lymphoma kinase (ALK)+ and ALK- anaplastic large-cell lymphoma. *Proc Natl Acad Sci U S A*. Sep 14 2010;107(37):16228-33. doi:10.1073/pnas.1009719107
79. Steinhilber J, Bonin M, Walter M, Fend F, Bonzheim I, Quintanilla-Martinez L. Next-generation sequencing identifies deregulation of microRNAs involved in both innate and adaptive immune response in ALK+ ALCL. *PLoS One*. 2015;10(2):e0117780. doi:10.1371/journal.pone.0117780
80. Mehrotra M, Medeiros LJ, Luthra R, et al. Identification of putative pathogenic microRNA and its downstream targets in anaplastic lymphoma kinase-negative anaplastic large cell lymphoma. *Human pathology*. Oct 2014;45(10):1995-2005. doi:10.1016/j.humpath.2014.06.012
81. Matsuyama H, Suzuki HI, Nishimori H, et al. miR-135b mediates NPM-ALK-driven oncogenicity and renders IL-17-producing immunophenotype to anaplastic large cell lymphoma. *Blood*. Dec 22 2011;118(26):6881-92. doi:10.1182/blood-2011-05-354654
82. Desjobert C, Renalier MH, Bergalet J, et al. MiR-29a down-regulation in ALK-positive anaplastic large cell lymphomas contributes to apoptosis blockade through MCL-1 overexpression. *Blood*. Jun 16 2011;117(24):6627-37. doi:10.1182/blood-2010-09-301994
83. Mehrotra M, Medeiros LJ, Luthra R, et al. Identification of putative pathogenic microRNA and its downstream targets in anaplastic lymphoma kinase–negative

anaplastic large cell lymphoma. *Human pathology*. 2014/10/01/ 2014;45(10):1995-2005. doi:https://doi.org/10.1016/j.humpath.2014.06.012
84. Ye Z, Li G, Kim C, et al. Regulation of miR-181a expression in T cell aging. *Nature Communications*. 2018/08/03 2018;9(1):3060. doi:10.1038/s41467-018-05552-3
85. Ji J, Yamashita T, Budhu A, et al. Identification of microRNA-181 by genome-wide screening as a critical player in EpCAM-positive hepatic cancer stem cells. *Hepatology*. Aug 2009;50(2):472-80. doi:10.1002/hep.22989
86. Li QJ, Chau J, Ebert PJ, et al. miR-181a is an intrinsic modulator of T cell sensitivity and selection. *Cell*. Apr 06 2007;129(1):147-61. doi:10.1016/j.cell.2007.03.008
87. Schaffert SA, Loh C, Wang S, et al. mir-181a-1/b-1 Modulates Tolerance through Opposing Activities in Selection and Peripheral T Cell Function. *J Immunol*. Aug 15 2015;195(4):1470-9. doi:10.4049/jimmunol.1401587
88. Kozloski GA, Jiang X, Bhatt S, et al. miR-181a negatively regulates NF-κB signaling and affects activated B-cell–like diffuse large B-cell lymphoma pathogenesis. *Blood*. 2016;127(23):2856-2866. doi:10.1182/blood-2015-11-680462
89. Ji J, Yamashita T, Budhu A, et al. Identification of microRNA-181 by genome-wide screening as a critical player in EpCAM–positive hepatic cancer stem cells. *Hepatology*. 2009;50(2):472-480. doi:https://doi.org/10.1002/hep.22989
90. Pichiorri F, Suh S-S, Ladetto M, et al. MicroRNAs regulate critical genes associated with multiple myeloma pathogenesis. *Proceedings of the National Academy of Sciences*. 2008;105(35):12885-12890. doi:10.1073/pnas.0806202105
91. Pons A, Nomdedeu B, Navarro A, et al. Hematopoiesis-related microRNA expression in myelodysplastic syndromes. *Leukemia & Lymphoma*. 2009/11/01 2009;50(11):1854-1859. doi:10.3109/10428190903147645
92. Koolivand M, Moein S, MalekZadeh K. The relationship of miR-181a expression level and AML: A systematic review protocol. *International Journal of Surgery Protocols*. 2019/01/01/ 2019;13:1-4. doi:https://doi.org/10.1016/j.isjp.2018.12.001
93. Gao J, Liu Q-G. The role of miR-26 in tumors and normal tissues (Review). *Oncol Lett*. 2011;2(6):1019-1023. doi:10.3892/ol.2011.413
94. Huse JT, Brennan C, Hambardzumyan D, et al. The PTEN-regulating microRNA miR-26a is amplified in high-grade glioma and facilitates gliomagenesis in vivo. *Genes & development*. Jun 1 2009;23(11):1327-37. doi:10.1101/gad.1777409
95. Gao J, Li L, Wu M, et al. MiR-26a inhibits proliferation and migration of breast cancer through repression of MCL-1. *PLoS One*. 2013;8(6):e65138. doi:10.1371/journal.pone.0065138
96. Liu B, Wu X, Liu B, et al. MiR-26a enhances metastasis potential of lung cancer cells via AKT pathway by targeting PTEN. *Biochimica et Biophysica Acta (BBA) - Molecular Basis of Disease*. 2012/11/01/ 2012;1822(11):1692-1704. doi:https://doi.org/10.1016/j.bbadis.2012.07.019
97. Icli B, Dorbala P, Feinberg MW. An emerging role for the miR-26 family in cardiovascular disease. *Trends in cardiovascular medicine*. Aug 2014;24(6):241-8. doi:10.1016/j.tcm.2014.06.003
98. Wang Z, Xie Q, Yu Z, et al. A regulatory loop containing miR-26a, GSK3β and C/EBPα regulates the osteogenesis of human adipose-derived mesenchymal stem cells. *Scientific reports*. Oct 15 2015;5:15280. doi:10.1038/srep15280
99. Zhao J, Hu Y, Liu H, et al. miR-26a as a novel potential therapeutic via inhibit CD38 translation and may overcome datatumumab resistance in multiple myeloma(MM). *The Journal of Immunology*. 2020;204(1 Supplement):91.10-91.10.
100. Dong J, Sui L, Wang Q, Chen M, Sun H. MicroRNA-26a inhibits cell proliferation and invasion of cervical cancer cells by targeting protein tyrosine phosphatase type IVA 1. *Mol Med Rep*. Sep 2014;10(3):1426-32. doi:10.3892/mmr.2014.2335

101. Zhang R, Tian A, Wang J, Shen X, Qi G, Tang Y. miR26a modulates Th17/T reg balance in the EAE model of multiple sclerosis by targeting IL6. *Neuromolecular Med*. Mar 2015;17(1):24-34. doi:10.1007/s12017-014-8335-5
102. Labbaye C, Testa U. The emerging role of MIR-146A in the control of hematopoiesis, immune function and cancer. *Journal of Hematology & Oncology*. 2012/03/27 2012;5(1):13. doi:10.1186/1756-8722-5-13
103. Iacona JR, Lutz CS. miR-146a-5p: Expression, regulation, and functions in cancer. *WIREs RNA*. 2019;10(4):e1533. doi:https://doi.org/10.1002/wrna.1533
104. Taganov KD, Boldin MP, Chang KJ, Baltimore D. NF-kappaB-dependent induction of microRNA miR-146, an inhibitor targeted to signaling proteins of innate immune responses. *Proc Natl Acad Sci U S A*. Aug 15 2006;103(33):12481-6. doi:0605298103 [pii] 10.1073/pnas.0605298103
105. Thai TH, Calado DP, Casola S, et al. Regulation of the germinal center response by microRNA-155. *Science*. Apr 27 2007;316(5824):604-8. doi:316/5824/604 [pii 10.1126/science.1141229
106. Yanaihara N, Caplen N, Bowman E, et al. Unique microRNA molecular profiles in lung cancer diagnosis and prognosis. *Cancer Cell*. Mar 2006;9(3):189-98. doi:S1535-6108(06)00033-X [pii] 10.1016/j.ccr.2006.01.025
107. Boldin MP, Taganov KD, Rao DS, et al. miR-146a is a significant brake on autoimmunity, myeloproliferation, and cancer in mice. *The Journal of experimental medicine*. Jun 6 2011;208(6):1189-201. doi:10.1084/jem.20101823
108. Zhao JL, Rao DS, Boldin MP, Taganov KD, O'Connell RM, Baltimore D. NF-kappaB dysregulation in microRNA-146a-deficient mice drives the development of myeloid malignancies. *Proc Natl Acad Sci U S A*. May 31 2011;108(22):9184-9. doi:10.1073/pnas.1105398108
109. Paik JH, Jang JY, Jeon YK, et al. MicroRNA-146a downregulates NFkappaB activity via targeting TRAF6 and functions as a tumor suppressor having strong prognostic implications in NK/T cell lymphoma. *Clin Cancer Res*. Jul 15 2011;17(14):4761-71. doi:10.1158/1078-0432.CCR-11-0494
110. Steinhilber J. *Charakterisierung der miRNA-Expression im großzellig anaplastischen T-Zell-Lymphom*. Eberhard Karls Universität Tübingen; 2014.
111. Gersmann A-K. *Untersuchung der direkten Regulation der miR-29c- und miR-146a-abhängig exprimierten Zielgene mittels Reportergensassay im ALK-positiven ALCL*. Eberhard Karls Universität Tübingen; 2017.
112. Zhang Z, Zhang Y, Sun XX, Ma X, Chen ZN. microRNA-146a inhibits cancer metastasis by downregulating VEGF through dual pathways in hepatocellular carcinoma. *Molecular cancer*. 2015;14:5. doi:10.1186/1476-4598-14-5
113. Kaname T, Miyauchi T, Kuwano A, Matsuda Y, Muramatsu T, Kajii T. Mapping basigin (BSG), a member of the immunoglobulin superfamily, to 19p13.3. *Cytogenetics and cell genetics*. 1993;64(3-4):195-7. doi:10.1159/000133573
114. Belton RJ, Jr., Chen L, Mesquita FS, Nowak RA. Basigin-2 is a cell surface receptor for soluble basigin ligand. *The Journal of biological chemistry*. Jun 27 2008;283(26):17805-14. doi:10.1074/jbc.M801876200
115. Landras A, Reger de Moura C, Jouenne F, Lebbe C, Menashi S, Mourah S. CD147 Is a Promising Target of Tumor Progression and a Prognostic Biomarker. *Cancers*. 2019;11(11):1803.
116. Weidle UH, Scheuer W, Eggle D, Klostermann S, Stockinger H. Cancer-related issues of CD147. *Cancer Genomics Proteomics*. May-Jun 2010;7(3):157-69.
117. Yan L, Zucker S, Toole BP. Roles of the multifunctional glycoprotein, emmprin (basigin; CD147), in tumour progression. *Thrombosis and haemostasis*. Feb 2005;93(2):199-204. doi:10.1160/th04-08-0536
118. Kanekura T, Chen X, Kanzaki T. Basigin (CD147) is expressed on melanoma cells and induces tumor cell invasion by stimulating production of matrix

metalloproteinases by fibroblasts. *International journal of cancer*. Jun 1 2002;99(4):520-8. doi:10.1002/ijc.10390
119. Rucci N, Millimaggi D, Mari M, et al. Receptor activator of NF-kappaB ligand enhances breast cancer-induced osteolytic lesions through upregulation of extracellular matrix metalloproteinase inducer/CD147. *Cancer Res*. Aug 1 2010;70(15):6150-60. doi:10.1158/0008-5472.Can-09-2758
120. Quemener C, Gabison EE, Naïmi B, et al. Extracellular matrix metalloproteinase inducer up-regulates the urokinase-type plasminogen activator system promoting tumor cell invasion. *Cancer Res*. Jan 1 2007;67(1):9-15. doi:10.1158/0008-5472.Can-06-2448
121. Menashi S, Serova M, Ma L, Vignot S, Mourah S, Calvo F. Regulation of extracellular matrix metalloproteinase inducer and matrix metalloproteinase expression by amphiregulin in transformed human breast epithelial cells. *Cancer Res*. Nov 15 2003;63(22):7575-80.
122. Yu B, Zhang Y, Wu K, et al. CD147 promotes progression of head and neck squamous cell carcinoma via NF-kappa B signaling. *Journal of cellular and molecular medicine*. Feb 2019;23(2):954-966. doi:10.1111/jcmm.13996
123. Tang Y, Nakada MT, Kesavan P, et al. Extracellular matrix metalloproteinase inducer stimulates tumor angiogenesis by elevating vascular endothelial cell growth factor and matrix metalloproteinases. *Cancer Res*. Apr 15 2005;65(8):3193-9. doi:65/8/3193 [pii] 10.1158/0008-5472.CAN-04-3605
124. Felmlee DJ, Baumert TF. CD147 handles lipid: a new role for anti-cancer target. *Translational Cancer Research*. 2016;5(3):238-240.
125. Xin X, Zeng X, Gu H, et al. CD147/EMMPRIN overexpression and prognosis in cancer: A systematic review and meta-analysis. *Scientific reports*. 2016/09/09 2016;6(1):32804. doi:10.1038/srep32804
126. Huang Q, Li J, Xing J, et al. CD147 promotes reprogramming of glucose metabolism and cell proliferation in HCC cells by inhibiting the p53-dependent signaling pathway. *Journal of hepatology*. Oct 2014;61(4):859-66. doi:10.1016/j.jhep.2014.04.035
127. Baba M, Inoue M, Itoh K, Nishizawa Y. Blocking CD147 induces cell death in cancer cells through impairment of glycolytic energy metabolism. *Biochemical and biophysical research communications*. Sep 12 2008;374(1):111-6. doi:10.1016/j.bbrc.2008.06.122
128. Li X, Xu W. CD147-mediated reprogrammed glycolytic metabolism potentially induces immune escape in the tumor microenvironment (Review). *Oncology reports*. May 2019;41(5):2945-2956. doi:10.3892/or.2019.7041
129. ten Berge RL, de Bruin PC, Oudejans JJ, Ossenkoppele GJ, van der Valk P, Meijer CJ. ALK-negative anaplastic large-cell lymphoma demonstrates similar poor prognosis to peripheral T-cell lymphoma, unspecified. *Histopathology*. Nov 2003;43(5):462-9.
130. Parrilla Castellar ER, Jaffe ES, Said JW, et al. ALK-negative anaplastic large cell lymphoma is a genetically heterogeneous disease with widely disparate clinical outcomes. *Blood*. Aug 28 2014;124(9):1473-80. doi:10.1182/blood-2014-04-571091
131. Feldman AL, Dogan A, Smith DI, et al. Discovery of recurrent t(6;7)(p25.3;q32.3) translocations in ALK-negative anaplastic large cell lymphomas by massively parallel genomic sequencing. *Blood*. Jan 20 2011;117(3):915-9. doi:10.1182/blood-2010-08-303305
132. Vasmatzis G, Johnson SH, Knudson RA, et al. Genome-wide analysis reveals recurrent structural abnormalities of TP63 and other p53-related genes in peripheral T-cell lymphomas. *Blood*. Sep 13 2012;120(11):2280-9. doi:10.1182/blood-2012-03-419937

133. A predictive model for aggressive non-Hodgkin's lymphoma. *N Engl J Med*. Sep 30 1993;329(14):987-94. doi:10.1056/nejm199309303291402
134. Cederleuf H, Bjerregård Pedersen M, Jerkeman M, Relander T, d'Amore F, Ellin F. The addition of etoposide to CHOP is associated with improved outcome in ALK+ adult anaplastic large cell lymphoma: A Nordic Lymphoma Group study. *Br J Haematol*. Sep 2017;178(5):739-746. doi:10.1111/bjh.14740
135. Schmitz N, Trümper L, Ziepert M, et al. Treatment and prognosis of mature T-cell and NK-cell lymphoma: an analysis of patients with T-cell lymphoma treated in studies of the German High-Grade Non-Hodgkin Lymphoma Study Group. *Blood*. Nov 4 2010;116(18):3418-25. doi:10.1182/blood-2010-02-270785
136. Abramson JS, Feldman T, Kroll-Desrosiers AR, et al. Peripheral T-cell lymphomas in a large US multicenter cohort: prognostication in the modern era including impact of frontline therapy. *Ann Oncol*. Nov 2014;25(11):2211-2217. doi:10.1093/annonc/mdu443
137. Fanale MA, Horwitz SM, Forero-Torres A, et al. Five-year outcomes for frontline brentuximab vedotin with CHP for CD30-expressing peripheral T-cell lymphomas. *Blood*. 2018;131(19):2120-2124. doi:10.1182/blood-2017-12-821009
138. Rodriguez J, Munsell M, Yazji S, et al. Impact of high-dose chemotherapy on peripheral T-cell lymphomas. *J Clin Oncol*. Sep 1 2001;19(17):3766-70. doi:10.1200/jco.2001.19.17.3766
139. Younes A, Bartlett NL, Leonard JP, et al. Brentuximab vedotin (SGN-35) for relapsed CD30-positive lymphomas. *N Engl J Med*. Nov 4 2010;363(19):1812-21. doi:10.1056/NEJMoa1002965
140. Pro B, Advani R, Brice P, et al. Brentuximab vedotin (SGN-35) in patients with relapsed or refractory systemic anaplastic large-cell lymphoma: results of a phase II study. *J Clin Oncol*. Jun 20 2012;30(18):2190-6. doi:10.1200/jco.2011.38.0402
141. Mossé YP, Lim MS, Voss SD, et al. Safety and activity of crizotinib for paediatric patients with refractory solid tumours or anaplastic large-cell lymphoma: a Children's Oncology Group phase 1 consortium study. *The Lancet Oncology*. 2013/05/01/ 2013;14(6):472-480. doi:https://doi.org/10.1016/S1470-2045(13)70095-0
142. Iwahara T, Fujimoto J, Wen D, et al. Molecular characterization of ALK, a receptor tyrosine kinase expressed specifically in the nervous system. *Oncogene*. Jan 30 1997;14(4):439-49. doi:10.1038/sj.onc.1200849
143. Chiarle R, Voena C, Ambrogio C, Piva R, Inghirami G. The anaplastic lymphoma kinase in the pathogenesis of cancer. *Nat Rev Cancer*. Jan 2008;8(1):11-23. doi:nrc2291 [pii] 10.1038/nrc2291
144. Bai RY, Ouyang T, Miething C, Morris SW, Peschel C, Duyster J. Nucleophosmin-anaplastic lymphoma kinase associated with anaplastic large-cell lymphoma activates the phosphatidylinositol 3-kinase/Akt antiapoptotic signaling pathway. *Blood*. Dec 15 2000;96(13):4319-27.
145. Chiarle R, Gong JZ, Guasparri I, et al. NPM-ALK transgenic mice spontaneously develop T-cell lymphomas and plasma cell tumors. *Blood*. Mar 1 2003;101(5):1919-27. doi:10.1182/blood-2002-05-1343 2002-05-1343 [pii]
146. Palmer RH, Vernersson E, Grabbe C, Hallberg B. Anaplastic lymphoma kinase: signalling in development and disease. *Biochem J*. Jun 15 2009;420(3):345-61. doi:BJ20090387 [pii] 10.1042/BJ20090387
147. Kinney MC, Higgins RA, Medina EA. Anaplastic large cell lymphoma: twenty-five years of discovery. *Archives of pathology & laboratory medicine*. Jan 2011;135(1):19-43. doi:10.1043/2010-0507-RAR.1
148. Liu B, Li J, Cairns MJ. Identifying miRNAs, targets and functions. *Briefings in bioinformatics*. Jan 2014;15(1):1-19. doi:10.1093/bib/bbs075

149. Spaccarotella E, Pellegrino E, Ferracin M, et al. STAT3-mediated activation of microRNA cluster 17~92 promotes proliferation and survival of ALK-positive anaplastic large cell lymphoma. *Haematologica*. Jan 2014;99(1):116-24. doi:10.3324/haematol.2013.088286
150. Hoareau-Aveilla C, Meggetto F. Crosstalk between microRNA and DNA Methylation Offers Potential Biomarkers and Targeted Therapies in ALK-Positive Lymphomas. *Cancers (Basel)*. Aug 3 2017;9(8)doi:10.3390/cancers9080100
151. Testa U, Pelosi E, Castelli G, Labbaye C. miR-146 and miR-155: Two Key Modulators of Immune Response and Tumor Development. *Noncoding RNA*. 2017;3(3):22. doi:10.3390/ncrna3030022
152. Chen J, Zhang K, Xu Y, et al. The role of microRNA-26a in human cancer progression and clinical application. *Tumour biology : the journal of the International Society for Oncodevelopmental Biology and Medicine*. Jun 2016;37(6):7095-108. doi:10.1007/s13277-016-5017-y
153. Feng X, Zhang C, Yang Y, Hou D, Zhu A. Role of miR-181a in the process of apoptosis of multiple malignant tumors: A literature review. *Advances in clinical and experimental medicine : official organ Wroclaw Medical University*. Feb 2018;27(2):263-270. doi:10.17219/acem/66842
154. Campo E, Swerdlow SH, Harris NL, Pileri S, Stein H, Jaffe ES. The 2008 WHO classification of lymphoid neoplasms and beyond: evolving concepts and practical applications. *Blood*. May 12 2011;117(19):5019-32. doi:10.1182/blood-2011-01-293050
155. Yates AD, Achuthan P, Akanni W, et al. Ensembl 2020. *Nucleic Acids Research*. 2019;48(D1):D682-D688. doi:10.1093/nar/gkz966
156. Robinson JT, Thorvaldsdóttir H, Winckler W, et al. Integrative genomics viewer. *Nat Biotechnol*. 2011;29(1):24-26. doi:10.1038/nbt.1754
157. John B, Enright AJ, Aravin A, Tuschl T, Sander C, Marks DS. Human MicroRNA Targets. *PLOS Biology*. 2004;2(11):e363. doi:10.1371/journal.pbio.0020363
158. Enright AJ, John B, Gaul U, Tuschl T, Sander C, Marks DS. MicroRNA targets in Drosophila. *Genome Biology*. 2003/12/12 2003;5(1):R1. doi:10.1186/gb-2003-5-1-r1
159. Agarwal V, Bell GW, Nam J-W, Bartel DP. Predicting effective microRNA target sites in mammalian mRNAs. *Elife*. 2015;4:e05005. doi:10.7554/eLife.05005
160. Miranda KC, Huynh T, Tay Y, et al. A Pattern-Based Method for the Identification of MicroRNA Binding Sites and Their Corresponding Heteroduplexes. *Cell*. 2006/09/22/ 2006;126(6):1203-1217. doi:https://doi.org/10.1016/j.cell.2006.07.031
161. Dweep H, Gretz N. miRWalk2.0: a comprehensive atlas of microRNA-target interactions. *Nat Methods*. Aug 2015;12(8):697. doi:10.1038/nmeth.3485
162. Vejnar CE, Blum M, Zdobnov EM. miRmap web: comprehensive microRNA target prediction online. *Nucleic Acids Research*. 2013;41(W1):W165-W168. doi:10.1093/nar/gkt430
163. Jassal B, Matthews L, Viteri G, et al. The reactome pathway knowledgebase. *Nucleic Acids Res*. Jan 8 2020;48(D1):D498-d503. doi:10.1093/nar/gkz1031
164. Mi H, Thomas P. PANTHER pathway: an ontology-based pathway database coupled with data analysis tools. *Methods Mol Biol*. 2009;563:123-140. doi:10.1007/978-1-60761-175-2_7
165. Koch I, Slotta-Huspenina J, Hollweck R, et al. Real-time quantitative RT-PCR shows variable, assay-dependent sensitivity to formalin fixation: implications for direct comparison of transcript levels in paraffin-embedded tissues. *Diagn Mol Pathol*. Sep 2006;15(3):149-56. doi:10.1097/01.pdm.0000213450.99655.54 00019606-200609000-00005 [pii]

166. Dobin A, Davis CA, Schlesinger F, et al. STAR: ultrafast universal RNA-seq aligner. *Bioinformatics*. Jan 1 2013;29(1):15-21. doi:10.1093/bioinformatics/bts635
167. Love MI, Huber W, Anders S. Moderated estimation of fold change and dispersion for RNA-seq data with DESeq2. *Genome Biol*. 2014;15(12):550. doi:10.1186/s13059-014-0550-8
168. Galili T. dendextend: an R package for visualizing, adjusting and comparing trees of hierarchical clustering. *Bioinformatics*. Nov 15 2015;31(22):3718-20. doi:10.1093/bioinformatics/btv428
169. Mootha VK, Lindgren CM, Eriksson KF, et al. PGC-1alpha-responsive genes involved in oxidative phosphorylation are coordinately downregulated in human diabetes. *Nat Genet*. Jul 2003;34(3):267-73. doi:10.1038/ng1180
170. Subramanian A, Tamayo P, Mootha VK, et al. Gene set enrichment analysis: a knowledge-based approach for interpreting genome-wide expression profiles. *Proc Natl Acad Sci U S A*. Oct 25 2005;102(43):15545-50. doi:10.1073/pnas.0506580102
171. Fabregat A, Sidiropoulos K, Garapati P, et al. The Reactome pathway Knowledgebase. *Nucleic Acids Res*. Jan 4 2016;44(D1):D481-7. doi:10.1093/nar/gkv1351
172. Milacic M, Haw R, Rothfels K, et al. Annotating cancer variants and anti-cancer therapeutics in reactome. *Cancers (Basel)*. Nov 8 2012;4(4):1180-211. doi:10.3390/cancers4041180
173. Shalem O, Sanjana NE, Hartenian E, et al. Genome-scale CRISPR-Cas9 knockout screening in human cells. *Science*. Jan 3 2014;343(6166):84-87. doi:10.1126/science.1247005
174. Sanjana NE, Shalem O, Zhang F. Improved vectors and genome-wide libraries for CRISPR screening. *Nature methods*. 2014;11(8):783-784. doi:10.1038/nmeth.3047
175. McManus MT, Haines BB, Dillon CP, et al. Small interfering RNA-mediated gene silencing in T lymphocytes. *J Immunol*. Nov 15 2002;169(10):5754-60. doi:10.4049/jimmunol.169.10.5754
176. McManus MT, Petersen CP, Haines BB, Chen J, Sharp PA. Gene silencing using micro-RNA designed hairpins. *RNA*. Jun 2002;8(6):842-50. doi:10.1017/s1355838202024032
177. Moore CB, Guthrie EH, Huang MT, Taxman DJ. Short hairpin RNA (shRNA): design, delivery, and assessment of gene knockdown. *Methods Mol Biol*. 2010;629:141-58. doi:10.1007/978-1-60761-657-3_10
178. Anastasov N, Klier M, Koch I, et al. Efficient shRNA delivery into B and T lymphoma cells using lentiviral vector-mediated transfer. *J Hematop*. Mar 2009;2(1):9-19. doi:10.1007/s12308-008-0020-x
179. Nusse M, Beisker W, Kramer J, et al. Measurement of micronuclei by flow cytometry. *Methods Cell Biol*. 1994;42 Pt B:149-58. doi:10.1016/s0091-679x(08)61072-9
180. Wolburg-Buchholz K, Mack AF, Steiner E, Pfeiffer F, Engelhardt B, Wolburg H. Loss of astrocyte polarity marks blood-brain barrier impairment during experimental autoimmune encephalomyelitis. *Acta neuropathologica*. Aug 2009;118(2):219-33. doi:10.1007/s00401-009-0558-4
181. Leuthold P, Schaeffeler E, Winter S, et al. Comprehensive Metabolomic and Lipidomic Profiling of Human Kidney Tissue: A Platform Comparison. *J Proteome Res*. Feb 3 2017;16(2):933-944. doi:10.1021/acs.jproteome.6b00875
182. Hofmann U, Maier K, Niebel A, Vacun G, Reuss M, Mauch K. Identification of metabolic fluxes in hepatic cells from transient 13C-labeling experiments: Part I. Experimental observations. *Biotechnol Bioeng*. Jun 1 2008;100(2):344-54. doi:10.1002/bit.21747

183. Piva R, Pellegrino E, Mattioli M, et al. Functional validation of the anaplastic lymphoma kinase signature identifies CEBPB and BCL2A1 as critical target genes. *J Clin Invest*. Dec 2006;116(12):3171-82. doi:10.1172/JCI29401
184. Montes-Mojarro IA, Steinhilber J, Griessinger CM, et al. CD147 a direct target of miR-146a supports energy metabolism and promotes tumor growth in ALK+ ALCL. *Leukemia*. Aug 2022;36(8):2050-2063. doi:10.1038/s41375-022-01617-x
185. Ebert MS, Sharp PA. Roles for microRNAs in conferring robustness to biological processes. *Cell*. Apr 27 2012;149(3):515-24. doi:10.1016/j.cell.2012.04.005
186. Bartel DP. MicroRNAs: genomics, biogenesis, mechanism, and function. *Cell*. Jan 23 2004;116(2):281-97. doi:10.1016/s0092-8674(04)00045-5
187. Cui M, Wang H, Yao X, et al. Circulating MicroRNAs in Cancer: Potential and Challenge. Review. *Frontiers in Genetics*. 2019-July-18 2019;10(626)doi:10.3389/fgene.2019.00626
188. Shah V, Shah J. Recent trends in targeting miRNAs for cancer therapy. *Journal of Pharmacy and Pharmacology*. 2020;72(12):1732-1749. doi:https://doi.org/10.1111/jphp.13351
189. Weiler J, Hunziker J, Hall J. Anti-miRNA oligonucleotides (AMOs): ammunition to target miRNAs implicated in human disease? *Gene therapy*. Mar 2006;13(6):496-502. doi:10.1038/sj.gt.3302654
190. Krützfeldt J, Rajewsky N, Braich R, et al. Silencing of microRNAs in vivo with 'antagomirs'. *Nature*. Dec 1 2005;438(7068):685-9. doi:10.1038/nature04303
191. Ebert MS, Neilson JR, Sharp PA. MicroRNA sponges: competitive inhibitors of small RNAs in mammalian cells. *Nat Methods*. Sep 2007;4(9):721-6. doi:10.1038/nmeth1079
192. Gaidatzis D, van Nimwegen E, Hausser J, Zavolan M. Inference of miRNA targets using evolutionary conservation and pathway analysis. *BMC Bioinformatics*. 2007/03/01 2007;8(1):69. doi:10.1186/1471-2105-8-69
193. Lewis BP, Shih Ih, Jones-Rhoades MW, Bartel DP, Burge CB. Prediction of Mammalian MicroRNA Targets. *Cell*. 2003/12/26/ 2003;115(7):787-798. doi:https://doi.org/10.1016/S0092-8674(03)01018-3
194. Lewis BP, Burge CB, Bartel DP. Conserved Seed Pairing, Often Flanked by Adenosines, Indicates that Thousands of Human Genes are MicroRNA Targets. *Cell*. 2005/01/14/ 2005;120(1):15-20. doi:https://doi.org/10.1016/j.cell.2004.12.035
195. Khorshid M, Hausser J, Zavolan M, van Nimwegen E. A biophysical miRNA-mRNA interaction model infers canonical and noncanonical targets. *Nature Methods*. 2013/03/01 2013;10(3):253-255. doi:10.1038/nmeth.2341
196. Kuhn DE, Martin MM, Feldman DS, Terry AV, Jr., Nuovo GJ, Elton TS. Experimental validation of miRNA targets. *Methods*. Jan 2008;44(1):47-54. doi:10.1016/j.ymeth.2007.09.005
197. Chen C-Z, Li L, Lodish HF, Bartel DP. MicroRNAs Modulate Hematopoietic Lineage Differentiation. *Science*. 2004;303(5654):83. doi:10.1126/science.1091903
198. Shen H, Weng XD, Liu XH, et al. miR-181a-5p is downregulated and inhibits proliferation and the cell cycle in prostate cancer. *Int J Clin Exp Pathol*. 2018;11(8):3969-3976.
199. Lim CX, Lee B, Geiger O, et al. miR-181a Modulation of ERK-MAPK Signaling Sustains DC-SIGN Expression and Limits Activation of Monocyte-Derived Dendritic Cells. *Cell Reports*. 2020;30(11):3793-3805.e5. doi:10.1016/j.celrep.2020.02.077
200. Lappano R, Maggiolini M. GPCRs and cancer. *Acta Pharmacol Sin*. Mar 2012;33(3):351-62. doi:10.1038/aps.2011.183

201. Nohata N, Goto Y, Gutkind JS. Onco-GPCR signaling and dysregulated expression of microRNAs in human cancer. *Journal of human genetics*. Jan 2017;62(1):87-96. doi:10.1038/jhg.2016.124
202. Nallanthighal S, Heiserman JP, Cheon DJ. The Role of the Extracellular Matrix in Cancer Stemness. *Front Cell Dev Biol*. 2019;7:86. doi:10.3389/fcell.2019.00086
203. Li Y, Kuscu C, Banach A, et al. miR-181a-5p Inhibits Cancer Cell Migration and Angiogenesis via Downregulation of Matrix Metalloproteinase-14. *Cancer Res*. Jul 1 2015;75(13):2674-85. doi:10.1158/0008-5472.Can-14-2875
204. Kim JT, Lee S-O, Lim S, et al. microRNA 181a-5p Reprogramed Glucose and Lipid Metabolism in Non- Small Cell Lung Cancer. 2018:
205. Kuo CC, Ling HH, Chiang MC, et al. Metastatic Colorectal Cancer Rewrites Metabolic Program Through a Glut3-YAP-dependent Signaling Circuit. *Theranostics*. 2019;9(9):2526-2540. doi:10.7150/thno.32915
206. Fei X, Qi M, Wu B, Song Y, Wang Y, Li T. MicroRNA-195-5p suppresses glucose uptake and proliferation of human bladder cancer T24 cells by regulating GLUT3 expression. *FEBS Lett*. Feb 17 2012;586(4):392-7. doi:10.1016/j.febslet.2012.01.006
207. Xu Y, Zhou X, Zhang S, Nanding A, Xuan Q. Expression and Prognostic Value of Glucose Transporter 3 in Diffuse Large B Cell Lymphoma. *Onco Targets Ther*. 2022;15:181-191. doi:10.2147/OTT.S338826
208. Bonzheim I, Irmler M, Klier-Richter M, et al. Identification of C/EBPbeta target genes in ALK+ anaplastic large cell lymphoma (ALCL) by gene expression profiling and chromatin immunoprecipitation. *PLoS One*. 2013;8(5):e64544. doi:10.1371/journal.pone.0064544
209. Zapolnik P, Zapolnik B. MicroRNA-26a-5p: multiple functions, multiple possibilities – a mini-review. journal article. *Journal of Pre-Clinical and Clinical Research*. 2020;14(4):130-133. doi:10.26444/jpccr/128009
210. Zhang W, Fu X, Xie J, Pan H, Han W, Huang W. miR-26a attenuates colitis and colitis-associated cancer by targeting the multiple intestinal inflammatory pathways. *Molecular Therapy - Nucleic Acids*. 2021/06/04/ 2021;24:264-273. doi:https://doi.org/10.1016/j.omtn.2021.02.029
211. Zhu H, Vishwamitra D, Curry CV, et al. NPM-ALK up-regulates iNOS expression through a STAT3/microRNA-26a-dependent mechanism. *The Journal of Pathology*. 2013;230(1):82-94. doi:https://doi.org/10.1002/path.4171
212. Galvagni F, Nardi F, Spiga O, et al. Dissecting the CD93-Multimerin 2 interaction involved in cell adhesion and migration of the activated endothelium. *Matrix Biol*. Dec 2017;64:112-127. doi:10.1016/j.matbio.2017.08.003
213. Langenkamp E, Zhang L, Lugano R, et al. Elevated expression of the C-type lectin CD93 in the glioblastoma vasculature regulates cytoskeletal rearrangements that enhance vessel function and reduce host survival. *Cancer Res*. Nov 1 2015;75(21):4504-16. doi:10.1158/0008-5472.Can-14-3636
214. Tong W, Wang G, Zhu L, et al. Pan-Cancer Analysis Identified CD93 as a Valuable Biomarker for Predicting Patient Prognosis and Immunotherapy Response. Original Research. *Frontiers in Molecular Biosciences*. 2022-February-21 2022;8doi:10.3389/fmolb.2021.793445
215. Lugano R, Vemuri K, Yu D, et al. CD93 promotes β1 integrin activation and fibronectin fibrillogenesis during tumor angiogenesis. *The Journal of Clinical Investigation*. 08/01/ 2018;128(8):3280-3297. doi:10.1172/JCI97459
216. Liu C, Cui Z, Wang S, Zhang D. CD93 and GIPC expression and localization during central nervous system inflammation. *Neural Regeneration Research*. 2014;9(22)
217. Janoueix-Lerosey I, Lopez-Delisle L, Delattre O, Rohrer H. The ALK receptor in sympathetic neuron development and neuroblastoma. *Cell Tissue Res*. May 2018;372(2):325-337. doi:10.1007/s00441-017-2784-8

218. Uhlén M, Fagerberg L, Hallström BM, et al. Tissue-based map of the human proteome. *Science*. 2015;347(6220):1260419. doi:doi:10.1126/science.1260419
219. Chang HY, Lee CH, Li YS, et al. MicroRNA-146a suppresses tumor malignancy via targeting vimentin in esophageal squamous cell carcinoma cells with lower fibronectin membrane assembly. *J Biomed Sci*. Nov 28 2020;27(1):102. doi:10.1186/s12929-020-00693-4
220. Huang WT, He RQ, Li XJ, et al. miR-146a-5p targets TCSF and influences cell growth and apoptosis to repress NSCLC progression. *Oncology reports*. Apr 2019;41(4):2226-2240. doi:10.3892/or.2019.7030
221. Simanovich E, Brod V, Rahat MM, Rahat MA. Function of miR-146a-5p in Tumor Cells As a Regulatory Switch between Cell Death and Angiogenesis: Macrophage Therapy Revisited. *Front Immunol*. 2017;8:1931. doi:10.3389/fimmu.2017.01931
222. Dash S, Balasubramaniam M, Dash C, Pandhare J. Biotin-based Pulldown Assay to Validate mRNA Targets of Cellular miRNAs. *J Vis Exp*. Jun 12 2018;(136)doi:10.3791/57786
223. Feitelson MA, Arzumanyan A, Kulathinal RJ, et al. Sustained proliferation in cancer: Mechanisms and novel therapeutic targets. *Seminars in Cancer Biology*. 2015/12/01/ 2015;35:S25-S54. doi:https://doi.org/10.1016/j.semcancer.2015.02.006
224. Nabeshima K, Iwasaki H, Koga K, Hojo H, Suzumiya J, Kikuchi M. Emmprin (basigin/CD147): matrix metalloproteinase modulator and multifunctional cell recognition molecule that plays a critical role in cancer progression. *Pathol Int*. Jul 2006;56(7):359-67. doi:PIN [pii] 10.1111/j.1440-1827.2006.01972.x
225. Sameshima T, Nabeshima K, Toole BP, et al. Glioma cell extracellular matrix metalloproteinase inducer (EMMPRIN) (CD147) stimulates production of membrane-type matrix metalloproteinases and activated gelatinase A in co-cultures with brain-derived fibroblasts. *Cancer Lett*. Sep 01 2000;157(2):177-84.
226. Yang S, Qi F, Tang C, et al. CD147 promotes the proliferation, invasiveness, migration and angiogenesis of human lung carcinoma cells. *Oncol Lett*. 2017/02/01 2017;13(2):898-904. doi:10.3892/ol.2016.5502
227. Chen X, Lin J, Kanekura T, et al. A small interfering CD147-targeting RNA inhibited the proliferation, invasiveness, and metastatic activity of malignant melanoma. *Cancer Res*. Dec 01 2006;66(23):11323-30. doi:10.1158/0008-5472.CAN-06-1536
228. Lugano R, Ramachandran M, Dimberg A. Tumor angiogenesis: causes, consequences, challenges and opportunities. *Cellular and Molecular Life Sciences*. 2020/05/01 2020;77(9):1745-1770. doi:10.1007/s00018-019-03351-7
229. Gupta MK, Qin RY. Mechanism and its regulation of tumor-induced angiogenesis. *World J Gastroenterol*. Jun 2003;9(6):1144-55. doi:10.3748/wjg.v9.i6.1144
230. Marmé D. Tumor Angiogenesis: A Key Target for Cancer Therapy. *Oncology Research and Treatment*. 2018;41(4):164-164. doi:10.1159/000488340
231. Zhu K, Pan Q, Zhang X, et al. MiR-146a enhances angiogenic activity of endothelial cells in hepatocellular carcinoma by promoting PDGFRA expression. *Carcinogenesis*. 2013;34(9):2071-2079. doi:10.1093/carcin/bgt160
232. Hanahan D, Weinberg Robert A. Hallmarks of Cancer: The Next Generation. *Cell*. 2011/03/04/ 2011;144(5):646-674. doi:https://doi.org/10.1016/j.cell.2011.02.013
233. Hahn JN, Kaushik DK, Yong VW. The role of EMMPRIN in T cell biology and immunological diseases. *J Leukoc Biol*. Jul 2015;98(1):33-48. doi:10.1189/jlb.3RU0215-045R
234. Xiong L, Edwards CK, 3rd, Zhou L. The biological function and clinical utilization of CD147 in human diseases: a review of the current scientific literature. *International journal of molecular sciences*. Sep 29 2014;15(10):17411-41. doi:10.3390/ijms151017411

235. Le Floch R, Chiche J, Marchiq I, et al. CD147 subunit of lactate/H+ symporters MCT1 and hypoxia-inducible MCT4 is critical for energetics and growth of glycolytic tumors. *Proc Natl Acad Sci U S A*. Oct 4 2011;108(40):16663-8. doi:10.1073/pnas.1106123108
236. Huang Q, Li J, Xing J, et al. CD147 promotes reprogramming of glucose metabolism and cell proliferation in HCC cells by inhibiting the p53-dependent signaling pathway. *Journal of hepatology*. 2014/10/01/ 2014;61(4):859-866. doi:https://doi.org/10.1016/j.jhep.2014.04.035
237. Li X, Zhang Y, Ma W, et al. Enhanced glucose metabolism mediated by CD147 contributes to immunosuppression in hepatocellular carcinoma. *Cancer Immunology, Immunotherapy*. 2020/04/01 2020;69(4):535-548. doi:10.1007/s00262-019-02457-y
238. Kirk P, Wilson MC, Heddle C, Brown MH, Barclay AN, Halestrap AP. CD147 is tightly associated with lactate transporters MCT1 and MCT4 and facilitates their cell surface expression. *EMBO J*. Aug 1 2000;19(15):3896-904. doi:10.1093/emboj/19.15.3896
239. Philp NJ, Wang D, Yoon H, Hjelmeland LM. Polarized expression of monocarboxylate transporters in human retinal pigment epithelium and ARPE-19 cells. *Investigative ophthalmology & visual science*. Apr 2003;44(4):1716-21.
240. Marchiq I, Le Floch R, Roux D, Simon MP, Pouyssegur J. Genetic disruption of lactate/H+ symporters (MCTs) and their subunit CD147/BASIGIN sensitizes glycolytic tumor cells to phenformin. *Cancer Res*. Jan 1 2015;75(1):171-80. doi:10.1158/0008-5472.Can-14-2260
241. Granja S, Marchiq I, Le Floch R, Moura CS, Baltazar F, Pouysségur J. Disruption of BASIGIN decreases lactic acid export and sensitizes non-small cell lung cancer to biguanides independently of the LKB1 status. *Oncotarget*. Mar 30 2015;6(9):6708-21. doi:10.18632/oncotarget.2862
242. Tondera D, Grandemange S, Jourdain A, et al. SLP-2 is required for stress-induced mitochondrial hyperfusion. *Embo j*. Jun 3 2009;28(11):1589-600. doi:10.1038/emboj.2009.89
243. Khacho M, Tarabay M, Patten D, et al. Acidosis overrides oxygen deprivation to maintain mitochondrial function and cell survival. *Nat Commun*. Apr 1 2014;5:3550. doi:10.1038/ncomms4550
244. Solaini G, Baracca A, Lenaz G, Sgarbi G. Hypoxia and mitochondrial oxidative metabolism. *Biochimica et Biophysica Acta (BBA) - Bioenergetics*. 2010/06/01/ 2010;1797(6):1171-1177. doi:https://doi.org/10.1016/j.bbabio.2010.02.011
245. Jiang J, Jiang Y, Zhang Y-G, et al. The effects of hypoxia on mitochondrial function and metabolism in gastric cancer cells. *Translational Cancer Research*. 2021;10(2):817-826.
246. Chapman J, Fielder E, Passos JF. Mitochondrial dysfunction and cell senescence: deciphering a complex relationship. *FEBS Letters*. 2019;593(13):1566-1579. doi:https://doi.org/10.1002/1873-3468.13498
247. Nunnari J, Suomalainen A. Mitochondria: in sickness and in health. *Cell*. Mar 16 2012;148(6):1145-59. doi:10.1016/j.cell.2012.02.035
248. Hutter E, Renner K, Pfister G, Stöckl P, Jansen-Dürr P, Gnaiger E. Senescence-associated changes in respiration and oxidative phosphorylation in primary human fibroblasts. *Biochem J*. Jun 15 2004;380(Pt 3):919-28. doi:10.1042/bj20040095
249. Ogrodnik M, Miwa S, Tchkonia T, et al. Cellular senescence drives age-dependent hepatic steatosis. *Nat Commun*. Jun 13 2017;8:15691. doi:10.1038/ncomms15691
250. Fendt S-M, Bell EL, Keibler MA, et al. Reductive glutamine metabolism is a function of the α-ketoglutarate to citrate ratio in cells. *Nature Communications*. 2013/07/31 2013;4(1):2236. doi:10.1038/ncomms3236

251. Paolicelli RC, Widmann C. Squalene: friend or foe for cancers. *Current Opinion in Lipidology*. 2019;30(4)
252. Ambrosio MR, Piccaluga PP, Ponzoni M, et al. The alteration of lipid metabolism in Burkitt lymphoma identifies a novel marker: adipophilin. *PLoS One*. 2012;7(8):e44315. doi:10.1371/journal.pone.0044315
253. Butler LM, Perone Y, Dehairs J, et al. Lipids and cancer: Emerging roles in pathogenesis, diagnosis and therapeutic intervention. *Advanced Drug Delivery Reviews*. 2020/01/01/ 2020;159:245-293. doi:https://doi.org/10.1016/j.addr.2020.07.013
254. Dean NR, Newman JR, Helman EE, et al. Anti-EMMPRIN monoclonal antibody as a novel agent for therapy of head and neck cancer. *Clin Cancer Res*. Jun 15 2009;15(12):4058-65. doi:10.1158/1078-0432.Ccr-09-0212
255. Hu X, Su J, Zhou Y, et al. Repressing CD147 is a novel therapeutic strategy for malignant melanoma. *Oncotarget*. Apr 11 2017;8(15):25806-25813. doi:10.18632/oncotarget.15709
256. Xu J, Shen ZY, Chen XG, et al. A randomized controlled trial of Licartin for preventing hepatoma recurrence after liver transplantation. *Hepatology*. Feb 2007;45(2):269-76. doi:10.1002/hep.21465
257. Wu L, Yang YF, Ge NJ, et al. Hepatic arterial iodine-131-labeled metuximab injection combined with chemoembolization for unresectable hepatocellular carcinoma: interim safety and survival data from 110 patients. *Cancer Biother Radiopharm*. Dec 2010;25(6):657-63. doi:10.1089/cbr.2010.0801
258. Wang M, Zhang S, Sun Q, et al. Dual effects of an anti-CD147 antibody for Esophageal cancer therapy. *Cancer Biology & Therapy*. 2019/12/02 2019;20(12):1443-1452. doi:10.1080/15384047.2019.1647052
259. Tseng H-c, Xiong W, Badeti S, et al. Efficacy of anti-CD147 chimeric antigen receptors targeting hepatocellular carcinoma. *Nature Communications*. 2020/09/23 2020;11(1):4810. doi:10.1038/s41467-020-18444-2
260. Eichner R, Heider M, Fernandez-Saiz V, et al. Immunomodulatory drugs disrupt the cereblon-CD147-MCT1 axis to exert antitumor activity and teratogenicity. *Nat Med*. Jul 2016;22(7):735-43. doi:10.1038/nm.4128
261. Baumann V, Winkler J. miRNA-based therapies: strategies and delivery platforms for oligonucleotide and non-oligonucleotide agents. *Future Med Chem*. 2014;6(17):1967-84. doi:10.4155/fmc.14.116
262. Rupaimoole R, Slack FJ. MicroRNA therapeutics: towards a new era for the management of cancer and other diseases. *Nature Reviews Drug Discovery*. 2017/03/01 2017;16(3):203-222. doi:10.1038/nrd.2016.246
263. Fuertes T, Ramiro AR, de Yebenes VG. miRNA-Based Therapies in B Cell Non-Hodgkin Lymphoma. *Trends in Immunology*. 2020/10/01/ 2020;41(10):932-947. doi:https://doi.org/10.1016/j.it.2020.08.006
264. Nana-Sinkam SP, Croce CM. MicroRNA regulation of tumorigenesis, cancer progression and interpatient heterogeneity: towards clinical use. *Genome Biology*. 2014/08/31 2014;15(9):445. doi:10.1186/s13059-014-0445-8

8. Declaration of contribution of others.

Statutory Declaration

Hereby I affirm that I wrote this Doctoral thesis independently with the topic.

“The role of Anaplastic Lymphoma Kinase (ALK) and CEBPβ-regulated miRNAs in ALK+ Anaplastic Large Cell Lymphoma”

and that I used no other aids than those cited. In each individual case, I have clearly identified the source of the passages that are taken paraphrased from other works and the linked manuscript. The work was carried out in the Institute of Pathology and Neuropathology under the supervision of the Prof. Falko Fend. The study was designed by Prof. Quintanilla-Fend, PD. Dr. Irina Bonzheim, Dr. Julia Steinhilber, Prof Falko Fend together with myself. The majority of the experiments were performed by me, following the advices of other laboratory members, specifically PD. Dr Irina Bonzheim, Dr. Julia Steinhilber and with the assistance of Biol. Esther Kohler. The identification of miR-146a target genes (transcriptome analysis) was mainly achieved by Dr. Julia Steinhilber and mentioned in her doctoral thesis, and only confirmatory experiments were conducted by me. The experiments for the downregulation of CD147 by shRNA were based on previous work of my colleague Mol. Med. Achim Rau as part of her Bachelor Thesis. Similarly, the experiments for miR-146a-CD147 direct regulation by luciferase assay were based on previous work by Ann-Kathrin Gersmann, as cited in the text, as part of her Medical Doctoral Thesis. The experiments from the mouse model were mainly performed by PD. Dr. Irina Bonzheim, Dr. Julia Steinhilber, and me. PET-MRT image analysis by Dr. Griessinger. Metabolomics was made in collaboration Dr. Prof. Dr. Matthias Schwab at the Dr. Margarete Fischer-Bosch-Institut für Klinische Pharmakologie and electronic microscopy with Dr. Fallier Becker in the Institute of Pathology and Neuropathology. The statistical analysis was completed by me with the guidance of M.D. Lina Maria Serna-Higuita, as part of the consultation with the Institute of Biometry. I acknowledge the work done by collaborators. I affirm to have completed the manuscript independently and I performed the scientific studies according to the principles of good scientific practice.

Ivonne A. Montes-Mojarro

_____ 07.02.2023, Tübingen, Germany

9. Publications.

Publications related to this thesis:

Leukemia (IF: 12.88)

- **Montes-Mojarro I-A,** Steinhilber J, Griessinger CM, Rau A, Gersmann A-K, Kohlhofer U, Fallier-Becker P, Liang H-C, Hofmann U, Haag M, Klapper W, Schaeffeler E, Pichler BJ, Schwab M, Fend F, Bonzheim I, Quintanilla-Martinez. CD147 a direct target of miR-146a supports energy metabolism and promotes tumor growth in ALK+ ALCL. *Leukemia*. Aug 2022;36(8):2050-2063. doi:10.1038/s41375-022-01617-x.
  Ivonne A. Montes-Mojarro performed the experiments described in this thesis. She analyzed, and interpreted the data and wrote the draft of the manuscript.
- Lobello, C.; Tichy, B.; Bystry, V.; Radova, L.; Filip, D.; Mraz, M.; **Montes-Mojarro, I.A.;** Prokoph, N.; Larose, H.; Liang, H.C., et al. STAT3 and TP53 mutations associate with poor prognosis in anaplastic large cell lymphoma. *Leukemia* **2021**, *35*, 1500-1505, doi:10.1038/s41375-020-01093-1.
  Ivonne A. Montes-Mojarro performed immunohistochemical analysis of STAT3 and TP53 to confirm mutational status at the protein level, wrote the corresponding methodology, figures, and legends and reviewed the manuscript.

Nature Communications (17.69)

- Liang, H.C.; Costanza, M.; Prutsch, N.; Zimmerman, M.W.; Gurnhofer, E.; **Montes-Mojarro, I.A.**; Abraham, B.J.; Prokoph, N.; Stoiber, S.; Tangermann, S., et al. Super-enhancer-based identification of a BATF3/IL-2R-module reveals vulnerabilities in anaplastic large cell lymphoma. *Nat Commun* **2021**, *12*, 5577, doi:10.1038/s41467-021-25379-9.
  Ivonne A. Montes-Mojarro reviewed and quantified the immunohistochemistry of IL2R and BATF3, wrote the corresponding methodology and results and reviewed the manuscript.

Blood (IF:23.62)

- Prokoph, N.; Probst, N.A.; Lee, L.C.; Monahan, J.M.; Matthews, J.D.; Liang, H.C.; Bahnsen, K.; **Montes-Mojarro, I.A**.; Karaca-Atabay, E.; Sharma, G.G., et al. IL10RA modulates crizotinib sensitivity in NPM1-ALK+ anaplastic large cell lymphoma. *Blood* **2020**, *136*, 1657-1669, doi:10.1182/blood.2019003793.
  Ivonne A. Montes-Mojarro provided the histological pictures of T-cell lymphomas, reviewed and quantified the immunohistochemistry of IL10RA, wrote the correspond-

ing methodology and results, reviewed the manuscript, and designed the cover photo for Blood. Volume 136, Issue 14. October 2020.

Cancers (IF: 6.64)

- **Montes-Mojarro, I.A.**; Steinhilber, J.; Bonzheim, I.; Quintanilla-Martinez, L.; Fend, F. The Pathological Spectrum of Systemic Anaplastic Large Cell Lymphoma (ALCL). *Cancers (Basel)* **2018**, *10*, doi:10.3390/cancers10040107.
  Ivonne A. Montes-Mojarro wrote the manuscript and made the figures and tables.

Laboratory Investigation (IF: 5.86):

- Schmidt J, Bonzheim I, Steinhilber J, **Montes-Mojarro IA,** Ortiz-Hidalgo C, Klapper W, Fend F, Quintanilla-Martinez L (2017) EMMPRIN (CD147) is induced by C/EBP-beta and is differentially expressed in ALK+ and ALK- anaplastic large-cell lymphoma Lab Invest 97:1095-1102. doi: 10.1038/labinvest.2017.54
  Ivonne A. Montes-Mojarro helped in the revision and quantification of the CD147 immunohistochemistry and reviewed the manuscript.

Publications not related to this thesis:

International Journal of molecular sciences (IF: 4.55)

- **Montes-Mojarro IA**, Hassas S, Staehle S, et al. Multiparametric Classification of Non-Muscle Invasive Papillary Urothelial Neoplasms: Combining Morphological, Phenotypical, and Molecular Features for Improved Risk Stratification. International journal of molecular sciences. Jul 23, 2022;23(15) doi:10.3390/ijms23158133
  Ivonne A. Montes-Mojarro wrote the manuscript, made the figures and tables.
- Geng R, Harland N, **Montes-Mojarro IA**, et al. CD24: A Marker for an Extended Expansion Potential of Urothelial Cancer Cell Organoids In Vitro? International journal of molecular sciences. May 13, 2022;23(10) doi:10.3390/ijms23105453
- Ivonne A. Montes-Mojarro performed the histological and immunohistochemical analysis of protein expression of the organoids, wrote the corresponding methodology, prepared the corresponding figures, and reviewed the manuscript.
- Harland N, Maurer FB, Abruzzese T, Bock C, **Montes-Mojarro IA,** Fend F, Aicher WK, Stenzl A, Amend B Elevated Expression of the Immune Checkpoint Ligand CD276 (B7-H3) in Urothelial Carcinoma Cell Lines Correlates Negatively with the Cell Proliferation. International journal of molecular sciences. Apr 29 2022;23(9) doi:10.3390/ijms23094969
  Ivonne A. Montes-Mojarro helped in the revision and quantification of the immunohistochemistry and reviewed the manuscript.

***Haematologica* (IF: 11.04)**

- Vogelsberg A, Steinhilber J, Mankel B, Federmann B, Schmidt J, **Montes-Mojarro IA**, Huttl K, Rodriguez-Pinilla M, Baskaran P, Nahnsen S, Piris MA, Ott G, Quintanilla-Martinez L, Bonzheim I, Fend F. Genetic evolution of in situ follicular neoplasia to aggressive B-cell lymphoma of germinal center subtype. Haematologica. Oct 1 2021;106(10):2673-2681. doi:10.3324/haematol.2020.254854

  Ivonne A. Montes-Mojarro helped in selecting the cases and preparing the illustrations.

Cancers (IF: 6. 64)

- **Montes-Mojarro IA**, Fend F, Quintanilla-Martinez L. EBV and the Pathogenesis of NK/T Cell Lymphoma. Cancers (Basel) 2021 Mar 19; 13(6).

  Ivonne A. Montes-Mojarro wrote the manuscript, made the figures and tables.

Modern Pathology (IF: 8,20)

- **Montes-Mojarro IA,** Chen BJ, Ramirez-Ibarguen AF, Quezada-Fiallos CM, Pérez-Báez WB, Dueñas D, Casavilca-Zambrano S, Ortiz-Mayor M, Rojas-Bilbao E, García-Rivello H, Metrebian MF, Narbaitz M, Barrionuevo C, Lome-Maldonado C, Bonzheim I, Fend F, Steinhilber J, Quintanilla-Martinez L. Mutational profile and EBV strains of extranodal NK/T-cell lymphoma, nasal type in Latin America. Mod Pathol 2020 May;33(5):781-791. doi: 10.1038/s41379-019-0415-5.

  Ivonne A. Montes-Mojarro performed the experiments and the analysis of the data, helped in writing the manuscript and prepared all figures and tables.

Seminars in diagnostic pathology (IF: 3.46)

- **Montes-Mojarro IA**, Kim WY, Fend F, Quintanilla-Martinez L. Epstein - Barr virus posi-tive T and NK-cell lymphoproliferations: Morphological features and differential diagno-sis. Semin Diagn Pathol 2020 Jan; 37(1): 32-46.

  Ivonne A. Montes-Mojarro wrote the manuscript, made the figures and tables.

Frontiers in Pediatrics (IF: 3.42)

- Kim, W.Y.; **Montes-Mojarro, I.A.;** Fend, F.; Quintanilla-Martinez, L. Epstein-Barr Virus-Associated T and NK-Cell Lymphoproliferative Diseases. *Front Pediatr* **2019**, *7*, 71, doi:10.3389/fped.2019.00071.

  Ivonne A. Montes-Mojarro helped in the manuscript preparation and made the figures.

BMC Medical Genetics (IF:2.1)

- Loffler MW, Steinhilber J, Hilke FJ, Haen SP, Bosmuller H, **Montes-Mojarro IA,** Bonzheim I, Stabler A, Faust U, Grasshoff U, Konigsrainer I, Rammensee HG, Kanz L,

Konigsrainer A, Beckert S, Riess O, Schroeder C First case report of malignant peritoneal mesothelioma and oral verrucous carcinoma in a patient with a germline PTEN mutation: a combination of extremely rare diseases with probable further implications. *BMC Med Genet*. Aug 15 2018;19(1):144.doi:10.1186/s12881-018-0651-4

Ivonne A. Montes-Mojarro helped in the revision of the histology, the protein status of PTEN by immunohistochemistry, prepared the corresponding figure and reviewed the manuscript.

Blood (IF:23.62)

- Schmidt, J.; Ramis-Zaldivar, J.E.; Nadeu, F.; Gonzalez-Farre, B.; Navarro, A.; Egan, C.; **Montes-Mojarro, I.A.**; Marafioti, T.; Cabecadas, J.; van der Walt, J., et al. Mutations of MAP2K1 are frequent in pediatric-type follicular lymphoma and result in ERK pathway activation. *Blood* **2017**, *130*, 323-327, doi:10.1182/blood-2017-03-776278.

  Ivonne A. Montes-Mojarro helped in revising the histology and immunohistochemistry and reviewed the manuscript.

10. Acknowledgments.

There are a number of people without whom this thesis simply could not have been written and to whom I owe a huge vote of gratitude.

To my mentors Prof. Leticia Quintanilla and Prof. Falko Fend, who are a great inspiration to me. Thank you for your time, support, patience, and hard work. This thesis was only possible through your efforts and commitment. Specially thanks to Prof. Quintanilla, who turned that struggle and effort into a precisely published work.

To my colleagues, friends, and supervisors. I would especially like to express my gratitude to Irina Bonzheim and Esther Kohler for their hard work, for sharing with me the joy and frustration of each result. To Franziska Otto, Achim Rau and Irene Gonzalez, for their unconditional professional advice.

I would especially like to thank Dr. Yamel Cardona, my colleague and friend from Tübingen Immunology and his PhD supervisor Prof. Alexander Weber, who provided me with expert advice and technical support in the development of new transfection methods.

My PhD committee, Prof. Alexander Weber, and Prof. Dr. Julia Skokowa, for their advice and criticism to improve this work.

My colleagues at the University of Vienna, Prof. Olaf Merkel, and Huang-Chang Jack Liang, as part of the ALK-related malignancies network (ALKATRAS), who helped to set up the Crispr-Cas9 experiments.

To my lovely friends, Antonio Vogelsberg, Mathis Overkamp, Yamel Cardona and Lina Serna-Higuita, for their trust and cheering, which made days sunnier and funnier. To my mother and brother, who encouraged and inspired me throughout my life, for supporting all my dreams to pursue my career and happiness, regardless of the distance placed between us.

And finally, for my husband who gave me his unconditional support in the bright and grey days. For his endurance and guidance in overcoming every challenge that I have come across. For being understanding of my weekends studying or doing lab work. For creating a greater version of myself. This thesis is for both of us.

———

This work was supported by funding of the European Union's Horizon 2020 research and innovative Programme under the Marie Sklodowska-Curie grant agreement No 675712

11. Supplementary tables.

Supplemental table 1. MiR-181a potential target genes

	gene	Base Mean	log2 FC	lfcSE	stat	pvalue	padj	Pred	CEBPβ
1	*SLC2A3*	29151.2	0.75	0.047	16.13	1.67E-58	1.07E-	4	
2	*PHLDA1*	574.2	1.13	0.100	11.35	7.54E-30	1.38E-	4	X
3	*CHST2*	4553.4	0.73	0.065	11.31	1.13E-29	1.82E-	1	
4	*COL16A1*	10574.7	0.69	0.064	10.69	1.08E-26	1.26E-	5	
5	*CCR1*	374.5	1.17	0.113	10.29	7.69E-25	7.60E-	2	
6	*EHF*	228.5	1.32	0.130	10.12	4.65E-24	4.27E-	4	
7	*AIM1*	639.9	0.88	0.088	9.99	1.70E-23	1.45E-	2	X
8	*KIAA1217*	918.5	0.68	0.076	9.00	2.30E-19	1.47E-	2	X
9	*HMGCS1*	14422.1	0.55	0.062	8.89	6.12E-19	3.57E-	2	
10	*COL5A1*	505.0	0.99	0.115	8.62	6.68E-18	3.57E-	3	
11	*PAM*	5283.1	0.49	0.057	8.61	7.61E-18	3.91E-	4	
12	*SCD*	26892.0	0.41	0.048	8.44	3.24E-17	1.44E-	4	X
13	*HSPA1B*	1115.2	0.78	0.093	8.39	4.72E-17	1.96E-	2	
14	*NR6A1*	779.1	0.69	0.082	8.36	6.04E-17	2.42E-	5	
15	*LRRC15*	132.8	1.17	0.142	8.21	2.28E-16	7.92E-	1	
16	*SIPA1L2*	4257.9	0.48	0.059	8.14	3.87E-16	1.21E-	3	
17	*ATP2B4*	4895.8	0.53	0.066	8.05	8.10E-16	2.42E-	2	
18	*HS3ST3A*	1088.8	0.62	0.079	7.83	5.06E-15	1.33E-	3	
19	*CA12*	1785.5	0.58	0.074	7.78	7.39E-15	1.90E-	1	
20	*DUSP6*	2960.3	0.49	0.064	7.74	9.64E-15	2.43E-	2	X
21	*CYP19A1*	230.5	1.07	0.140	7.64	2.10E-14	5.08E-	3	
22	*AGT*	393.2	0.91	0.119	7.58	3.42E-14	7.84E-	3	X
23	*CUBN*	146.1	1.13	0.150	7.53	5.11E-14	1.11E-	3	
24	*ANTXR2*	511.8	0.69	0.093	7.45	9.12E-14	1.92E-	3	X
25	*ETS1*	3497.5	0.46	0.062	7.43	1.06E-13	2.16E-	3	
26	*KIF3B*	3636.4	0.45	0.062	7.36	1.84E-13	3.70E-	3	
27	*MINK1*	3462.8	0.48	0.066	7.32	2.45E-13	4.63E-	4	
28	*TREM1*	1308.7	1.08	0.152	7.12	1.07E-12	1.81E-	1	
29	*IDH1*	2457.1	0.43	0.061	7.11	1.16E-12	1.94E-	3	
30	*PPAP2B*	933.1	0.62	0.088	7.02	2.16E-12	3.47E-	2	X
31	*ZKSCAN1*	13562.7	0.41	0.059	6.98	2.94E-12	4.55E-	3	X
32	*ARHGEF3*	815.2	0.53	0.078	6.82	9.08E-12	1.30E-	3	
33	*IQGAP2*	254.1	0.92	0.137	6.69	2.19E-11	2.93E-	2	X
34	*ITGA3*	17600.8	0.43	0.065	6.66	2.71E-11	3.60E-	4	X

35	*PTPRC*	373.4	0.75	0.114	6.64	3.22E-11	4.14E-	3	X
36	*LIN28B*	1547.2	0.51	0.078	6.58	4.82E-11	5.84E-	5	
37	*SERTAD2*	2209.1	0.44	0.067	6.57	5.00E-11	5.95E-	3	
38	*GALNT3*	3087.3	0.46	0.070	6.55	5.89E-11	6.94E-	3	
39	*MGLL*	565.0	0.63	0.097	6.49	8.45E-11	9.37E-	1	
40	*VCAN*	16866.1	0.45	0.071	6.32	2.66E-10	2.76E-	3	X
41	*VDR*	1322.9	0.41	0.067	6.10	1.06E-09	9.63E-	3	
42	*FAM46C*	972.4	0.49	0.082	5.96	2.48E-09	2.11E-	3	
43	*E2F5*	1191.9	0.45	0.075	5.95	2.62E-09	2.21E-	5	
44	*RBPMS*	111.2	0.98	0.167	5.89	3.98E-09	3.24E-	1	X
45	*SEMA3A*	548.1	0.69	0.118	5.84	5.27E-09	4.10E-	1	
46	*SPP1*	4131.4	0.81	0.140	5.77	7.73E-09	5.85E-	4	X
47	*DOCK10*	163.2	0.85	0.148	5.73	1.01E-08	7.49E-	4	X
48	*TRAF1*	382.0	0.58	0.102	5.67	1.45E-08	1.03E-	3	
49	*GPR132*	414.7	0.52	0.095	5.52	3.46E-08	2.19E-	1	
50	*MYOM1*	810.0	0.43	0.079	5.48	4.32E-08	2.71E-	1	
51	*FOSB*	179.8	0.70	0.138	5.11	3.15E-07	1.61E-	1	
52	*CTLA4*	113.5	0.83	0.163	5.09	3.57E-07	1.81E-	2	X
53	*KCTD12*	692.1	0.44	0.089	4.99	6.10E-07	2.86E-	3	
54	*CBX7*	430.5	0.55	0.111	4.93	8.11E-07	3.64E-	5	
55	*SNTB1*	429.5	0.49	0.102	4.86	1.17E-06	5.05E-	3	
56	*HOXA1*	125.6	0.69	0.148	4.68	2.94E-06	0.0001	5	
57	*BAIAP2*	139.0	0.73	0.159	4.59	4.46E-06	0.0001	2	
58	*VGLL3*	1065.2	0.42	0.095	4.43	9.33E-06	0.0003	3	
59	*PRKCE*	369.9	0.48	0.111	4.29	1.81E-05	0.0005	5	
60	*PLCL2*	488.4	0.40	0.099	4.03	5.66E-05	0.0013	3	
61	*PIK3AP1*	5186.8	0.52	0.129	4.01	5.99E-05	0.0014	2	X
62	*BTBD11*	244.1	0.46	0.120	3.84	0.000121	0.0025	3	
63	*KLHL3*	204.5	0.50	0.134	3.77	0.000166	0.0032	2	
64	*HAVCR2*	155.2	0.52	0.144	3.59	0.000325	0.0056	2	X
65	*SFXN3*	253.3	0.42	0.127	3.28	0.001048	0.0142	2	
66	*PRICKLE2*	142.4	0.50	0.152	3.27	0.001067	0.0143	3	
67	*SLCO3A1*	245.1	0.40	0.123	3.27	0.001067	0.0143	2	
68	*ATP8B4*	189.8	0.40	0.130	3.12	0.001811	0.0216	1	

Abb.: gene: gene identifier; base mean: mean of normalized counts; log2FC: log 2 Fold Change difference of expression between control and SUDHL-1 with miR-26 overexpression, value reported on logarithmic scale to base 2; lfcSE: standard error estimate for the log2change assessment; stat: value of the statistic test for the gene or transcript, p-value: p-value for multiple testing for the gene; p adj: P-value adjusted for multiple testing adjusted by the FDR; Pred: number of miRNAs algorithms predicting this target gene.

Supplemental table 2. MiR-26a candidate target genes

	Gene	base-Mean	log2FC	lfcSE	stat	pvalue	padj	Pred
1	*CHAC1*	1126.89	1.48	0.10	14.92	2.48E-50	1.65E-46	4
2	*CD93*	12269.52	0.77	0.05	14.06	6.69E-45	2.97E-41	4
3	*LINGO1*	6194.26	0.77	0.07	11.88	1.57E-32	2.62E-29	4
4	*GBP2*	5078.04	0.76	0.06	11.70	1.30E-31	1.73E-28	1
5	*ITGAX*	3527.79	0.89	0.08	11.44	2.58E-30	3.12E-27	1
6	*ADAMTSL4*	6036.44	0.78	0.07	11.29	1.52E-29	1.56E-26	1
7	*COL4A2*	2950.47	0.79	0.07	10.98	4.79E-28	4.26E-25	3
8	*ST18*	1800.15	0.99	0.09	10.89	1.26E-27	1.05E-24	3
9	*CLU*	16379.95	0.55	0.06	9.71	2.84E-22	1.35E-19	1
10	*CACNA2D4*	6756.93	0.52	0.06	9.22	3.01E-20	1.14E-17	3
11	*CTDSP2*	6387.88	0.45	0.05	8.88	6.64E-19	2.21E-16	4
12	*MAPK13*	1023.16	0.75	0.08	8.88	6.89E-19	2.21E-16	1
13	*RPS6KL1*	1825.43	0.67	0.08	8.79	1.56E-18	4.55E-16	1
14	*TRIM38*	6607.57	0.54	0.06	8.68	4.06E-18	1.13E-15	1
15	*PTPRC*	373.41	0.96	0.12	8.22	1.96E-16	4.28E-14	1
16	*ADAM19*	57836.78	0.41	0.05	8.11	4.94E-16	1.01E-13	4
17	*VEGFA*	2414.52	0.54	0.07	7.96	1.69E-15	3.22E-13	1
18	*ITGA5*	1586.15	0.57	0.07	7.86	3.92E-15	7.16E-13	3
19	*OAF*	1441.98	0.58	0.07	7.85	4.16E-15	7.50E-13	5
20	*TAP1*	5188.45	0.42	0.05	7.82	5.49E-15	9.77E-13	3
21	*BZRAP1*	1566.07	0.68	0.09	7.74	9.99E-15	1.67E-12	1
22	*ITGB2*	1337.53	0.62	0.08	7.68	1.58E-14	2.47E-12	1
23	*NIPSNAP1*	5277.29	0.46	0.06	7.40	1.37E-13	1.91E-11	3
24	*SPON2*	680.30	0.71	0.10	7.39	1.45E-13	1.97E-11	1
25	*WIPI1*	623.84	0.73	0.10	7.17	7.57E-13	9.35E-11	1
26	*ARHGEF6*	9518.48	0.46	0.07	7.10	1.24E-12	1.50E-10	3
27	*H6PD*	3130.87	0.47	0.07	7.00	2.60E-12	2.80E-10	1
28	*COL5A1*	504.95	0.81	0.12	6.99	2.84E-12	3.03E-10	4
29	*MEI1*	598.47	0.68	0.10	6.95	3.53E-12	3.73E-10	3
30	*PPM1M*	810.42	0.58	0.08	6.84	7.80E-12	7.65E-10	2
31	*HIP1*	2398.53	0.46	0.07	6.81	9.57E-12	9.18E-10	4
32	*NPEPL1*	682.44	0.69	0.10	6.78	1.18E-11	1.11E-09	2
33	*NRP2*	2652.48	0.42	0.06	6.64	3.17E-11	2.71E-09	3
34	*TMEM42*	656.92	0.57	0.09	6.53	6.75E-11	5.29E-09	3
35	*TAZ*	1711.14	0.44	0.07	6.48	9.35E-11	7.04E-09	3

36	*STARD13*	2296.35	0.43	0.07	6.43	1.30E-10	9.52E-09	1
37	*ADM2*	1486.52	0.55	0.09	6.35	2.09E-10	1.44E-08	3
38	*DDIT4*	2345.87	0.56	0.09	6.35	2.21E-10	1.52E-08	2
39	*CYP19A1*	230.53	0.88	0.14	6.24	4.25E-10	2.72E-08	2
40	*MMP14*	216.44	0.80	0.13	6.22	5.09E-10	3.19E-08	4
41	*HOXB9*	737.67	0.64	0.11	6.05	1.42E-09	7.74E-08	1
42	*ZC3H6*	225.10	0.85	0.14	6.05	1.44E-09	7.78E-08	3
43	*RECQL5*	1658.73	0.43	0.07	6.03	1.60E-09	8.58E-08	1
44	*GREB1*	997.54	0.45	0.08	5.95	2.63E-09	1.37E-07	3
45	*IL11RA*	380.19	0.73	0.12	5.94	2.79E-09	1.43E-07	1
46	*PNPLA6*	5839.62	0.43	0.07	5.91	3.43E-09	1.72E-07	1
47	*GALNT3*	3087.29	0.41	0.07	5.88	4.10E-09	2.02E-07	3
48	*SNTB1*	429.47	0.61	0.10	5.82	5.79E-09	2.67E-07	2
49	*SEMA3A*	548.07	0.69	0.12	5.82	5.83E-09	2.68E-07	3
50	*PSD2*	197.99	1.18	0.20	5.78	7.45E-09	3.28E-07	1
51	*GPSM3*	349.70	0.62	0.11	5.71	1.15E-08	4.78E-07	1
52	*ULK1*	1715.70	0.44	0.08	5.68	1.34E-08	5.42E-07	5
53	*FCRLB*	434.73	0.57	0.10	5.65	1.56E-08	6.21E-07	1
54	*GPR155*	985.65	0.46	0.08	5.63	1.76E-08	6.83E-07	3
55	*COL19A1*	134.69	0.88	0.16	5.63	1.81E-08	7.02E-07	5
56	*SEMA6C*	396.42	0.62	0.11	5.59	2.30E-08	8.51E-07	3
57	*BCL9L*	6418.67	0.43	0.08	5.58	2.38E-08	8.75E-07	4
58	*DMBX1*	5214.70	0.43	0.08	5.57	2.53E-08	9.22E-07	1
59	*CCNB1IP1*	2066.86	0.43	0.08	5.50	3.82E-08	1.29E-06	1
60	*PNRC1*	1280.69	0.43	0.08	5.48	4.30E-08	1.40E-06	5
61	*PLEKHG5*	661.58	0.60	0.11	5.46	4.72E-08	1.51E-06	2
62	*PMAIP1*	928.77	0.45	0.08	5.43	5.63E-08	1.74E-06	4
63	*MYOM1*	809.99	0.42	0.08	5.23	1.67E-07	4.53E-06	3
64	*SUV420H2*	865.98	0.47	0.09	5.21	1.93E-07	5.15E-06	4
65	*OBFC1*	937.66	0.46	0.09	5.17	2.39E-07	6.11E-06	2
66	*SLC12A1*	210.66	0.75	0.15	5.04	4.55E-07	1.08E-05	3
67	*CAMK2D*	1406.42	0.42	0.09	4.92	8.73E-07	1.86E-05	1
68	*ZIC4*	438.35	0.49	0.10	4.89	1.00E-06	2.07E-05	2
69	*GPC2*	151.74	0.68	0.14	4.80	1.59E-06	3.03E-05	1
70	*AMACR*	119.97	0.76	0.16	4.73	2.28E-06	4.14E-05	2
71	*YPEL1*	239.38	0.65	0.14	4.64	3.53E-06	5.95E-05	5
72	*OLAH*	109.46	0.75	0.16	4.61	4.11E-06	6.77E-05	1
73	*SLC1A4*	703.11	0.43	0.09	4.60	4.30E-06	7.04E-05	3

74	*FGD1*	455.39	0.44	0.10	4.57	4.97E-06	7.86E-05	5
75	*APOBEC3G*	441.02	0.43	0.10	4.45	8.70E-06	0.000127296	1
76	*LAMB3*	1106.46	0.40	0.09	4.42	9.75E-06	0.000140319	1
77	*CALCOCO1*	757.69	0.45	0.10	4.42	1.01E-05	0.000143034	1
78	*AMT*	301.50	0.58	0.13	4.39	1.14E-05	0.000157923	1
79	*RYR2*	228.94	0.64	0.16	4.11	4.01E-05	0.000453537	1
80	*OPRL1*	204.15	0.51	0.13	3.86	0.000114366	0.001086074	2
81	*DNAJB5*	238.16	0.45	0.12	3.83	0.000126088	0.001170705	2
82	*SLC7A11*	383.68	0.53	0.14	3.73	0.000194589	0.001681437	3
83	*PSD3*	222.19	0.48	0.13	3.70	0.00021759	0.00184903	5
84	*DMD*	184.80	0.46	0.13	3.51	0.000452665	0.003392568	3
85	*PTPRH*	317.38	0.42	0.12	3.48	0.000495035	0.003662765	3
86	*CTLA4*	113.47	0.57	0.16	3.45	0.000562013	0.004054829	1
87	*RHBDF1*	225.79	0.45	0.13	3.43	0.000611488	0.00435755	1
88	*C1RL*	247.99	0.42	0.12	3.39	0.000702916	0.004866031	3
89	*PAQR8*	324.77	0.40	0.12	3.31	0.000922841	0.006070172	3
90	*PBX1*	134.34	0.49	0.15	3.31	0.000939129	0.00615908	2
91	*DLG4*	129.12	0.51	0.15	3.30	0.000971598	0.006320779	2
92	*KLHL3*	204.54	0.42	0.14	3.11	0.001885575	0.010518985	2
93	*FSTL1*	102.22	0.51	0.17	2.96	0.003120961	0.015637646	1
94	*ZMAT1*	103.28	0.48	0.16	2.93	0.003347798	0.016458773	3
95	*HIST2H2BE*	103.36	0.45	0.16	2.85	0.004434089	0.020579286	1
96	*HSD17B6*	101.06	0.47	0.17	2.80	0.005052745	0.022736499	3

Abb.: gene: gene identifier; base mean: mean of normalized counts; log2FC: log 2 Fold Change difference of expression between control and SUDHL-1 with miR-26 overexpression, value reported on logarithmic scale to base 2; IfcSE: standard error estimate for the log2change assessment; stat: value of the statistic test for the gene or transcript, p-value: p-value for multiple testing for the gene; p adj: P-value adjusted for multiple testing adjusted by the FDR; Pred: number of miRNAs algorithms predicting this target gene.